



UNIVERSITEIT•STELLENBOSCH•UNIVERSITY
jou kennisvennoot • your knowledge partner

The Design and Manufacture of a Device to Measure Drivetrain Losses for a Bicycle

Mr. T. Payne
Student no. 20198906

November 2020



Department of Mechanical and Mechatronics Engineering
University of Stellenbosch
Private Bag X1, Matieland 7602 , South Africa.



The Design and Manufacture of a Device to Measure Drivetrain Losses for a Bicycle

by

Troy Payne
20198906

Mechanical Final Year Project 478

Final Report

Supervisor: Prof G Venter

Department of Mechanical Engineering
Stellenbosch University
November 2020

Declaration

I have read and understand the Stellenbosch University Policy on Plagiarism and the definitions of plagiarism and self-plagiarism contained in the Policy [Plagiarism: The use of the ideas or material of others without acknowledgement, or the re-use of one's own previously evaluated or published material without acknowledgement or indication thereof (self-plagiarism or text-recycling)].

I also understand that direct translations are plagiarism, unless accompanied by an appropriate acknowledgement of the source. I also know that verbatim copy that has not been explicitly indicated as such, is plagiarism.

I know that plagiarism is a punishable offence and may be referred to the University's Central Disciplinary Committee (CDC) who has the authority to expel me for such an offence.

I know that plagiarism is harmful for the academic environment and that it has a negative impact on any profession.

Accordingly all quotations and contributions from any source whatsoever (including the internet) have been cited fully (acknowledged); further, all verbatim copies have been expressly indicated as such (e.g. through quotation marks) and the sources are cited fully.

I declare that, except where a source has been cited, the work contained in this assignment is my own work and that I have not previously (in its entirety or in part) submitted it for grading in this module/assignment or another module/assignment.

I declare that have not allowed, and will not allow, anyone to use my work (in paper, graphics, electronic, verbal or any other format) with the intention of passing it off as his/her own work.

I know that a mark of zero may be awarded to assignments with plagiarism and also that no opportunity be given to submit an improved assignment.

Signature: 

Name: Troy Payne

Student no: 20198906

Date: 05 November 2020

MECHANICAL FINAL YEAR PROJECT 478: SUMMARY

Student: T Payne

Title of Project
The Design and Manufacturing of a Device to Measure Drive Train Losses for a Bicycle.
Objectives
The project is comprised of three main parts, i.e, the design and manufacture of a test rig that would imitate a bicycle drive train, the design and implementation of a braking mechanism that would represent resistance felt by the cyclist, the implementation of a speed sensor to measure rotational shafts speed and finally the construction of a dynamic torque transducer capable of accurately measuring dynamic torque in order to determine drive train efficiency. The test rig also needs to be compatible with a variety of bicycle drive train components and must be able to shift gears.
What is current practice and what are its limitations?
Currently the technology to measure dynamic torque of a rotating shaft is costly and not available to everyone.
What is new in this project?
This project will aim to reduce the costs involved with measuring input and output power. The project will make use of off the shelf electronics as measuring equipment and open source data acquisition software using Arduino and the Python programming language.
If this project is successful, how will it make a difference?
If the accuracy of the proposed torque measuring device relates to that of industry standard torque transducers it can be determined that it is possible to build dynamic torque transducers using “cost effective” electronics. Cyclists will also be able to make educated decisions when buying bicycle drive train components or deciding on which chain lubricant to use.
What is the end result of this project?
Reduce the cost involved in accurately measuring bicycling drive train efficiencies.
What contributions have/will other students made/make?
This project was formerly done as a final year Skripsie project and this current project aims to improve on lessons learned previously. However the current project is a completely new project, as no hardware, equipment or methods from the previous project are used in this project.
What are the expected advantages in the projects continuation?
If a thorough dataset containing efficiencies of different bicycle drive train component combinations can be created, cyclists can make informed decisions when purchasing equipment.
What arrangements are being made for continuation of this project?
All prototypes of the designed system is returned to the faculty. Developed programs used in this project is documented as well as the data obtained during testing. Should this project be continued or a similar project endeavoured all components of this project will be well documented for continuation or used as reference.

ECSA Exit Level Outcomes

ELO 1: Problem solving

Chapter 1 stipulates the formulation of objectives to solve a given problem. In Chapter 3 engineering requirements are formulated and suitable concepts discussed. Chapter 3 details the final design proposed to achieve the objectives stipulated in Chapter 1 and adhere to the engineering requirements. In Chapter 6 the results of the proposed solution are discussed and conclusions are drawn.

ELO 2: Application of scientific and engineering knowledge

The application of scientific and engineering knowledge can be found in the technical design of system components in Appendix A, B, C and D. The principles of the various technologies used in this project i.e. the measuring equipment and the implementation thereof is discussed in Chapters 3 and 4.

ELO 3: Engineering design

Chapter 3 details the technical design process. Engineering requirements are formulated and various concepts capable of meeting project objectives are generated and discussed. The selection of each chosen concept for the different components are motivated and a detailed final design is included. The detailed design of components can be found in Appendix A, B, C and D. A techno-economic analysis is performed in Appendix G.

ELO 5: Engineering methods, skills and tool, including Information Technology

The effective use of engineering methods, skill and tools including those based on information technology can be found in Chapter 3 and the implementation thereof in Chapters 4, 5 and 6. Micro-controllers are primarily used to measure dependant variables and interfaced with the Python environment for data logging and post processing.

ELO 6: Professional and technical communication

The presentation of this final report accompanied by an oral presentation (verbal communication) and poster (visual communication) demonstrates competency to communicate effectively with engineering audiences and the community at large.

ELO 8: Individual, team and multidisciplinary working

Completion of this project without delay, shows competency in working as an individual during the research and design phase of this project, but also the ability to work in a team and multidisciplinary environment during the development phase. Effective communication with lab technicians and the mechanical workshop was critical in producing the designed system in an acceptable time frame.

ELO 9: Independent learning ability

The implementation of various technologies, some of which only theoretical knowledge had been obtained before commencing this project, shows competency in the ability to learn independently as this involved extensive research (Chapter 2). Skills such as Arduino programming, development in the Python environment for data logging and skills used in the assembly of mechanical systems were all obtained as a result of independent learning (Chapter 3).

Contents

Declaration	i
Mechanical Final Year Project 478: Summary	ii
ECSA Exit Level Outcomes	iii
Contents	iv
List of Figures	vi
List of Tables	ix
1 Introduction	1
1.1 Background	1
1.2 Objectives	1
1.3 Motivation	2
2 Literature Review	3
2.1 Existing bicycle drivetrain test rigs and their implementation	3
2.2 Dynamic torque transducers	5
2.3 Braking mechanism	13
2.4 Concluding the literature review	16
3 Technical Design	17
3.1 Customer requirements	17
3.2 Engineering requirements	18
3.3 Concept generation	18
3.3.1 Test rig	18
3.3.2 Brake mechanism	18
3.3.3 Shaft speed measurement	19
3.3.4 Torque measurement	21
3.4 Concept selection	22
3.4.1 Test rig design	22
3.4.2 Brake mechanism	23
3.4.3 Shaft speed measurement	24
3.4.4 Torque measurement	24
3.5 Final design	25
3.5.1 Test rig overview	25
3.5.2 Braking mechanism	27
3.5.3 Shaft speed measurement	28
3.5.4 Torque measurement	29
3.5.5 Data acquisition	32
4 Initial Testing and Calibration	35
4.1 Shaft speed calibration	35
4.2 Transducer static calibration	35
4.3 Initial testing and troubleshooting	36
4.3.1 Torque measurement errors	36

4.3.2	Shaft speed measurement errors	38
4.4	Transducer dynamic calibration	39
5	Eddy Current Brake Effectiveness	41
5.1	Brake calculations validation	42
6	Testing	43
6.1	Test procedure	43
6.2	Data processing	43
6.3	Test rig performance	44
6.4	Efficiency tests using different lubricants	46
6.5	Suggested further work	48
7	Conclusion	49
A	Motor Selection Calculations	51
B	Transducer Design	53
C	Eddy Current Brake Design	56
D	Shaft Design	63
D.1	Output shaft design	63
D.2	Summary of shaft design	66
E	Pugh Charts	67
F	Risk Analysis and Safety Procedure	68
G	Techno-Economic Analysis	71
G.1	Budget	71
G.2	Time management	72
G.3	Technical impact	74
G.4	Return on investment	74
G.5	Potential for commercialization	75
H	Instrumentation Used	75
H.1	Calibration	75
H.1.1	Data acquisition system	75
H.1.2	In-line torque transducer	76
H.2	Speed sensors	76
H.3	Designed torque transducer	76
H.3.1	Sparkfun HX711 analog-to-digital load cell amplifier	76
H.3.2	Arduino Nano	76
H.3.3	NRF24L01 transceiver module	76
H.4	Arduino Uno DAQ system	77
	List of References	78

List of Figures

2.1	Drivetrain test rig schematic, (Spicer <i>et al.</i> (2000))	4
2.2	Drivetrain test rig schematic, (Bolen and Archibald (2017))	4
2.3	Optical probe and zebra tape schematic, (Zappalá <i>et al.</i> , 2018)	6
2.4	Torque test rig setup used by Zappalá <i>et al.</i> (2018)	6
2.5	(a) Simplified schematic representation of the calibration setup; (b) detail of load cell, strain sensors and movable arm, (Silva <i>et al.</i> , 2017)	7
2.6	Radio frequency (RF) antenna used by Silva <i>et al.</i> (2017)	7
2.7	Details of Bragg gratings mounted on rotating shaft proposed by Kruger <i>et al.</i> (2004)	8
2.8	Rotating mount for GRIN lenses, (Kruger <i>et al.</i> , 2004)	8
2.9	Strain gauge orientation when used to measure shaft torque (Muftah <i>et al.</i> , 2013)	9
2.10	Commonly used body forms when measuring shaft strain using strain gauges, (Muftah <i>et al.</i> , 2013)	10
2.11	(a) V-shape strain gauge used by Muftah <i>et al.</i> (2013). (b) The V-shaped strain gauge mounted on shaft by Muftah <i>et al.</i> (2013).	10
2.12	Proposed model design by Mustafa <i>et al.</i> (2018)	11
2.13	FEA analysis performed by Mustafa <i>et al.</i> (2018)	11
2.14	Readout electronic circuit by Mustafa <i>et al.</i> (2018)	12
2.15	Experimental setup, Mustafa <i>et al.</i> (2018)	12
2.16	(a) Torque sensing strain gauge in full Wheatstone bridge configuration. (b) Four quarter bridge gauges in full Wheatstone bridge configuration. (Binsfeld Engineering [Online])	13
2.17	Double-sided permanent magnet linear eddy current brake, (Edwards <i>et al.</i> , 1999)	14
2.18	Schematic of Eddy currents, (Smith (2019))	14
2.19	Diagram of Eddy Current Brake system (Lee and Park, 1999)	15
2.20	Electro magnetic breaking system using Eddy currents, (Baharom <i>et al.</i> , 2011)	15
2.21	Permanent magnet eddy current brake topologies. (a) Halbach magnetization, (b) horizontal magnetization, (c) vertical magnetization, (Jang and Lee, 2003).	15
3.1	Schematic of a band brake dynamometer (Killedar, 2012)	19
3.2	Rotor disc with magnets on either side, (Rodrigues <i>et al.</i> , 2016)	19
3.3	(a) Infrared sensor module, (Micro Robotics [Online]). (b) Tachometer using IR sensor, (Viral Science, The Home of Creativity [Online])	20
3.4	LED and photodiode module, (Botshop [Online])	20
3.5	Perforated disc in conjunction with optical encoder, (RS Components [Online])	21
3.6	T22 HBM in-line Torque Transducer, (HBM [Online])	21
3.7	Torque sensing strain gauge configuration, (van der Merwe, 2020)	22
3.8	Measuring motor reaction force, (Killedar, 2012)	22
3.9	(a) Spinning bike braking mechanism, (Indoor Training Bikes [Online]). (b) and (c) Resistance trainer Eddy current brake mechanism.	23
3.10	(a) Maximum braking resistance magnet orientation and attracting magnetic fields. (b) Minimum braking resistance magnet orientation and repelling magnetic fields. (Wikipedia [Online])	23

3.11	Input Shaft.	25
3.12	Bicycle drive train.	26
3.13	Output Shaft.	26
3.14	Test Rig.	26
3.15	Two stage gear reduction at end of output shaft.	27
3.16	(a) Brake housing backplate with one magnet disc holder fastened indicating magnet slots and brake output shaft. (b) Full brake assembly with both magnet disc holders engaged.	28
3.17	Speed sensor electronic components schematic.	29
3.18	Perforated disc in conjunction with photo interrupter module to measure input shaft speed.	29
3.19	Strain gauges attached in full Wheatstone bridge configuration to transducer body.	30
3.20	(a) Typical weigh scale application block diagram, (Avia, 2017). (b) Data output, input and gain selection, timing and control, (Avia, 2017).	31
3.21	Transducer electronics component schematic.	32
3.22	(a) Fully assembled torque transducer mounted in-line with the input shaft. (b) Full strain gauge Wheatstone bridge wiring.	32
3.23	Schematic depicting the wire and pin connections of the Arduino DAQ system.	33
3.24	(a) Logic flow of Arduino DAQ system. (b) Python data logging logic flow.	34
4.1	Comparing measured shaft speed with actual shaft speed.	35
4.2	Static calibration jig.	36
4.3	(a) Oscillations present in output shaft torque measurement at zero breaking load applied. (b) Reduction in the amplitude of oscillations present in the measured torque values after inserting a shim.	37
4.4	(a) Random noise present in the input shaft speed measurements. (b) Reduction in amplitude and frequency of noise present in speed measurements.	38
4.5	Designed torque transducer in-line with the HBM T22 Torque transducer.	39
4.6	(a) Output torque transducer calibration 40 RPM input. (b) Output torque transducer calibration 80 RPM input.	40
4.7	(a) Input torque transducer calibration 40 RPM input. (b) Input torque transducer calibration 80 RPM input.	40
5.1	Magnet disc holders positions.	41
5.2	Torque induced by Eddy Current Brake in Position 1 (a) and Position 2 (b).	41
5.3	Torque induced by Eddy Current Brake in Position 3.	42
5.4	Calculated power induced at input shaft vs measured power induced at input shaft.	42
6.1	(a) Example of dataset pre-processing. (b) Example of dataset post-processing.	44
6.2	Candle-wax coated chain efficiency tests.	45
6.3	Average efficiency measured over time.	46
6.4	Average efficiency of drive with train error bar indicating the standard deviation between the five tests conducted per lubricant.	47
E.1	(a) Brake option definition. (b) Shaft speed measurement option definition. (c) Torque measurement option definition	67

E.2	(a) Brake mechanism Pugh chart. (b) Shaft speed measurement Pugh chart.	67
E.3	Torque measurement Pugh chart.	67
F.1	Test rig safety chains and guard covering all rotating components.	71

List of Tables

3.1	Engineering Requirements	18
3.2	Transducer dimensions	29
3.3	Electronic components for both torque transducers.	30
3.4	HX711 Input Channel and Gain Selection (Avia, 2017)	31
3.5	Electronic components for Arduino DAQ system.	33
4.1	Static calibration results	36
6.1	Comparison of difference in input and output torque measured with candle-wax coated chain.	44
6.2	Comparing output losses experienced by the candle-wax coated chain and efficiency derived from each test.	45
6.3	List of lubricants tested and efficiencies calculated with standard deviation between tests.	46
D.1	Input shaft.	66
D.2	Output shaft.	66
D.3	Brake shaft.	66
D.4	Gear reduction shaft.	66
F.1	Risk Assessment Matrix	69
F.2	Activity Based Risk Assessment	69
G.1	Proposed budget.	72
G.2	Actual budget.	72
G.3	Hours worked.	73
G.4	Proposed Gantt chart.	73
G.5	Actual Gantt chart.	74

Chapter 1

Introduction

1.1 Background

Bicycle and bicycle drivetrain technologies have been around for more than a century. In recent times it has become increasingly important to determine and minimise drivetrain losses, in order to maximise the output power generated by the cyclist. By minimising drivetrain losses, the cyclist may gain an advantage over their competitors. The quest to gain an advantage has become more important due to the professional nature of the sport, improved build technology and the increased investments incurred by the sports top athletes and teams. Understanding bicycle drivetrain efficiency and what affects it, is of huge interest to the cycling community.

Having the most efficient drivetrain is not only of interest to professional cyclists, but also the amateur and Sunday cruiser cycling enthusiasts, as nobody wants to feel that their efforts are in vain. A wide range of bicycle components and lubricants at varying costs are currently available on the market. If the optimal combination of components and lubricants can be determined, it could provide the cyclist with the information needed to assemble the most efficient drivetrain for their specific budget. If not limited by a budget, the most efficient drive train can be assembled.

The most challenging aspect of this project is the ability to accurately measure mechanical losses in a bicycle drive train. Bicycle drive trains are capable of operating at an efficiency as high as 98% this would mean a mere loss of only 4 W at an input cycling power of 200 W.

In order to determine the efficiency, the input and output power of the drive train is measured and compared. However, the power is not measured directly but rather calculated knowing what the rotational shaft speed and torque experienced by the rotating component is. Therefore the design will be focused around measuring rotational shaft speed and dynamic torque whilst implementing a braking mechanism capable of applying the necessary load to mimic the resistance experienced by a cyclist.

Thus the aim of this project is to design, manufacture and test a device that can accurately measure drivetrain losses for a bicycle.

1.2 Objectives

The objectives of the project are therefore:

- 1. Design and manufacture a test rig:**

Design and manufacture a two axle drivetrain driven at the front by an electric motor that would represent the pedal input of a cyclist. A brake must be implemented at the rear axle that would imitate the resistance the cyclist must overcome in order to power the bicycle forward. The rig must be able to accommodate various drive

train components and must have the ability to shift gears whilst operating. The rig must also be stiff/rigid to only account for drive train mechanical losses.

2. Measure input and output power:

To address the main objective of measuring input- and output power accurately, a device must be mounted on both the input and output shafts capable of measuring dynamic torque. A tachometer must be placed on both shafts to measure shaft rotational speed in order to convert torque measurements into power measurements. Thus the ability to measure dynamic torque is the first focus point of this project in order to obtain accurate data.

3. Apply variable load to simulate cycling resistance:

The second focus point of this project is the implementation of a mechanism to simulate the resistance experienced by a cyclist. This will be in the form of a braking mechanism applied to the rear end of the output shaft to induce a braking torque.

4. Obtain and analyse data:

The data obtained by these power measurements must then be compiled by a suitable software and an efficiency analysis is to be performed and results compared to data obtained from literature.

1.3 Motivation

Most bicycle efficiency parameters are governed by variables such as percentage increase/decrease in frame stiffness, the weight of the frame, wheel sets used as well as rolling resistance experienced by different tyre profiles and thicknesses. These factors do influence bicycle efficiencies. Available data on the influence that different drivetrain components have on drivetrain efficiency, is however limited. This project will thus aid in determining what influence different components and lubricants have on efficiency, as this is a direct performance measure.

This project would aid in the understanding of drivetrain losses and would allow cyclists, both professional and occasional, to assemble the most efficient bicycle drivetrain.

Chapter 2

Literature Review

The purpose of the literature review is to determine what the best method would be for accomplishing all the objectives set out in Chapter 1. The literature review is thus divided into three sections. Reviewing existing test rigs and their implementation, reviewing existing dynamic torque measuring equipment and techniques and a means of creating braking load on the system.

2.1 Existing bicycle drivetrain test rigs and their implementation

Spicer *et al.* (2000) conducted a similar study in the “Technical Journal of The IHPVA”. In the study they gave a thorough description of the experimental apparatus used and the experimental procedure followed.

To assess the drivetrain efficiency of bicycle components, a test rig was designed to effectively measure the mechanical losses involved from the front chainring to the rear transmission components. In order to determine the efficiency, the input and output power of the system was measured and the ratio was used to calculate drive train efficiency. In order to determine respective shaft power, the torque transmitted by the shaft along with shaft rotational speed was measured. The speed of the driven shaft was not measured directly, but rather calculated by multiplying the drive shaft speed with the selected gear ratio. The efficiency of the system was then derived using the following equation:

$$\text{Efficiency}(\%) = \frac{\tau_2 \omega_2}{\tau_1 \omega_1} \quad (2.1)$$

Where τ_1 and τ_2 represents the shaft torque experienced whilst ω_1 and ω_2 represent the rotational speed of the the respective shafts in rad/s.

The data required to calculate efficiency was gathered using a data acquisition system connected to a PC. Figure 2.1 depicts the test bench setup used by Spicer *et al.* (2000).

The shaft torque was measured by implementing a rotary torque transducer at both the input and output shafts, whilst the shaft speed was measured using a speed sensor. The input and output shafts were configured in such a manner that the drive components could be adjusted accurately to ensure the correct distance from the cassette to the front chain ring. The drive shaft was driven by an electric motor and the speed controlled using a variable speed drive (VSD). The drive shaft speed was not changed during operation but rather set at a desired rotation rate. To create a dynamic braking load an electromagnetic brake was connected to the output shaft.

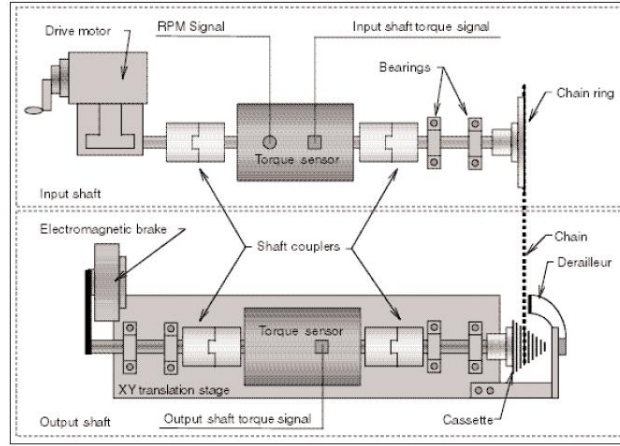


Figure 2.1: Drivetrain test rig schematic, (Spicer *et al.* (2000))

Spicer *et al.* (2000) conducted various tests at various loads, drive shaft rotational speeds, time intervals and configurations, ranging from 100 W to 75 W, 50 RPM to 70 RPM, 30 min to 2 hours.

It was apparent that from the tests that Spicer *et al.* (2000) conducted that the efficiency was highly dependant on the rear sprocket size. An increase in sprocket size correlated to an increase in drive train efficiency. It was also found that the efficiency decreased with an increase in rotational rate at constant power input. It was observed that efficiency increased with an increase power for constant rotational rate. Higher chain tension resulted in an increase in efficiency regardless of input power and rotational rate (Spicer *et al.*, 2000).

Further examples of test rigs utilised in literature are shown in figure 2.2:



Figure 2.2: Drivetrain test rig schematic, (Bolen and Archibald (2017))

A similar study was conducted by Bolen and Archibald (2017) in order to determine bicycle drive train efficiency. The basic principle of their test rig was similar to that of Spicer *et al.* (2000), with input shaft driven by a geared motor and a brake applied to the end of the output shaft to induce a load. They however relied on different methods of measuring dynamic torque and shaft speed. Input torque was measured by a load cell, shown in green (Figure 2.2), in conjunction with a motor lever arm with a wire that measures the motor reaction force. Output torque was measured using a band brake dynamometer with the output force calculated by determining the difference between readings from a load cell measuring the slack side of the friction belt and the load cell measuring the taut side. Shaft speed was measured by an inductive proximity sensor, shown in orange (figure 2.2).

2.2 Dynamic torque transducers

Research was conducted to understand the working principle of the various techniques used to measure dynamic torque. Dynamic torque is the torque experienced by a rotating component. According to Muftah *et al.* (2013), torque is a very important parameter used to determine the quality of the mechanism. Torque can be defined as a force that acts to rotate a body around its central axis (Muftah *et al.*, 2013). The central axis is the axis that runs through the length of the member (Muftah *et al.*, 2013). This definition is applicable to both dynamic and static torque measurements. This literature review will focus on dynamic torque.

Measure relative twist angle:

The first method considered was that of Zappalá *et al.* (2018) where they described non-intrusive, reliable and precise torque measurement as critical to dynamic performance. Zappalá *et al.* (2018) presented a contactless torque measuring system that does not require that the torque measuring device be inserted in-line with the rotating shaft but it rather consists of two shaft mounted zebra tapes and two optical sensors mounted on stationary rigid supports. Because this system does not require the expensive use of shaft mounted technology and is non-intrusive, it is cost-effective and applicable to a variety of advanced engineering applications.

The torque experienced by the shaft is measured by estimating the shaft twist angle through analysis of the pulse train time shift produced by the zebra tape. According to Zappalá *et al.* (2018) intrusive torque sensing technology is susceptible to noise and requires bearings, which involves maintenance. The major obstacle of direct measuring systems is the high costs and intrusive nature involved, which is impractical for short term use. Direct measuring systems cannot be implemented when the original system design does not allow for in-line implementation.

The methodological approach proposed by Zappalá *et al.* (2018) is based upon the phenomenon that when torque is applied to a shaft, the shaft itself twists with one end rotating with respect to the other end by an angle displacement referred to as theta (θ). Assuming that the shaft is of constant diameter and of a linear homogenous elastic material, the relationship between applied torque and relative angular displacement between shaft ends can be described Equation 2.2:

$$T = I\ddot{\theta} + C\dot{\theta} + K\theta \quad (2.2)$$

T being the torque experienced in Nm, θ , $\dot{\theta}$ and $\ddot{\theta}$ representing angular displacement (rad), angular velocity (rad/s) and angular acceleration (rad/s²), respectively. I , C and K represent the mass moment of inertia (m⁴), damping coefficient (Ns/m) and spring constant (N) of the rotating member.

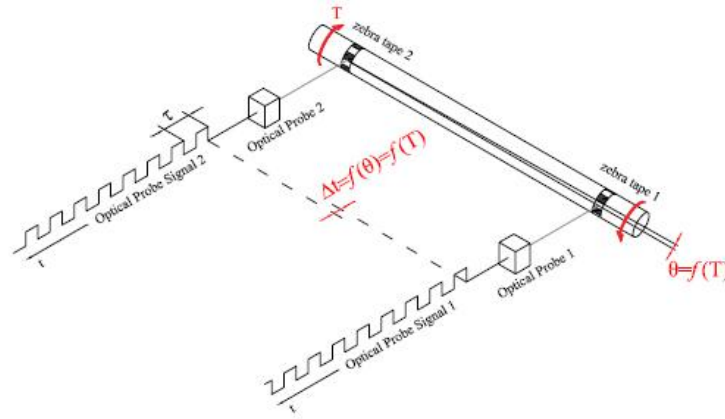


Figure 2.3: Optical probe and zebra tape schematic, (Zappalá *et al.*, 2018)



Figure 2.4: Torque test rig setup used by Zappalá *et al.* (2018)

Sound acoustic wave technology:

Another technique proposed by Silva *et al.* (2017) is the use of surface acoustic wave (SAW) technology, used to monitor strain that is felt by a mechanical component. An SAW device is composed of a piezoelectric slab with one interdigitated (IDT) contact and some reflectors (Silva *et al.*, 2017). The working principle of SAW sensors is that when an alternating magnetic field is applied to the IDT of a SAW resonator, a mechanical deformation of the piezoelectric substrate takes place. If the distance between the IDT fingers is such that the frequency of the electric signal, f_c , is related with the phase velocity V_p and the wavelength of the SAW λ by $f_c = \frac{V_p}{\lambda}$, a resonance condition happens and a SAW wave propagates across the surface of the piezoelectric material (Silva *et al.*, 2017).

Thus if external factors such as temperature and deformation influence the propagation characteristics of the piezoelectric material, the phase velocity of the SAW waves changes and the frequency f_c changes accordingly. It is thus possible to get an indirect measurement of the parameter being monitored by probing the resonant frequency of the SAW sensor. A characteristic that makes SAW sensors ideal for measurement of strain on rotating parts is that the IDT can directly be connected to a radio frequency (RF) antenna and interrogation of the device can be made remotely, without the use of wires. These devices also do not require external power or batteries as they are passive devices (Silva *et al.*, 2017).

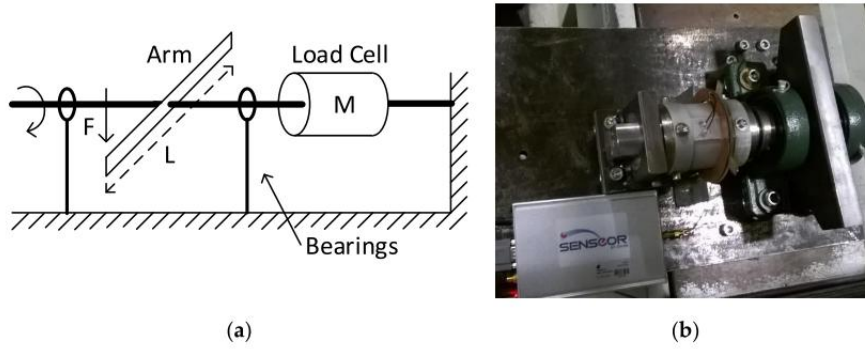


Figure 2.5: (a) Simplified schematic representation of the calibration setup; (b) detail of load cell, strain sensors and movable arm, (Silva *et al.*, 2017)



Figure 2.6: Radio frequency (RF) antenna used by Silva *et al.* (2017)

Fibre Bragg gratings:

Another non-contact way of measuring rotating shaft torque was presented by Kruger *et al.* (2004). Even though the use of fibre Bragg gratings for sensing strain in mechanical components was well known, the use of fibre Bragg gratings for measuring torque was fairly new, at the time of publication. Using fibre Bragg gratings to measure rotating shaft torque involves the use of graded index lenses for transmitting optical information between the light source and the gratings, and back to a spectrum analyser (Kruger *et al.*, 2004). Wang *et al.* (2001) proposed the idea of using an etched long-period grating as a twist sensitive torsion transducer. The problem with etched long period gratings and the use of a single fibre Bragg grating sensor is the sensitivity to temperature changes (Kruger *et al.*, 2004). That is why Kruger *et al.* (2004) presented a novel non-contact torque measuring device that is based on the use of two fibre Bragg gratings and graded index (GRIN) lenses. These are lenses with a constant thickness while the refractive index varies in the radial direction, therefore not relying on curved surfaces, as alternative to the aforementioned techniques. Using two fibre Bragg gratings has the advantage of being relatively insensitive to temperature changes and has twice the sensitivity of using a single fibre Bragg grating and will not be prone to electromagnetic interference (EMI) (Kruger *et al.*, 2004).

Figure 2.7 depicts the Bragg grating orientation of the proposed torque transducer by Kruger *et al.* (2004). Two Bragg gratings of different centre wavelengths are used to sense principle tensile and compressive strains. The gratings should be oriented at an angle of 45° with the neutral axis and at 90° with respect to one another. At this orientation the

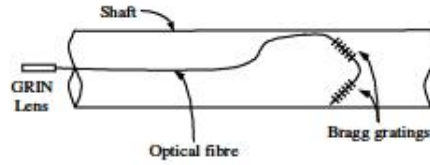


Figure 2.7: Details of Bragg gratings mounted on rotating shaft proposed by Kruger *et al.* (2004)

Bragg grating will only measure pure tensile and pure compressive strain. They will thus experience principle strains in the opposite direction, causing their resonant wavelengths to move in the opposite direction whereas a change in temperature will shift their resonant wavelength in the same direction (Kruger *et al.*, 2004).

To separate the paths of the incident optical excitation from that of the returning signal from the measurement transducer, a special device is used through which the optical power is guided. The coupling between the rotating and stationary components of the system occurs through a set of suitably aligned lenses. The wavelengths of the Bragg gratings, λ_1 and λ_2 are different and chosen specifically to not overlap under maximum strain in the shaft (Kruger *et al.* (2004)). These gratings therefore reflect two distinct wavelengths, for which the values are functions of strain and temperature.

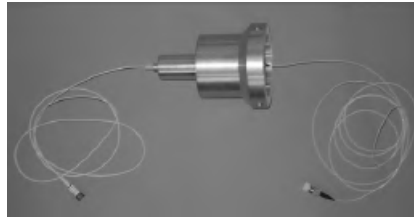


Figure 2.8: Rotating mount for GRIN lenses, (Kruger *et al.*, 2004)

Kruger *et al.* (2004) proved the feasibility of torsion measurement when using dual fibre Bragg gratings together with GRIN lenses, offering a great advantage over the use of conventional slip rings.

Strain gauge based torque transducer:

Muftah *et al.* (2013) proposed an improved strain gauge-based dynamic torque measurement method. The researchers investigated the use of a new strain gauge shape to determine the dynamic torque.

The use of strain gauge-based strain measurement has been widely used in industrial applications due its relatively low cost and high sensitivity (Mustafa *et al.*, 2018). Metallic strain gauge torque transducers are used to measure the strain experienced by the shaft due to a external torsional load. A bridge circuit is generally used to detect the small changes in resistance of the gauges caused by a change in diameter of the metallic gauge wires due to the applied load. A voltage measuring device can then be used to measure the voltage unbalance in the bridge circuit and indicates a change in resistance (Figliola, 2015). The bridge circuit is commonly referred to as a Wheatstone bridge circuit.

Figure 2.9 depicts the orientation of the strain gauges when measuring shaft torque. The strain gauges are applied to the shaft in a Wheatstone bridge configuration. The first two strain gauges are oriented at an angle of 45° with the neutral axis and 90° respectively. The same applies to the remaining strain gauges but are attached to the opposite side of the shaft. Shear strain in the shaft occurs when a torque is applied to the shaft. Therefore, the tensile strain, which is measured by one pair of gauges, will increase the circuit resistance which in return will be decreased by the other pair of gauges due to the compression strain (Muftah *et al.*, 2013).

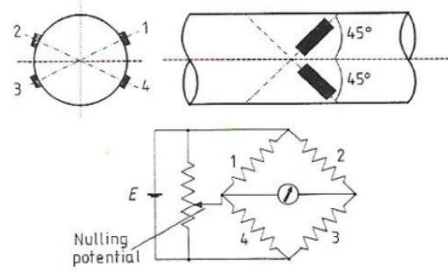


Figure 2.9: Strain gauge orientation when used to measure shaft torque (Muftah *et al.*, 2013)

This is considered to be a very popular method as there is no friction torque present, can be used in various temperature ranges and is insensitive to bending and axial stresses.

The one drawback of this method is developing an appropriate algorithm that can convert the resistance variations experienced by the gauge into a quantifiable amount (Muftah *et al.*, 2013).

To better understand the workings of metallic strain gauges a relationship between conductor length (L), electrical resistivity (ρ) and cross sectional area (A) have been established to determine the resistance (R) of that conductor.

$$R = \rho \frac{L}{A} \quad (2.3)$$

The sensitivity of the material can also be expressed by the Gauge Factor (GF).

$$GF = \frac{dR/R}{\epsilon} \quad (2.4)$$

Where dR/R represents the change in resistance and ϵ is the applied strain, Muftah *et al.* (2013).

In the research conducted by Muftah *et al.* (2013), a V-shaped strain gauge with measuring grid axis at $\pm 45^\circ$ to the axis of symmetry, was used.

During the design of the torque transducer described by Muftah *et al.* (2013), reference is made to 5 commonly used measuring body forms. The final design was based off a solid circular shaft with a reduced cross sectional area at the location of the strain gauge to create a stress concentration at that point.

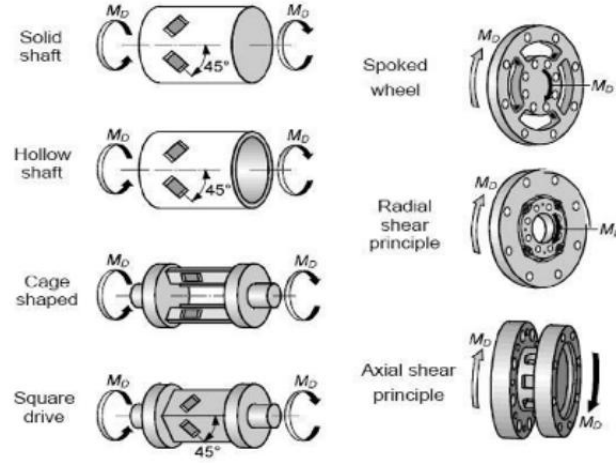


Figure 2.10: Commonly used body forms when measuring shaft strain using strain gauges, (Muftah *et al.*, 2013)

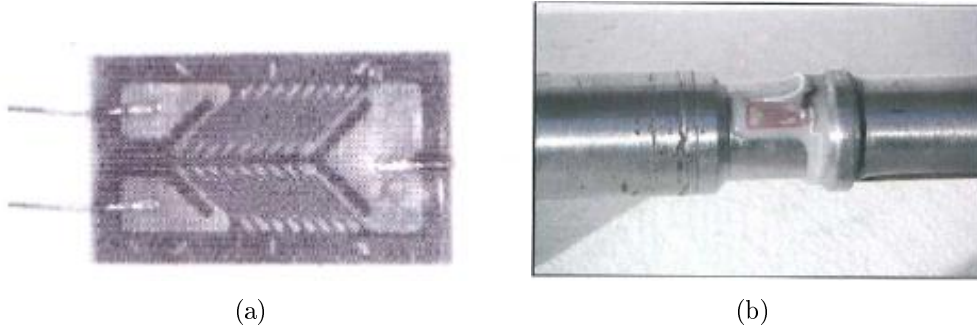


Figure 2.11: (a) V-shape strain gauge used by Muftah *et al.* (2013). (b) The V-shaped strain gauge mounted on shaft by Muftah *et al.* (2013).

The torque transducer proposed by Muftah *et al.* (2013) depicted in Figure 2.11(b) was calibrated using dead weights. Various tests were conducted and it was observed that the difference between the measured and calculated strain value was 1.5%.

Mustafa *et al.* (2018) proposed the development of a wireless clamp-on torque transducer. They based their research on the scientific contribution of Muftah *et al.* (2013), where they developed strain gauge-base torque transducers using new strain gauge shapes. Mustafa *et al.* (2018) wanted to improve on the work by Muftah *et al.* (2013) and decided to develop a wireless clamp-on torque transducer. The benefits of this system includes, wireless transmission, fast installation and there is no need to install additional parts in-line where the torque measurement is required (Mustafa *et al.*, 2018). This transducer can therefore be mounted directly onto the shaft.

The design of the clamp-on torque transducer is comprised of two collars with pre-calibrated strain gauge rods connecting the collars. The strain gauges are aligned precisely on the rods during assembly (Mustafa *et al.*, 2018). To extract the torque readings, a signal conditioning circuit is implemented to the control system with a STM32 micro-controller. Torque signals are then transmitted via a wireless RF (radio frequency) transmitter (NRF24L01 transceiver module), to achieve a desired non-contact torque measurement.

The proposed mechanical design of this torque measuring system is based on measuring the twist angle between two ends of the shaft when a torque is applied, given that the diameter of the shaft remains uniform. The angle of twist can mathematically be expressed by:

$$\phi = \frac{TL}{GI_p} \quad (2.5)$$

In the equation above ϕ , T , L , G and I_p represent angle of twist (rad), torque applied (Nm), and shaft length (m) while G indicates shear modulus of elasticity (N/m²) and I_p is the polar moment of inertia (m⁴). When the torque transducer is clamped onto the shaft and a torque is applied to the shaft, the deformation experienced by the shaft will be the same as that of the measuring rod. The deformation is thus measured by the strain gauge bridge attached to the measuring rod (Mustafa *et al.*, 2018).

The measured signals are amplified and converted by a bridge conditioning circuit and transmitted by the NRF24L01 transceiver module.

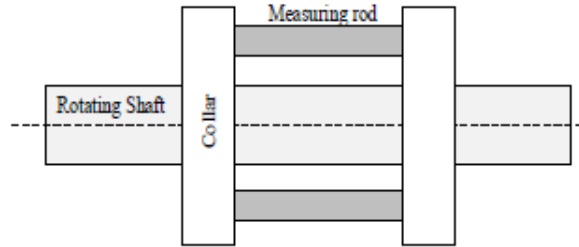


Figure 2.12: Proposed model design by Mustafa *et al.* (2018)

Mustafa *et al.* (2018) also performed a finite element analysis (FEA) on the proposed design to determine the maximum stress on the rods and the location thereof. In Figure 2.13 the maximum stress locations are indicated at the end of the rods and therefore strain gauges should be placed in those specific regions.

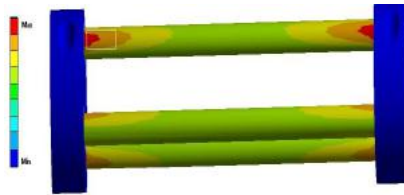


Figure 2.13: FEA analysis performed by Mustafa *et al.* (2018)

Amplification and filtering of the signal is also required due to the relatively weak voltages measured in the mV region, which are also susceptible to interference (Mustafa *et al.*, 2018). The proposed design performed the amplification in two stages, using two op-amp modules in series. These modules are capable of gains up to a thousand (Mustafa *et al.*, 2018). Filtering of the signal is also accomplished by the two amplification modules, AD620 and AD623.

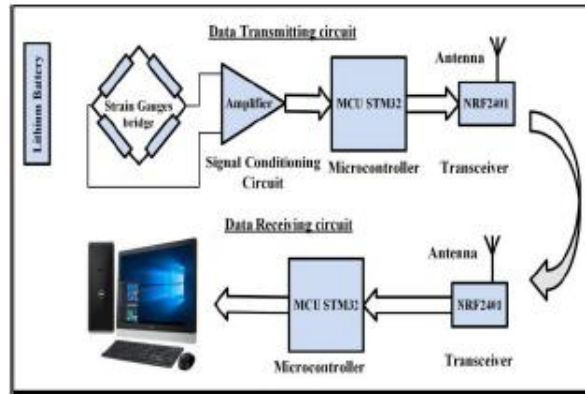


Figure 2.14: Readout electronic circuit by Mustafa *et al.* (2018)

Because the functionality of the microprocessor is essential to the developed system, it must have functions such as analog-to-digital conversion (ADC), serial port, multiple digital interfaces, etc, (Mustafa *et al.*, 2018). In order to meet the system requirements Mustafa *et al.* (2018) selected STM32 microcontroller with 12-bit ADC and numerous high frequency digital interfaces.

To achieve the most critical part in non-contact torque measurements is the transmission of accurate RF signals which needs high communication speed and high signal strength. To achieve this the NRF24L01 module was used by Mustafa *et al.* (2018) with 100 mW communication power, 2 Mbps transmission rate and strong anti-interference (Mustafa *et al.*, 2018).

The results obtained by Mustafa *et al.* (2018) supported the FEA analysis. Mustafa *et al.* (2018) placed the torque sensor in a test setup (Figure 2.15) and a static analysis was conducted, where a torque wrench was used for the operational verification of the electronics' readout design.

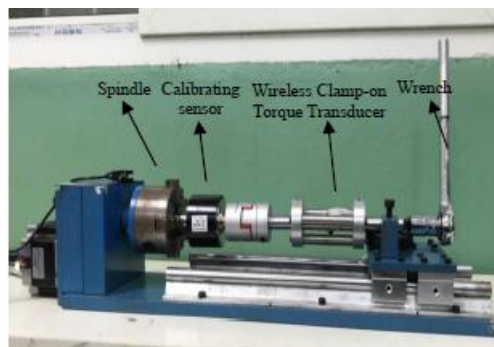


Figure 2.15: Experimental setup, Mustafa *et al.* (2018)

Mustafa *et al.* (2018) concluded that the experimental setup and the validation of the simulated results confirms efficacy of the proposed system as a wireless torque transducer.

Binsfeld Engineering [Online] provided the use of two methods for measuring shaft torque using strain gauges. Both types of gauges can accurately measure strain. The difference is that the one gauge is a specially designed torque sensing strain gauge in full Wheatstone bridge configuration attached directly to the shaft, whilst the other gauge is a combination of four quarter bridge gauges attached to the shaft in full Wheatstone bridge configuration. Essentially both gauges are the same but attaching the four quarter bridge gauges to the shaft provides a greater challenge as the gauges need to be aligned at 90° respectively and at an angle of 45° with the axis of the shaft to ensure accurate measurements.



Figure 2.16: (a) Torque sensing strain gauge in full Wheatstone bridge configuration. (b) Four quarter bridge gauges in full Wheatstone bridge configuration. (Binsfeld Engineering [Online])

2.3 Braking mechanism

The use of a band brake was considered due to its simple, compact and rugged nature, however because a band brake relies on friction they are prone to grabbing or chatter, hence leading to the loss of brake force when hot / heated (Allen, 2018). Due to the nature of this project and accuracy of measurements required, this part of the literature review will focus on the use of magnetic brakes.

Eddy current brakes, which is an alternative to band brakes and known to combat the influence of friction, was studied by (Edwards *et al.*, 1999). Edwards *et al.* (1999) stated that if the field source is a permanent magnet, and the brake is designed to avoid demagnetization, an Eddy current brake cannot fail to operate. The basic structure of a double-linear eddy current brake can be seen in Figure 2.17. The structure consists of two primary iron backing plates, with surface mounted permanent magnet blocks and a secondary non-magnetic reaction plate, which is the moving part. Due to the non-magnetic nature of the secondary plate, there is no normal force acting on it and the braking force is induced by Eddy currents.

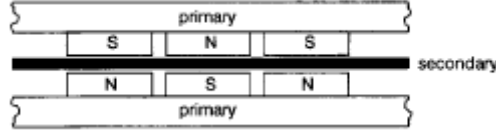


Figure 2.17: Double-sided permanent magnet linear eddy current brake, (Edwards *et al.*, 1999)

Eddy currents are induced in a conductor when it passes through a magnetic field, which creates opposing forces that spin inside the conductor (Smith, 2019). According to Faraday's law, a current is induced when a conductor moves through a magnetic field. In this case the conductor is not a wire through which the current can be directed in a single direction, but rather the current induced swirls around. This phenomenon is referred to as Eddy currents. According to Lenz's law, an Eddy current produces a magnetic field that is in opposition to the magnetic field that produced it, and therefore Eddy currents are an inverse response to the source magnetic field (Smith, 2019).

The basic configuration of a Eddy current brake consists of a rotating non-ferromagnetic conducting disc through a stationary magnetic field. The rotating disc induces Eddy currents, which induces a magnetic field in the opposite direction to that of the stationary magnetic field resulting in a retarding braking force.

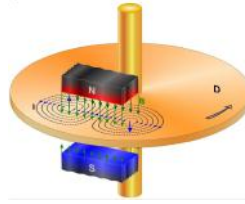


Figure 2.18: Schematic of Eddy currents, (Smith (2019))

Wouterse (1991) derived a theoretical model for eddy current disc brakes operating in the critical speed region in which the braking torque can not only be expressed as a function of magnetic flux and disc speed. Lee and Park (1999) however later derived a model that proved to deliver relatively accurate results in both the low and high speed region.

$$T_b = \sigma R^2 S d \dot{\theta} B^2 \quad (2.6)$$

For the braking torque calculation in Equation 2.6, σ , R , S , d , $\dot{\theta}$ and B represent the disc conductivity ($\frac{S}{m}$), distance between centre of disc and pole centre (m), pole area (m^2) and magnetic flux density (B), respectively.

The braking force of the Eddy current brake relies on the speed of the rotating disc and the strength of the magnetic field, therefore increasing the speed to increase the braking force is not always feasible. An excellent example is magnetic resistance trainers such as spinning bikes. In order to enhance the braking force, one of two options are available. Firstly the use of electromagnets to control strength of magnetic field or the alteration of the magnet orientation or proximity of the magnet to the rotating disc (reducing the air gap).

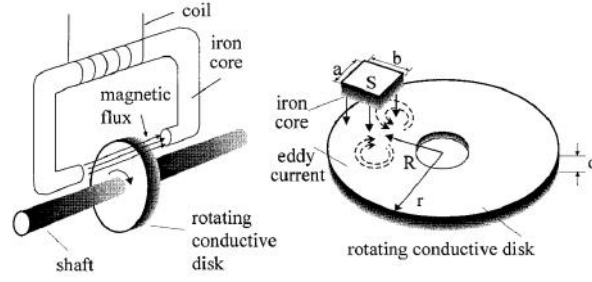


Figure 2.19: Diagram of Eddy Current Brake system (Lee and Park, 1999)

Baharom *et al.* (2011) studied the use of an electromagnet Eddy current braking system. The researchers investigated the use of two different series of aluminium to calculate the difference in braking torque between the two. Different voltages were also applied to the electromagnet, to study the effect that the strength of the magnetic field has on the braking torque.

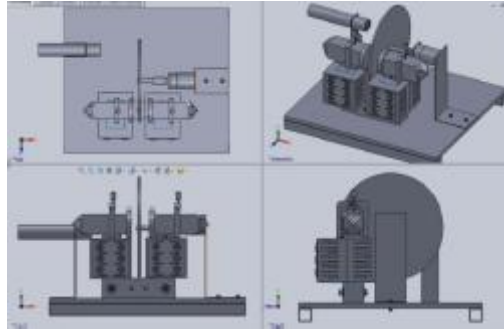


Figure 2.20: Electro magnetic breaking system using Eddy currents, (Baharom *et al.*, 2011)

Another way of adjusting the strength of the magnetic field is by changing the magnetization pattern. The influence a change in magnet orientation has on magnetic field is shown by Jang and Lee (2003).

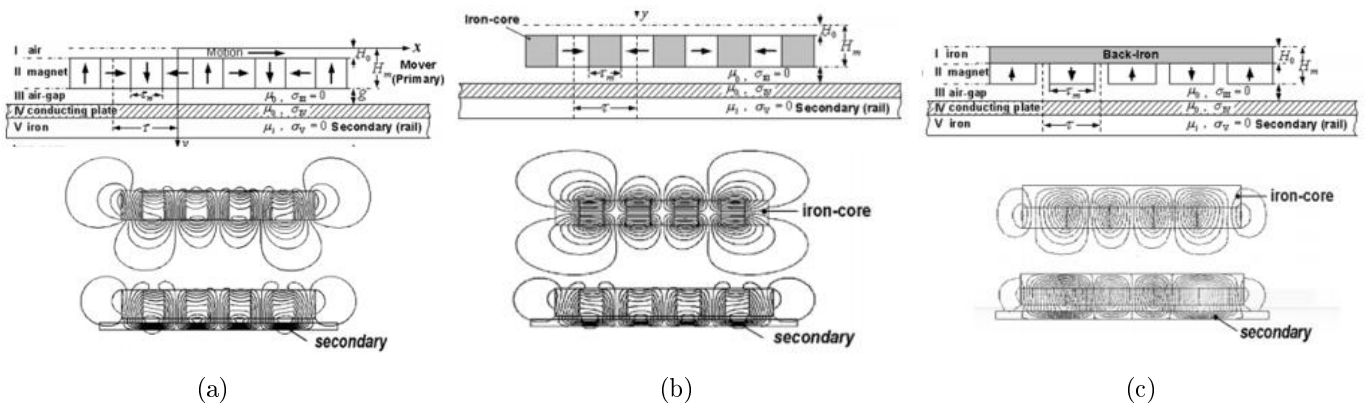


Figure 2.21: Permanent magnet eddy current brake topologies. (a) Halbach magnetization, (b) horizontal magnetization, (c) vertical magnetization, (Jang and Lee, 2003).

2.4 Concluding the literature review

This review gives a brief overview of existing test rigs used to determine bicycle drivetrain efficiencies, along with the methods and technologies applied to measure dynamic torque and induce a braking load in a system. Determining efficiencies of bicycle drivetrains and what affects it, is of great interest to the cycling community. It is believed that when implementing and/or adapting the methods, discussed in the literature review, a bicycle drivetrain test rig capable of measuring small, relative mechanical losses can be produced.

Chapter 3

Technical Design

This chapter stipulates what the technical requirements of the project are, the process that was followed during design, i.e. concept generation and literature review analysis and finally selecting a concept that would achieve the objectives.

3.1 Customer requirements

The customer requirements are obtained from the project brief: “Design a test rig capable of measuring the efficiency of a bicycle drivetrain”. The following customer requirements are established:

- The system needs to be compatible with different drivetrain components, from different manufacturers, i.e. different sized chain rings and cassettes as well as derailleurs.
- The operating range of the system must be similar to that of a cyclist’s output.
- The system operating speed must be similar to that of a cyclist’s input cadence.
- The system needs to be able to accurately measure shaft input- and output shaft torque and speed.
- The brake applied to the output shaft of the system must provide enough resistance to induce a torque at the input shaft similar to that of cyclist’s input torque.

Additionally the system should not be fixed and must be a stand-alone piece of equipment. After completion of the project the system should be available for future use. System components developed should be able to be used in other future projects.

3.2 Engineering requirements

Engineering requirements refer to quantitative measures that need to be met by the system and are obtained from the customer requirements.

Table 3.1: Engineering Requirements

Specification	Quantitative Measure
Power measurement sensitivity	At least 3% power losses between input and output shaft
Maximum input power	At least 200 W
Max operating speed	100 rpm
Variable braking torque	Required
Variable operating speed	Required
Compatible various sized chain rings	Required
Compatible various cassette manufacturers	Required
Compatible various rear derailleurs	Required
Test rig stand-alone piece of equipment	Required

3.3 Concept generation

This chapter describes the concepts that were considered for each subsystem required to achieve the objectives. The focus was placed on the methods employed to measure the variables which are required to calculate power. Each concept is described in detail and analysis of the final concept selection is done in the next section.

3.3.1 Test rig

The test rig itself is the least intricate part of the design. The rig should be able to support both input and output shafts, be a stand-alone piece of equipment and provide safety measures, i.e. a screen protecting the operator from all rotating components.

3.3.2 Brake mechanism

Two options were considered for the braking mechanism. Namely; a permanent magnet- or electromagnetic Eddy current brake and a band brake.

Band brake

Band brakes are used in many mechanical applications. The resistance of a band brake can be adjusted by increasing the tension in the band, either by tensioning the band or brake with a tensioning mechanism or by increasing the weight as described by Killedar (2012). Torque can also be derived directly by multiplying the tension force in the band with the moment arm.

The band would be situated at the end of the output shaft. Band brakes are a good option because it is cheap and fairly easy to implement, but can cause vibration in the system due to grabbing of the band.

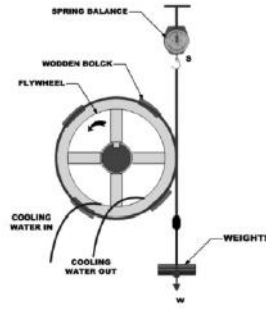


Figure 3.1: Schematic of a band brake dynamometer (Killedar, 2012)

Eddy current brake

The use of magnetic braking due to Eddy currents is not a new technology and is often used in conjunction with band brakes because of its smooth operation and frictionless nature. The drawback however is that magnetic brakes do not have holding torque capabilities.

Eddy current brakes can either be implemented by the use of an electromagnet or the use of multiple permanent magnets. Using an electromagnet is a viable option, but would require additional electronic equipment that would add to the complexity of the system and would incur additional costs. The design considered is a non-ferromagnetic disc, preferably aluminium, rotating between two stationary discs in which permanent magnets are housed. The orientation of the magnet disc holders in relation to each other, will be adjustable in order to alter the amount of magnetic flux density (B) passing through the rotating disc. This would enable the system to have a variable load applied to it. Because the induction of Eddy currents highly depend on the speed of the rotating disc, the speed of the brake shaft would need to be increased by means of a gear reduction.

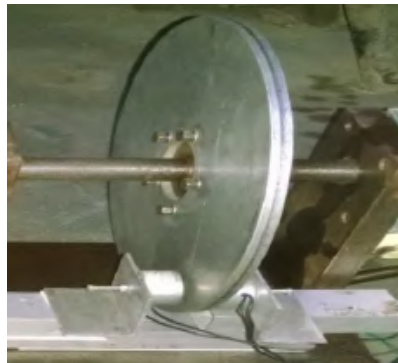


Figure 3.2: Rotor disc with magnets on either side, (Rodrigues *et al.*, 2016)

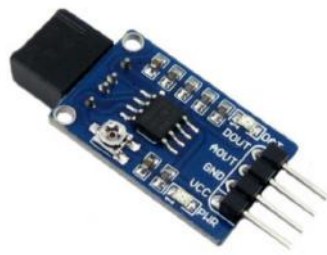
3.3.3 Shaft speed measurement

To determine the input- and output power of the system, the rotational shaft speeds at both ends are required. The systems responsible for measuring speed and torque must be connected to the same data acquisition system. The components considered were chosen

as they would be best suited to use in conjunction with the inexpensive electronics as described in the following sections.

Infrared reflective sensor

Using infrared (IR) reflective sensor to measure rotational speed is a common practice. IR sensors emit infrared radiation and when an object is brought into close proximity of the sensor, the rays are reflected and detected by the IR receiver. In the case of monitoring speed, the IR sensor is placed at the perimeter of the rotating disc and reflective tape is pasted onto the edge of the disc at predetermined incremental values. As the disc rotates and the reflective tape passes the IR sensor, the IR rays are reflected and received by the IR receiver. This generated pulse is subsequently used to determine rotational shaft speed.



(a)



(b)

Figure 3.3: (a) Infrared sensor module, (Micro Robotics [Online]). (b) Tachometer using IR sensor, (Viral Science, The Home of Creativity [Online])

Optical encoder with perforated disc

Using a perforated disc with an optical encoder (photo-interrupter) is also an option. Similar to the IR sensor module considered previously, the optical encoder houses an IR light source and a photo-diode, situated opposite each other. The encoder is placed at the perimeter of the perforated disc, allowing the disc to pass through the light source and photodiode. As the disc rotates and the light is allowed to pass through the module, it outputs a digital high. The opposite is observed when the light source is blocked by the disc and the module outputs a digital low. The digital high and digital low creates a pulse train from which the rotational speed can be derived. This is possible if it is known how many pulses are generated per revolution, which is determined by the amount of perforations in the disc.



Figure 3.4: LED and photodiode module, (Botshop [Online])

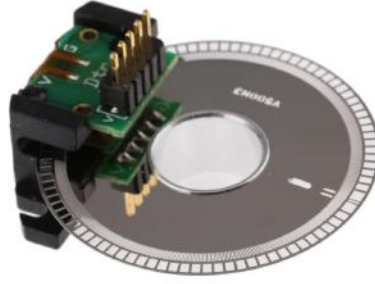


Figure 3.5: Perforated disc in conjunction with optical encoder, (RS Components [Online])

3.3.4 Torque measurement

A motor will be used to supply an input to the system and a brake will be used to induce a load in the system. Therefore a way of measuring torque at both the input and output shafts must be devised.

Industry used in-line torque transducer

An industry-standard HBM in-line torque transducer will be used as the control device to compare with the various torque measuring systems which follow. These transducers are calibrated, very sensitive and extremely expensive. The rig must therefore be designed in such a manner that the in-line torque transducer can be interchangeable between the input and output drive shafts. This will allow for the comparison between the control device and the torque measuring system at the respective shaft ends.



Figure 3.6: T22 HBM in-line Torque Transducer, (HBM [Online])

Measure relative twist angle of shaft by use of zebra tape and optical sensors

Zappalá *et al.* (2018) presented a contactless torque measuring system that does not involve the torque measuring device to be inserted in-line with the rotating shaft. The working principle of this system was explained in Section 2.2. This torque measuring system can be implemented at both the input and output shafts. To accomplish this, zebra tape can be placed around both ends of a long shaft. In addition to the zebra tape, two optical encoders are placed on the ground. This will allow for the measurement of the phase shift between the two ends, both covered in zebra tape, because of the relative angle of twist caused by the induced torque. Refer to Figure 2.4.

Measuring shaft torque directly by using strain gauges

Strain gauges can be applied directly to the shaft to measure torque. The method proposed by Muftah *et al.* (2013) involved attaching a V-shaped strain gauge onto the shaft with each metallic arm at a 45° with respect to the axis of the shaft. One of the pitfalls of these V-shaped strain gauges is that they are very expensive. A possible

alternative was proposed by Mustafa *et al.* (2018), where it was shown that the same functionality can be achieved by making use of four strain gauges in a full Wheatstone bridge configuration. This is further illustrated in Figure 2.16 and Figure 3.7.

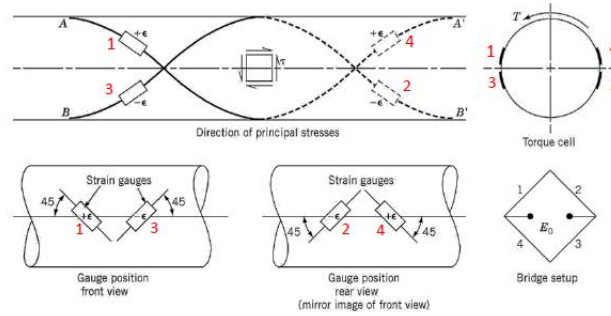


Figure 3.7: Torque sensing strain gauge configuration, (van der Merwe, 2020)

Measuring reaction force caused by motor

Measuring the reaction force experienced by the motor is also a viable option. If a moment arm is somehow connected to the motor base, and the motor base has the ability to swivel about the output shaft's axis. Then a load cell could be attached to the moment arm and the force is then measured at a distance x from the shaft axis to calculate the torque.

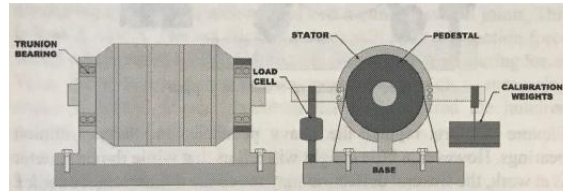


Figure 3.8: Measuring motor reaction force, (Killedar, 2012)

3.4 Concept selection

In this section the final selection for each subsystem was validated. The selection criteria were as follows, manufacturability, cost, reliability and innovation.

3.4.1 Test rig design

The test rig frame will be manufactured from steel square tubing. The rig itself will be a stand-alone piece of equipment capable of being moved around if needed. The rig will allow for a motor to be mounted onto it. This motor will drive a pillow block bearing supported front chain ring, whilst the torque measuring equipment will be placed in-line with the input shaft. The input shaft will then drive a pillow block bearing supported 9 or 10 speed cassette at the output shaft with a rear derailleur suspended from the rear derailleur hanger. The output shaft torque measuring equipment will also be placed in-line with the output shaft whilst a braking mechanism is implemented at the end of the output shaft. Shaft speed measuring equipment will be implemented at the input shaft.

The height of the rig will be approximately 50 cm and as a safety measure, a protective guard will be placed over all rotating components whilst the system is in operation.

3.4.2 Brake mechanism

In the previous “skripsie” project, based on the same topic by McKechnie (2018) a band brake was used. Upon testing it was found that the frictional vibration caused by the gripping of the band, impacted the accuracy of the torque measurement. Therefore it was decided that a permanent magnet Eddy current brake would be used to mitigate the frictional effects. An electromagnetic Eddy current brake was not selected as it would add to the complexity of the system and incur additional costs. The design is based off of the magnetic brake used in resistance trainers in gyms, i.e. spinning bikes.

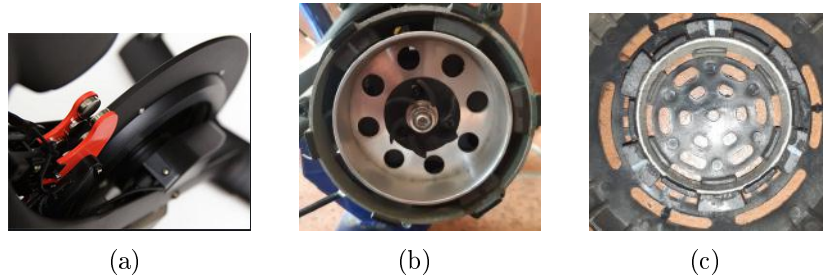


Figure 3.9: (a) Spinning bike braking mechanism, (Indoor Traing Bikes [Online]). (b) and (c) Resistance trainer Eddy current brake mechanism.

The braking mechanism will consist of a spinning non-ferromagnetic disc inside a housing with a stationary disc housing permanent magnets on either side. The number of magnets each disc contains will be able adjustable. Along with the varying number of magnets, the opposing discs will be able to be oriented in two ways namely; (1) with the positive poles of the magnets opposing each other, or (2) will have the positive poles of the magnets on one disc oppose the negative poles on the other disc. This would enable a variable load to be applied to the system, as the resistance is dependant on the magnetic flux density passing through the rotating disc. In position (1) the brake would have the least amount of resistance and in position (2) the maximum amount of braking resistance would be applied.

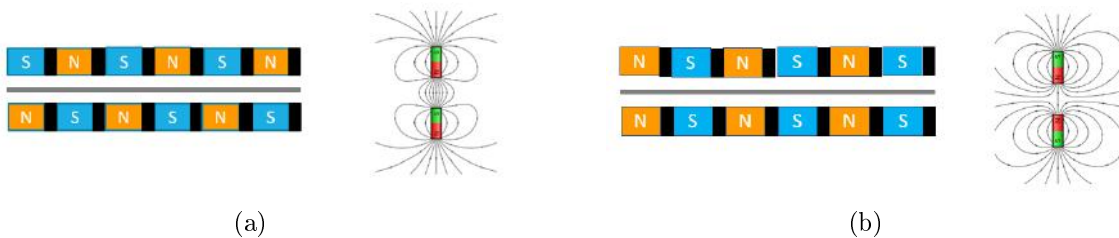


Figure 3.10: (a) Maximum braking resistance magnet orientation and attracting magnetic fields. (b) Minimum braking resistance magnet orientation and repelling magnetic fields. (Wikipedia [Online])

The amount of magnetic resistance experienced due to the induction of eddy currents is highly dependant on the speed of the rotating disc and thus a two stage gear reduction will be implemented at the rear end of the output shaft.

A magnetic brake was chosen as it is often used where frictionless operation is paramount. It is a well understood technology and due to its simple implementation in resistance trainers, seamlessly translates to this project.

3.4.3 Shaft speed measurement

Two methods were devised too measure shaft rotational speed. The chosen method is that of a rotating perforated disc in conjunction with a photo interrupter. This method was chosen as it would be more reliable in measuring real time rotational shaft speed as opposed to using the infrared IR module and reflective tape which is susceptible to ambient light as described by InterlinkKnight (2019)

3.4.4 Torque measurement

The torque at both shafts will be measured by the use of strain gauges as described by Muftah *et al.* (2013) and Mustafa *et al.* (2018). Both of these methods proved reliable and is applicable to the project. An in-line based torque transducer will be developed. It will be in the form of a hollow flanged aluminium tube which will be inserted in-line with both the input and output shafts. The strain gauges will be applied directly to the shaft as performed by Muftah *et al.* (2013), with a full Wheatstone bridge configuration employed. In order to get a measurable reading the voltage signal will be conditioned and amplified by an instrumentation amplifier and microcontroller as performed by Mustafa *et al.* (2018).

Because the shaft will be rotating, there is no possible way to connect the load cell with an external data acquisition system through a wired connection. The signal will thus be interpreted by a microcontroller mounted to the shaft and wirelessly transmitted via a RF transceiver module to the data acquisition system on the ground as demonstrated by Mustafa *et al.* (2018). The reason for choosing this method is that strain gauges are generally very accurate in determining shaft torque and the technology is well understood. The general problem with using strain gauges to measure torque of rotating shafts is the means of transmitting the signal wirelessly. This is usually done in industry by using a v-link, but in our case is very expensive to procure and reasonably big. However, Mustafa *et al.* (2018) proposed using an NRF24L01 transceiver module and obtained accurate results during practical experiments. This thesis will demonstrate the viability of implementing cost-effective electronics for the purpose of measuring dynamic torque. Ideally, this will provide an affordable alternative to the in-line torque transducers which are significantly more expensive.

SAW and fibre-Bragg grating technology was also an option, but its complexity did not make it viable.

Pugh charts depicting the selection criteria for each component can be found in Appendix G.

3.5 Final design

This section gives a detailed description of the final design and explains how each component works and how they interact with each another to achieve the project objectives.

3.5.1 Test rig overview

The test rig frame was constructed from a combination of 38x38x2 mm and 40x40x2 mm steel square tubing. The frame occupies a floor space of 0.64 m². On the drive input end of the test rig provision is made for an electric motor to be mounted onto a plate with slots to allow for axial positional adjustment during assembly. The motor selected for this project is the R27 CMP 63M/KY/RH1M/SM1 (SEW-EURODRIVE) servo motor which is to be controlled by the SEW Movidrive MDX61B (SEW-EURODRIVE) VSD (Variable speed drive). The selected motor was chosen because it has the ability to provide an input torque of 35 Nm at an input speed of 100 RPM to the system when coupled with the VSD, refer to Appendix A for motor selection calculations.

The motor is coupled to the input shaft using jaw couplings to account for misalignment and vibrations. The T22 HBM torque transducer, which is to be used for comparison purposes, is extremely sensitive, therefore even a slight misalignment or vibrations may influence the measured torque. In addition to its sensitivity, this transducer is highly accurate and very expensive and needs to be protected from any potential damage. The torque transducer which was designed for this project is placed in-line with the T22 HBM torque transducer. The designed transducer embodies the shape of a flanged hollow aluminium shaft with strain gauges attached directly to the shaft and electronic components mounted onto the shaft.

Just beyond the second pillow block bearing mounted onto the shaft is the speed sensor perforated disc and spider onto which one or more chainrings can be attached.

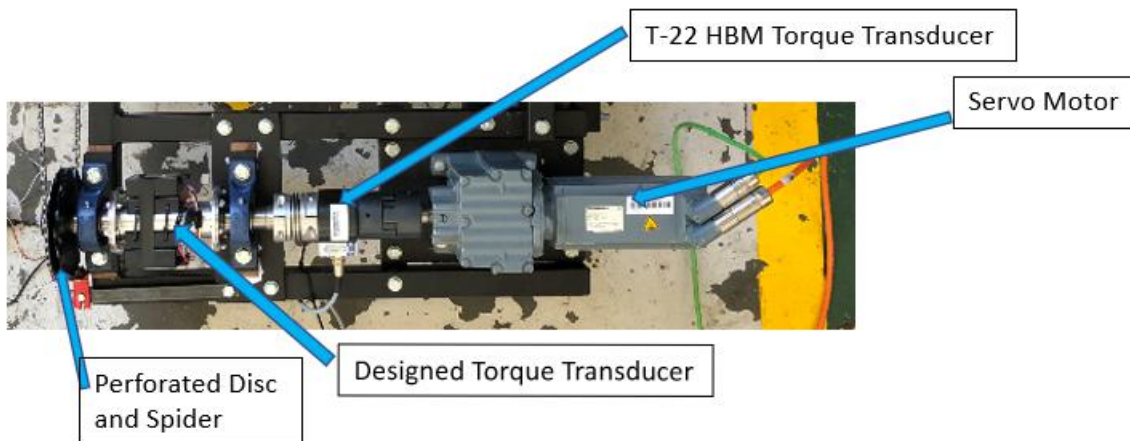


Figure 3.11: Input Shaft.

The input and output shafts are connected by a standard bicycle chain. At the front end of the output shaft, a cassette body is bolted onto the shaft to make provision for the rear cassette. A derailleur arm is bolted onto the frame which essentially acts as the rear derailleur hanger.

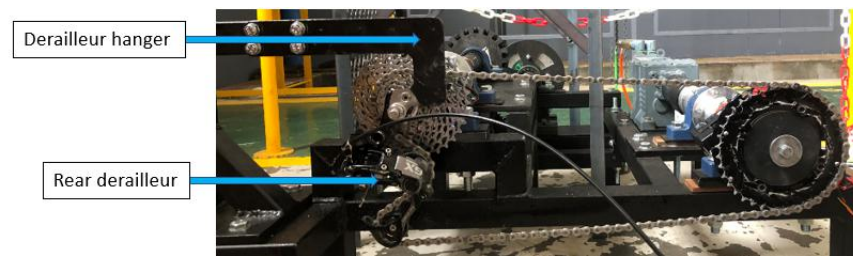


Figure 3.12: Bicycle drive train.

As is the case with the input drive shaft, the proposed torque transducer is placed between two pillow block bearings in-line with the output shaft. Just beyond the second pillow block bearing the output shaft is extended. This extension is interchangeable with the two sets of couplings and T22 HBM transducer used for comparison.

At the end of the output shaft, just beyond the final pillow block bearing, a two stage gear reduction system is introduced to increase the speed of the brake shaft and increase the effectiveness of the Eddy current brake.

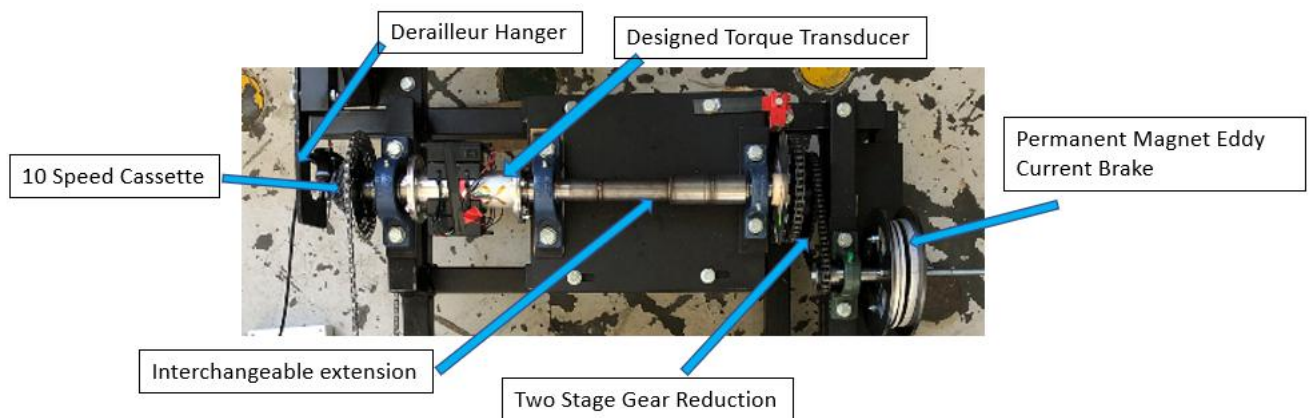


Figure 3.13: Output Shaft.

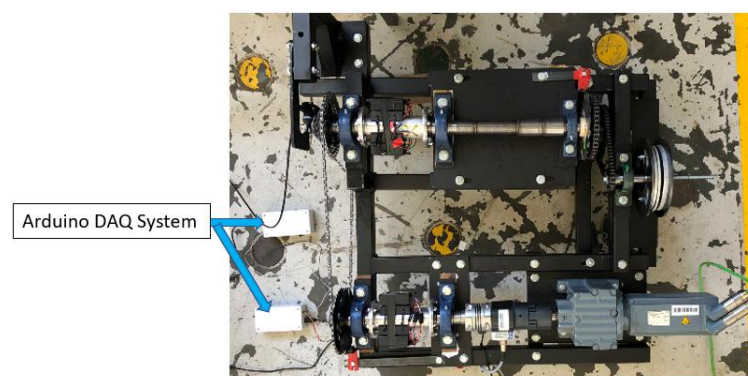


Figure 3.14: Test Rig.

3.5.2 Braking mechanism

The braking mechanism design is divided into two subsections. Gear reduction which allows for the rotating disc to reach an adequate speed so that a retarding force can be induced will be discussed. Secondly, the magnetic brake housing which includes the magnet disc holder and rotating ferromagnetic disc will also be explored.

Gear reduction

The braking force induced by an Eddy current brake is dependant on the speed of the rotating disc as described by Lee and Park (1999).

$$T_b = \sigma R^2 S d \dot{\theta} B^2 \quad (3.1)$$

To achieve the required gear reduction ratio of 1:9 a two stage sprocket gear reduction system was used. Each stage consists of a 15 tooth sprocket being driven by a 45 tooth sprocket, resulting in a gear reduction ratio of 1:3 during each stage.

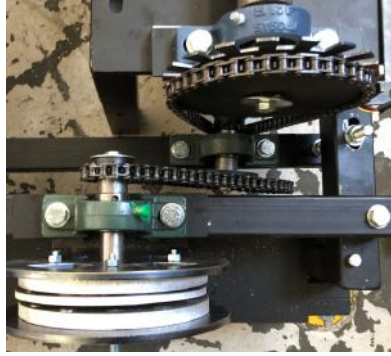


Figure 3.15: Two stage gear reduction at end of output shaft.

Eddy current brake housing

The magnetic brake housing consists of two steel back plates with an aluminium magnet disc holder bolted onto the inside of each back plate, this allows the magnet disc holders oppose each other. One of the magnet disc holders remain fixed, while the other has the ability to rotate in order to adjust the strength of the magnetic field passing through the disc.

Equation 3.1 was used to design the brake. The torque induced by the brake is a product of the disc conductivity (σ), the square root of the distance between the centre of the disc and pole centre (R^2), magnet pole area (S), disc thickness (d), disc speed ($\dot{\theta}$) and the square root of the magnetic flux that passes through the disc (B^2).

Refer to Appendix C for brake design calculations.

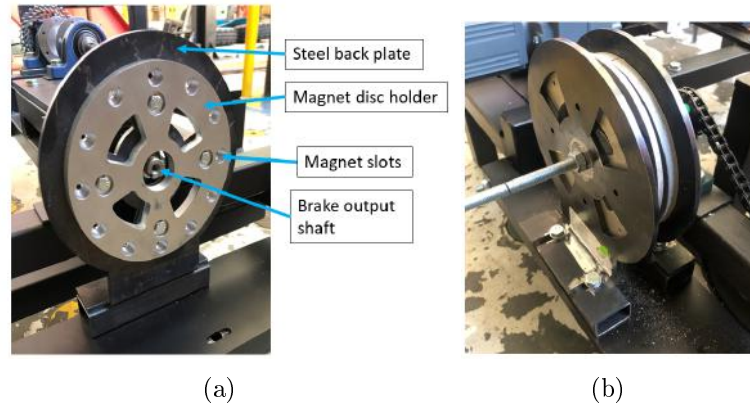


Figure 3.16: (a) Brake housing backplate with one magnet disc holder fastened indicating magnet slots and brake output shaft. (b) Full brake assembly with both magnet disc holders engaged.

3.5.3 Shaft speed measurement

Perforated disc

The perforated disc is constructed from a laser cut 2mm steel plate with 18 slots. The 18 slots would result in 18 pulses per revolution to determine rotational shaft speed. The use of more slots results in an increased sensitivity of the speed sensor.

Electronics

The photo-interrupter is connected to an Arduino Uno which forms part of the data acquisition system. The photo-interrupter module used, has a LM393 comparator. The comparator compares the inverting and non-inverting inputs, and outputs either a digital high (1) when there is no obstruction between the emitting and receiving element of the module, or a digital low (0) when there is an obstruction (RENESAS [Online]). The digital output of the photo-interrupter is connected to Interrupt pin 2 of the Arduino (Digital pin 2). The Interrupt of the Arduino is configured to be rising edge triggered, so that when a slot in the disc passes the emitting and receiving element, allowing light to be transmitted from the LED to the photo transistor, the module outputs a digital high (1) and an interruption is triggered (Sward and Nunley, 2016).

The number of interrupts/pulses which occur in a given time is counted by incrementing a variable using the interrupt service routine. To determine the time elapsed during the counting cycle the `micros()` function is used. The `micros()` function returns the time that has passed since the Arduino board has been switched ON. Calling the `micros()` function before and after the counting cycle and taking their difference, returns the time that has passed during this counting cycle, the period between pulses (InterlinkKnight, 2019). The frequency of the interruptions can then be derived from the period. Finally, by dividing the frequency with the amount of interruptions per revolution (amount of slots in the disc) and multiplying by 60, the shaft speed in RPM can be calculated (InterlinkKnight, 2019). The photo-interrupter module has an operating voltage of 3.3 V to 5 V and is directly connected to the respective pin on the Arduino Uno DAQ system (in this case, 3.3 V), whilst the digital output pin of the photo interrupter module is connected to pins D2 of the Arduino Uno as shown in Figure 3.17.

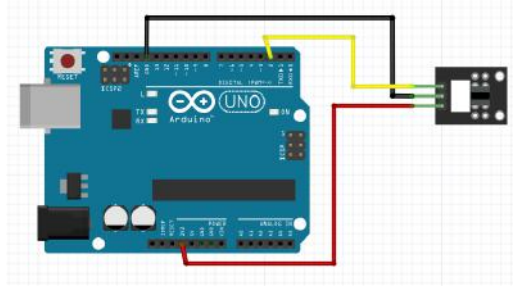


Figure 3.17: Speed sensor electronic components schematic.

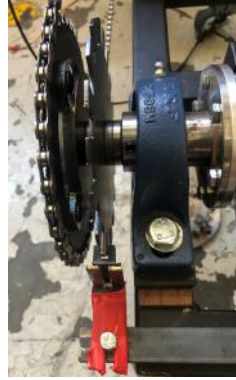


Figure 3.18: Perforated disc in conjunction with photo interrupter module to measure input shaft speed.

3.5.4 Torque measurement

The measurement of torque at both the input and output shafts is done by the proposed in-line torque transducers, making use of strain gauges in a full Wheatstone bridge configuration. Along with an amplifier, conditioning and wireless telemetry circuits are mounted onto the rotating shaft.

Transducer design

The transducer is comprised of a flanged hollow aluminium shaft. Aluminium was chosen as it has a lower shear modulus when compared to steel, it will therefore experience greater surface strain when the same torque is applied when compared to steel. Refer to Appendix B for transducer design calculations.

The dimensions of the transducer are depicted in Table 3.2.

Table 3.2: Transducer dimensions

Tube length	130 mm
Tube OD	50 mm
Tube ID	44 mm
Tube wall thickness	3 mm
Flange diameter	90 mm
Flange thickness	5 mm
Transducer total length	140 mm

The length of the transducer was selected arbitrarily as it needs to be big enough for the required electronic components to be mounted onto the tube and have enough surface area for a full strain gauge Wheatstone bridge.

Strain gauge configuration and application

For each transducer four educational purpose 350 Ω strain gauges are used. The strain gauges are attached to the shaft using the appropriate M-BOND 200 ADHESIVE in conjunction with 200 CATALYST-C. In order to align the strain gauges at exactly 90° with respect to each another and at 45° with respect to the shaft axis. A template as depicted in Figure 3.19 was used to align the strain gauges at 90°. In order to reduce tension in the strain gauge lead wires and protect its fragile soldering tabs, an additional soldering tab strip was attached to the shaft using the same method as applied to the strain gauges.

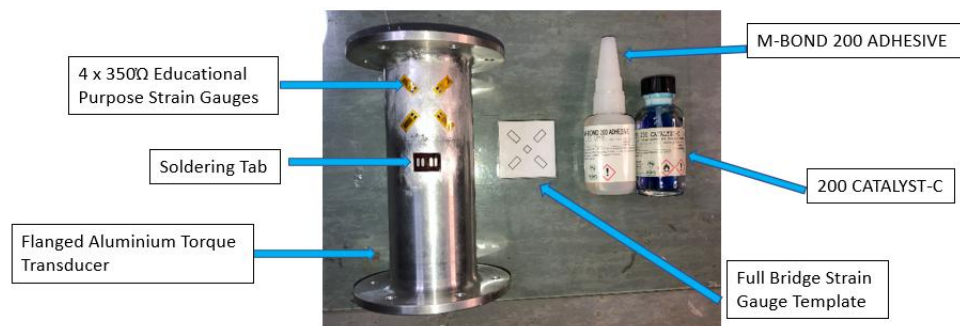


Figure 3.19: Strain gauges attached in full Wheatstone bridge configuration to transducer body.

Electronics

The electronics used to condition, amplify and transmit the strain gauges voltages are off the shelf, readily available components are inexpensive and form part of the wireless telemetry system. The components used for both transducers are listed in Table 4.1.

Table 3.3: Electronic components for both torque transducers.

Component	Function
(NRF24L01 RF 2.4 Ghz Transceiver module) x 2	Transmit transducer torque values wirelessly.
(Sparkfun 24-bit HX711 ADC Load Cell Amp) x 2	Signal conditioning and amplification.
(Arduino Nano) x 2	Microcontroller which processes voltage signal to output a torque value.
(9 V Battery) x 2	Power supply
(2 x Black boxes) x 2	Component housing

The HX711 is a precision 24-bit analog-to-digital converter (ADC) designed to interface directly with a bridge sensor (Avia, 2017). It operates at a supply voltage of 5 V whilst providing a stable excitation voltage of 4.3 V to the bridge sensor.

The module has two differential input channels A and B which is selected by the input multiplexer of the module after which this input is applied to the programmable gain amplifier (PGA) (Microcontrollers Lab [Online]). A fixed gain of 32 is achieved by channel B whilst channel A has a programmable gain of 64 and 128. The measured signal is amplified by the PGA and provides output to the digital interface which converts the analog signal to a digital value and provides serial data at the output (Components 101 [Online]). Pins DOUT and PD_SCK are used for data collection, gain selection, input selection and power down controls (Avia, 2017). When DOUT goes low, it is an indication that data is ready for collection. Data is shifted out from the DOUT pin by applying 25 - 27 positive clock pulses within one conversion period at the PD_SCK pin (Avia, 2017). Each pulse shifts out one bit, starting with the MSB (most significant bit), until all 24 bits are shifted out. The 25th pulse at the PD_SCK will pull DOUT pin back to high (Avia, 2017). The number of input PD_SCK pulses controls the input and gain selection (Avia, 2017). The Arduino Nano microcontroller reads the output of the HX711 module via serial communication. Sampling rate of the HX711 module when using the internal oscillator can either be 10 Hz (RATE=0) or 80 Hz (RATE=1) according to the module data sheet (Avia, 2017). For this application an output data rate of 10 Hz would suffice.

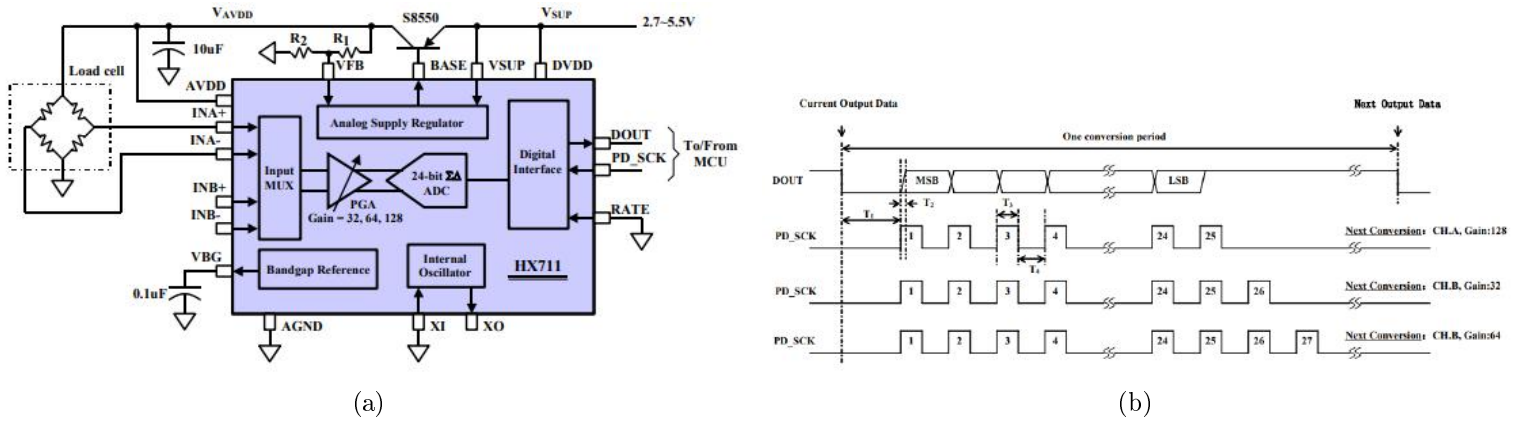


Figure 3.20: (a) Typical weigh scale application block diagram, (Avia, 2017). (b) Data output, input and gain selection, timing and control, (Avia, 2017).

Table 3.4: HX711 Input Channel and Gain Selection (Avia, 2017)

PD_SCK pulses	Input Channel	Gain
25	A	128
26	B	32
27	A	64

The NRF24L01 Wireless RF module is a single chip transceiver designed for operation in the ISM frequency band (reserved internationally for the use of unlicensed low-power devices (LastMinuteEngineers [Online])) ranging from 2.400 - 2.4835 Ghz. The module is widely used in ultra low-power, wireless applications. Parameters like frequency channel, air data rate and output power are configurable by the user. The module supports an air data rate of 250 kbps, 1 Mbps and 2 Mbps (Nordic, 2008). However for this application the default air data rate of 1 Mbps proved to be sufficient. The operating voltage of the module is 1.9 - 3.6 V, however the pins are 5 V tolerant. The module uses a packet structure known as ‘Enhanced ShockBurst’. This payload length specifier of the structure allows for a payload length variation of 1 to 32 bytes, depending on the size of package ready for transmission (LastMinuteEngineers [Online]).

Figure 3.21 depicts a schematic of a single torque transducer and wireless telemetry system. The load cell used in this Figure 3.21 is for illustrative purposes only.

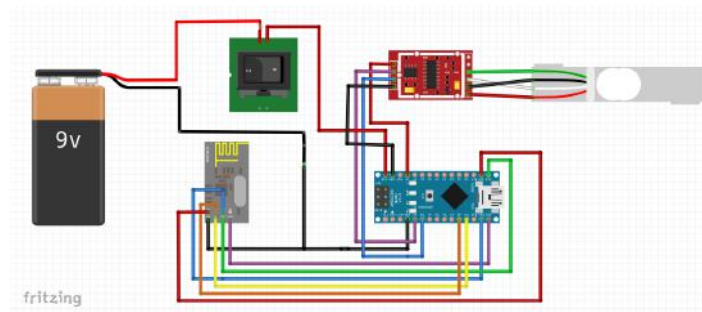


Figure 3.21: Transducer electronics component schematic.

In figure 3.22(a) the fully assembled torque transducer is placed in-line with the input shaft.

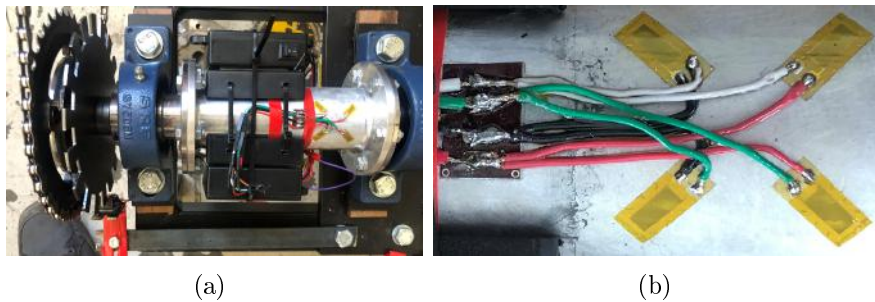


Figure 3.22: (a) Fully assembled torque transducer mounted in-line with the input shaft. (b) Full strain gauge Wheatstone bridge wiring.

3.5.5 Data acquisition

Hardware

The data acquisition hardware comprises of two stationary Arduino Uno modules. The Arduino Uno connected to the photo-interrupter speed sensor, which measures input shaft speed, acts as the master and receives the output torque measurements from the second

Arduino Uno (slave). The master and slave communicate via the TX and RX pins to allow for serial communication between the two Arduino modules. The master Arduino Uno is connected to a PC via a USB 2.0 Type A/B Cable. Both Arduino Uno modules are connected to a NRF24L01 transceiver module to allow for wireless communication with the respective torque transducers.

Table 3.5: Electronic components for Arduino DAQ system.

Component	Function
NRF24L01 RF 2.4 Ghz Transceiver module x 2	Receive measured torque values from the respective shafts wirelessly.
Photo-interrupter module	Count pulses of perforated disc and measure rotational shaft speed.
Arduino Uno x 2	Processes received torque measurements, calculates input shaft speed and transmit data via serial communication.
9 V Battery	Power supply to Arduino Uno 2
2 x White boxes	Component housing

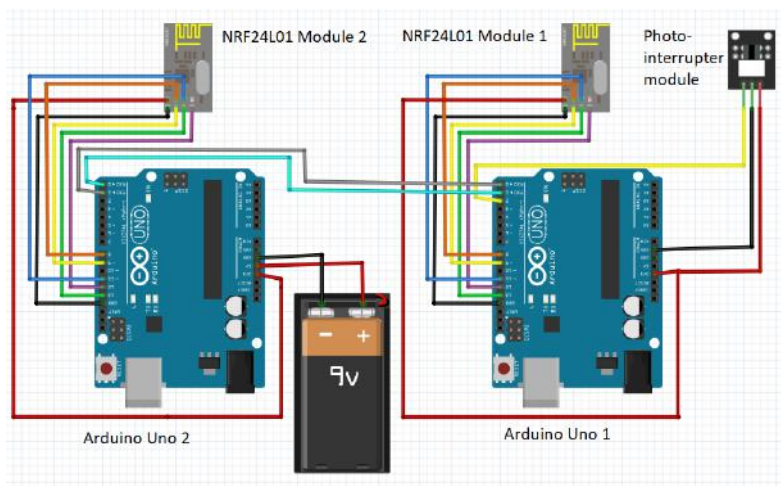


Figure 3.23: Schematic depicting the wire and pin connections of the Arduino DAQ system.

Software, Python data logging

Figure 3.23 shows the full schematic of the Arduino DAQ system. Arduino Uno 2, as shown in Figure 3.23 receives the measured torque values from the output shaft torque transducer and transmits it via serial communication to Arduino Uno 1. At the same time, Arduino Uno 1 receives the measured torque values from the input shaft torque transducer as well as the interrupt signals from the photo-interrupter module. Once the Arduino Uno has received the torque measurements from the input and output shafts, only then does the `micros` function start measuring the time passed per interruption to calculate the input shaft speed in RPM. The calculated input shaft speed is then converted to rad/s by the micro controller. This is achieved by multiplying the RPM value with $2\frac{\pi}{60}$. Because the HX711 load cell amplifier module of the torque transducers

samples at 10 Hz, the input shaft speed is also calculated 10 times per second. Thus the instantaneous input and output torque measurements, as well as the input shaft speed measurements is synchronized. The synchronized data is printed to the serial port of the PC as comma separated values (CSV) (via `Serial.print()` function) at the end of the loop. Output shaft speed and both input- and output power calculations are performed prior to data logging.

To analyse input and output power measurements, to determine drivetrain efficiency, it is necessary to save the data recorded by the system. Data logging is performed using Python. The data is then saved directly to a .CSV file for processing and analysis. A live plot and the Python serial monitor act as user interface.

Flow block diagram

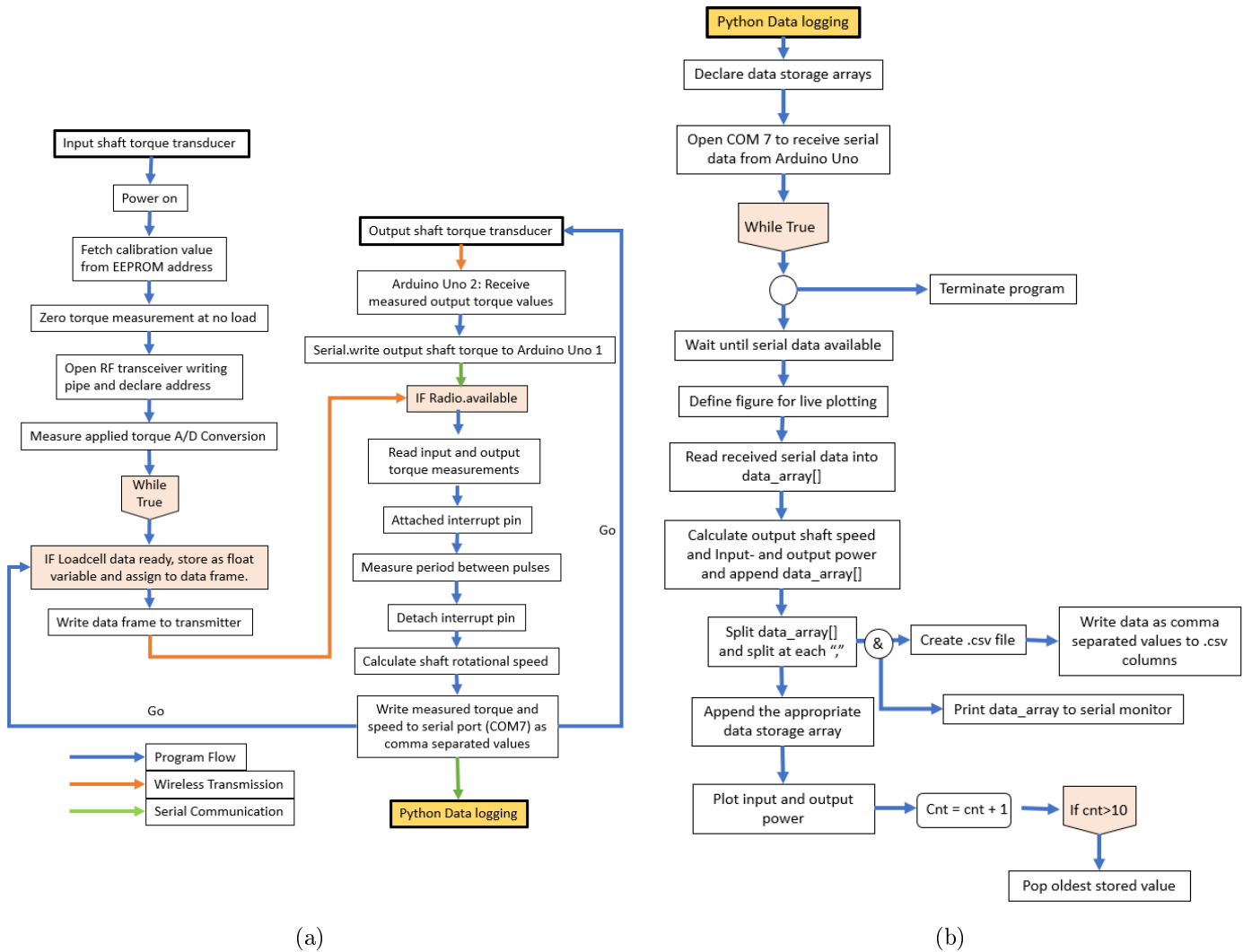


Figure 3.24: (a) Logic flow of Arduino DAQ system. (b) Python data logging logic flow.

Chapter 4

Initial Testing and Calibration

4.1 Shaft speed calibration

A SEW Movidrive MDX61B VSD was used to provide variable speed control to the motor. The VSD interfaces with a PC via serial communication and the motor speed can be adjusted with the SEW MOVITOOLS engineering software. During software setup the gear ratio of the attached gear unit was selected. The software divides the user selected motor speed by the gear ratio and displays the calculated actual output shaft speed. The speed sensor was calibrated by comparing the speed measured by the photo-interrupter with the output shaft speed, which was displayed by the SEW MOVITOOLS software.

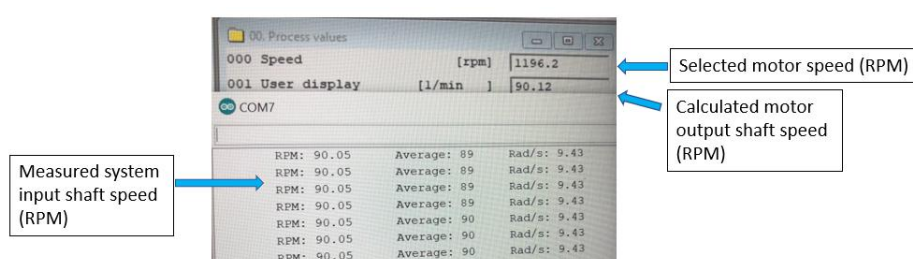


Figure 4.1: Comparing measured shaft speed with actual shaft speed.

The measured input shaft speed was comparable to the actual shaft speed and displayed an average error of $\pm 0.5\%$. This error was satisfactory as the output shaft speed of the system was calculated by multiplying the measured input shaft speed with the selected drive train gear ratio. The power calculated at both the input- and output shafts would therefore slightly increase or decrease simultaneously, without severely influencing the derived efficiency.

4.2 Transducer static calibration

To perform the static calibration procedure, the HX711 Arduino calibration code, provided by Kallhovd (2017) was uploaded to the Arduino Nano which was mounted on the transducer shaft. One flanged end of the transducer was bolted onto a jig, designed so that when the other end is subjected to a torsion force, no moment is induced in the transducer body. This was due to the end, that was subjected to the torsion force, resting on the base of the jig. On the other end of the flanged shaft, a piece of hard wood was fastened onto a plate, which was bolted directly to the flanged shaft. The total length of the hard wood was 1 m in length, extending 0.5 m in both directions, so that the weight of the moment arm would not have to be taken into account during the calibration procedure.

The calibration procedure starts by running the calibration code, after which you are instructed to remove all forces from the end of the moment arm. A known mass was

then applied to the end of the moment arm, inducing a torque in the transducer. In this case a 5 kg weight plate was used for calibration and a 2 kg weight plate used to validate the calibration. The Arduino Nano determines what the calibration factor is and stores it in the EEPROM memory of the Arduino Nano. The static calibration was performed to obtain an estimate of expected calibration factor value. This value can also be adjusted manually, as done during dynamic calibration.

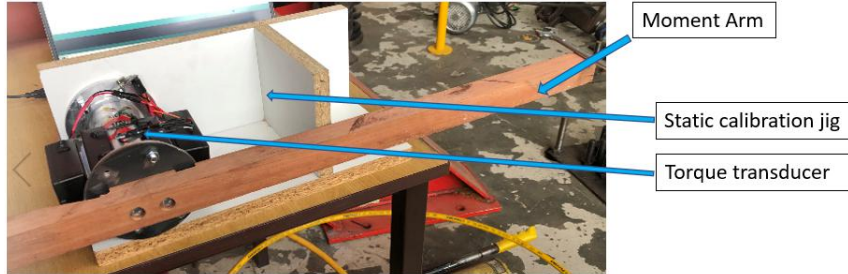


Figure 4.2: Static calibration jig.

Table 4.1: Static calibration results

Applied moment	Measured moment	Percentage error
$5.012 \text{ kg} \times 9.81 \frac{\text{m}}{\text{s}^2} \times 0.5 \text{ m} = 24.58 \text{ Nm}$	24.63 Nm	0.2 %
$2.015 \text{ kg} \times 9.81 \frac{\text{m}}{\text{s}^2} \times 0.5 \text{ m} = 9.88 \text{ Nm}$	10.07 Nm	1.9 %

The design of the proposed torque transducer can be verified by comparing the measured moment to the applied moment. The error present in the measured static calibration values can be due to the moment arm hinging about its axis where it was fastened to plate. This phenomenon changes the length of the moment arm slightly, thus influencing the torque measured. The error is however small enough to be negligible at this stage. The same procedure was followed with the output shaft designed torque transducer.

4.3 Initial testing and troubleshooting

Initial tests were performed before conducting the dynamic calibration procedure. These tests were used to determine whether the system operates as designed as well as identify factors that cause inaccurate/oscillating readings, in order to mitigate them.

4.3.1 Torque measurement errors

Misalignment

The initial tests performed on the output shaft indicated large levels of oscillations present in the measured torque values (Figure 4.3(a)). The tests were performed at an output shaft speed of 40 RPM with no external or braking load applied to the output shaft. Therefore, any load induced in the system is a result of system inertia and bearing friction.

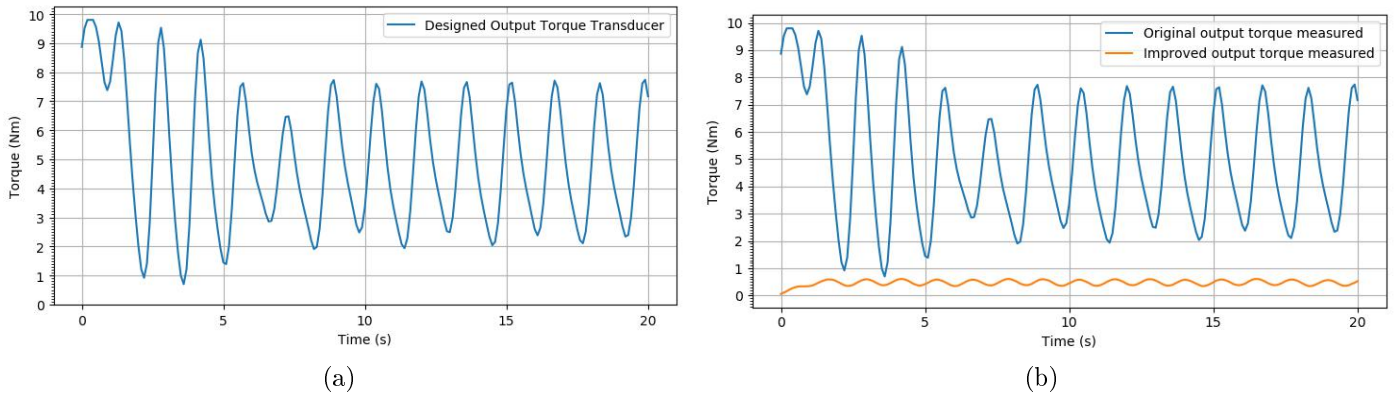


Figure 4.3: (a) Oscillations present in output shaft torque measurement at zero breaking load applied. (b) Reduction in the amplitude of oscillations present in the measured torque values after inserting a shim.

The oscillations observed in the measured torque values had a peak to peak value of ± 6 Nm, which was undesirable and did not meet the engineering requirements. Due to the periodic nature and amplitude of the oscillations it was speculated that the shaft misalignment might be responsible for the undesirable results. The bolts of the centre pillow block bearing on the output shaft, supporting the designed torque transducer, were loosened and the same test was conducted. The results of the second test indicated that the oscillations present in the torque measurements were greatly reduced. These results confirmed our speculation with regards to the shaft misalignment. Feeler gauges were used to determine the space between the centre pillow block bearing and the plate it was fastened to, resulting in a 0.9 mm gap. This problem was overcome by manufacturing a makeshift pillow block bearing shim, made up of a 0.6 mm thick stainless steel sheet and a 0.3 mm thick copper sheet, which was inserted between the bearing housing and base plate.

Figure 4.3(b) shows the effect of the inserted shim on the amplitude of the oscillating torque measurement. The new peak to peak value of the measured torque signal is 0.3 Nm, which translates to a peak to peak power measurement difference of 1.67 W, when the output shaft is rotating at 40 RPM. Although the operating speed and the amount of torque induced in the output shaft did not meet the engineering requirements, the low levels of noise displayed at low speeds and the absence of breaking load, proved to be promising.

4.3.2 Shaft speed measurement errors

The errors present in the shaft speed measurements were slightly more concerning as there was no pattern to the plotted output values, resulting in random noise (Figure 4.4(a)).

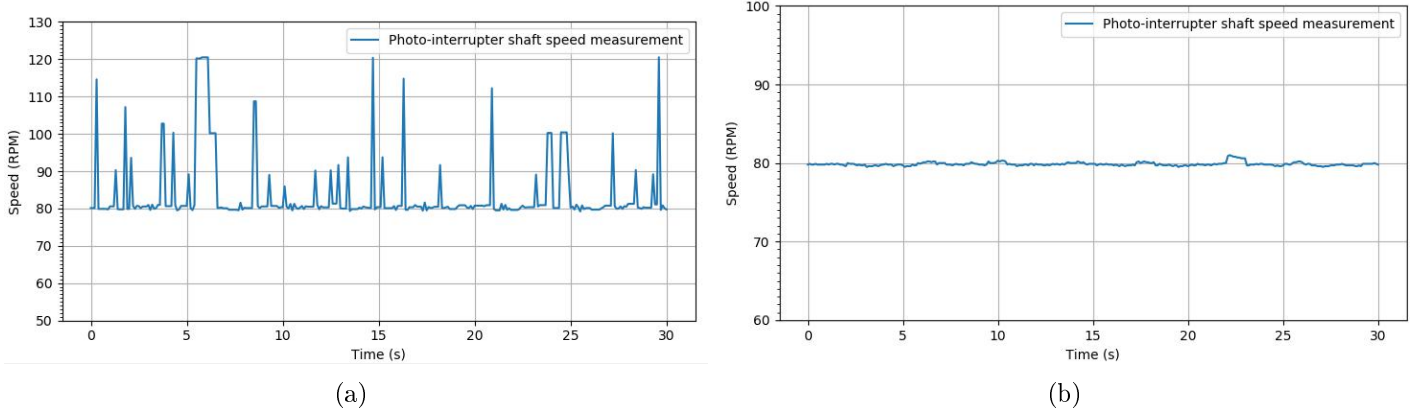


Figure 4.4: (a) Random noise present in the input shaft speed measurements. (b) Reduction in amplitude and frequency of noise present in speed measurements.

It was observed that whenever the variable speed drive (VSD) was switched on and the motor engaged without rotating the shaft speed measured by the photo-interrupter and displayed on the Arduino integrated development environment (IDE) serial monitor would result in random numbers ranging from 0-4000. This however would be impossible as the shaft was not rotating. Further investigation was conducted and the photo-interrupter was removed from the rig and held at a distance. By doing this the random values printed onto the serial monitor disappeared and reverted to outputting 0 RPM, as expected. The photo-interrupter and lead wires were then brought into close proximity of the motor and resulted in random printed values to the serial monitor once again.

The source of the EMI (Electromagnetic Interference) was identified but this posed a challenge when trying to mitigate the source of interference, as the motor needs to be switched on in order for the system to operate. It was also discovered that when any part of the photo-interrupter and/or its lead wires, connected to the Arduino Uno, made contact with the test rig frame, the same noise in the measured RPM value was observed.

It was concluded that the frame of the test rig acted as a conductor of EMI, causing the electronic equipment in contact with the frame to produce inaccurate measurements. A simple, yet effective solution was to insulate the photo-interrupter from any conductive material in contact with the test rig frame, and also ensure that the lead wires did not make contact with the frame. Figure 3.18 shows the photo-interrupter insulated from the frame using insulation tape. The amount of slots present in the disc was also reduced from 18 to 6, using insulation tape. This however slightly reduced the sensitivity of the speed sensor, but provided accurate speed measurements when the system was operating at a constant speed.

The methods used to mitigate the effects of EMI, produced by the motor, proved to be successful, as seen in Figure 4.4(b). A reduced error of 1 RPM was present, which translates to a difference in calculated power of 3 W, when a torque of 30 Nm is induced

at the input shaft whilst rotating at 80 RPM. This was acceptable as the relative error was less than the power measurement sensitivity required ($<3\%$), as stipulated by the engineering requirements, when the system is operating at the expected load ranging between 150 W and 250 W input power.

It is noted that this error is not a regular occurrence and can be reduced by averaging and/or outlier identification techniques during data processing, and can thus be deemed negligible.

4.4 Transducer dynamic calibration

Dynamic calibration of the designed torque transducers was performed by placing both designed torque transducers in-line with the T22 HBM torque transducer at the input end of the system and comparing the torque values measured. This was an iterative process, as the respective designed torque transducers calibration factors were adjusted until its measured values matched that of the HBM T22 torque transducer. Calibration was performed at both 40 RPM and 80 RPM and a constant gear ratio of 38:22, to observe the effect that the input shaft speed and load applied, might have on the noise present in the measured torque. During the placement of both designed torque transducers in-line with the input shaft, great care was taken to ensure shaft and shaft component alignment, as the slightest misalignment would cause a deviation of 1-2 Nm in the measured torque when no load is applied. This might seem like a minor concern, but when the system operates at an input speed of 90 RPM, which translates to 9.42 rad/s, a power measurement error of 9.42 W to 18.84 W can be expected.

When using the on-chip oscillator of the HX711 Load Cell Amplifier module, a sampling rate of either 10 Hz or 80 Hz is possible. The tests would be conducted for an extended period and the system not subjected to sudden changes, therefore a sampling rate of 10 Hz would suffice for this application. The sampling rate of the QuantumX MX440B Universal DAQ used in conjunction with the HBM T22 torque transducers was also set to 10 Hz. The total sampling time used during the calibration procedure was 30 s.

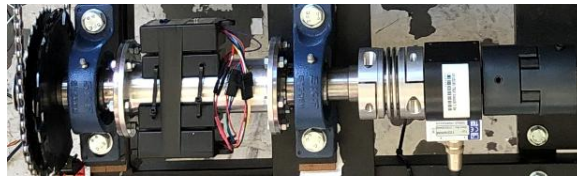


Figure 4.5: Designed torque transducer in-line with the HBM T22 Torque transducer.

Output torque transducer calibration

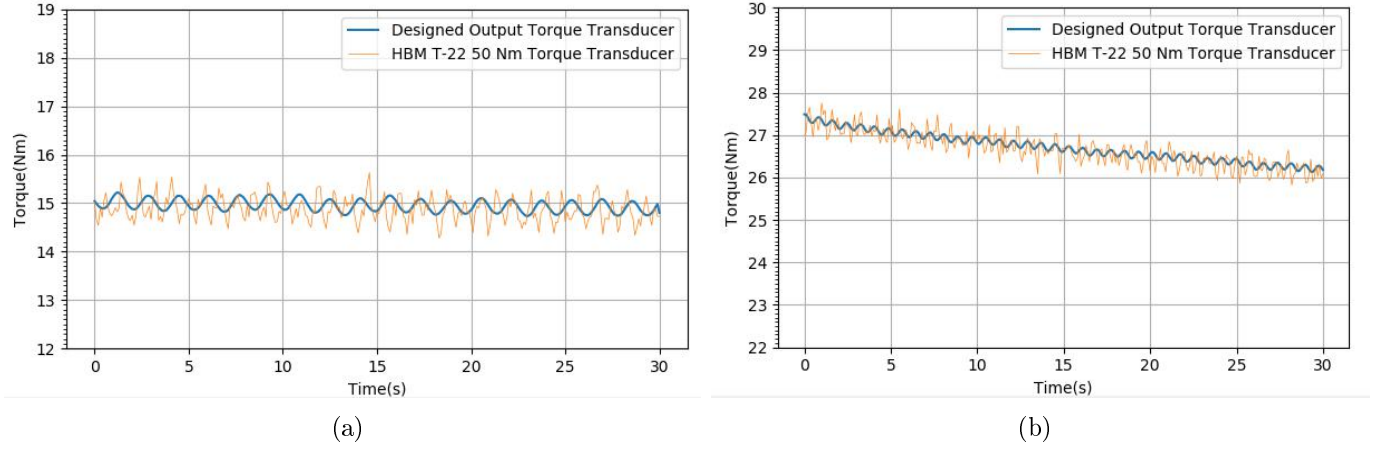


Figure 4.6: (a) Output torque transducer calibration 40 RPM input. (b) Output torque transducer calibration 80 RPM input.

Input torque transducer calibration

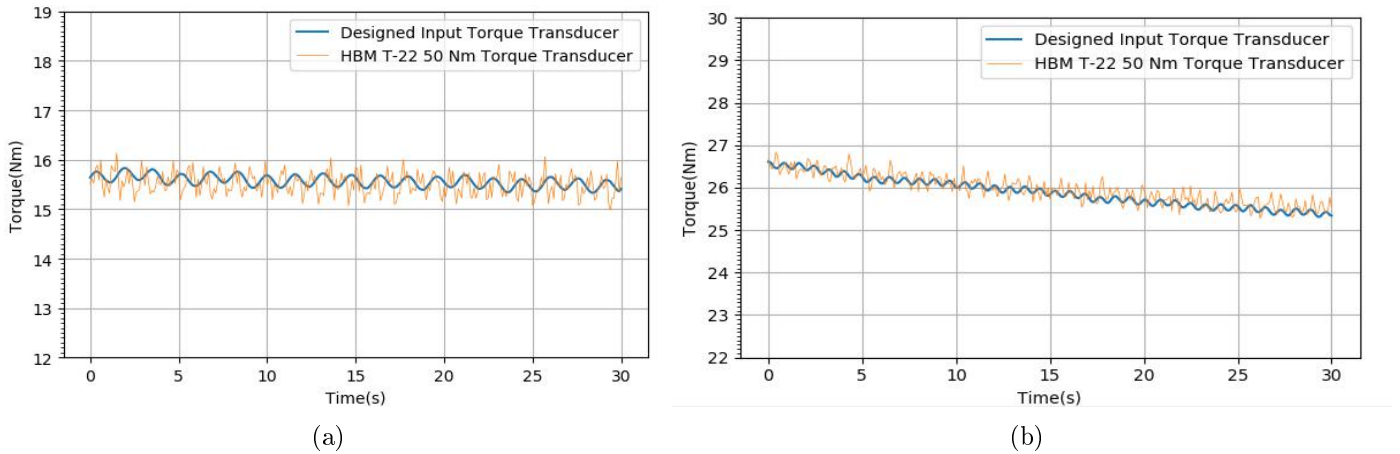


Figure 4.7: (a) Input torque transducer calibration 40 RPM input. (b) Input torque transducer calibration 80 RPM input.

Figure 4.7 illustrates that the designed torque transducers performed well, when compared to the T22 HBM Torque transducer at various motor shaft output speeds. The orientation of the opposing magnet disc holders of the Eddy current brake was held constant during both tests. Because the braking torque induced was dependant on the disc speed, an increased braking torque was induced at higher input speeds. The descending nature of the measured torque at higher input speeds is a result of the kinetic energy of the rotating disc being dissipated as heat, which is generated by the Eddy currents induced in the rotating disc. The strength of the magnetic field is inversely proportional to the temperature which the magnets are exposed to. Therefore an increase in magnet temperature results in a reduction of magnetic field strength. Weaker Eddy currents are induced in the rotating disc, resulting in the decline of the Eddy current brake effectiveness.

Chapter 5

Eddy Current Brake Effectiveness

The effectiveness of the Eddy current brake was examined at three possible magnet disc orientations and three input shaft speeds. A moving average of 10 values was implemented in the Arduino code to further reduce oscillations and improve the accuracy of torque measurements at both the input- and output shafts. The descending nature of the measured torque values at high input shaft speeds and high loads applied to the system, present during the calibration procedure, was reduced by cooling the rotating disc with a blower during operation. This proved to be effective at dissipating the heat caused by the induced Eddy currents in the rotating disc and resulted in a reduction of the torque drift observed. A selected gear ratio of 38:22 was used during all tests in the three prescribed magnet disc holder positions (Figure 5.1).

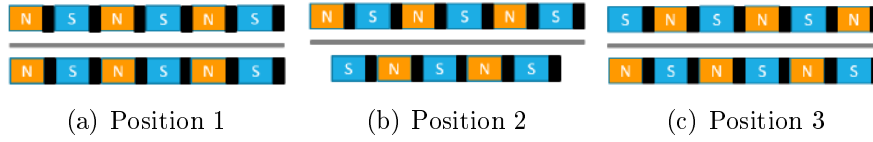


Figure 5.1: Magnet disc holders positions.

Position 1: The opposing magnet poles repel each other, resulting in the least amount of magnetic flux to pass through the rotating aluminium disc, therefore inducing the lowest amount of breaking torque.

Position 2: The poles of the adjustable magnet disc holder is shifted between the opposing magnet poles. This increases the amount of magnetic flux that is able to pass through the rotating aluminium disc, which results in an increased torque induced in the system.

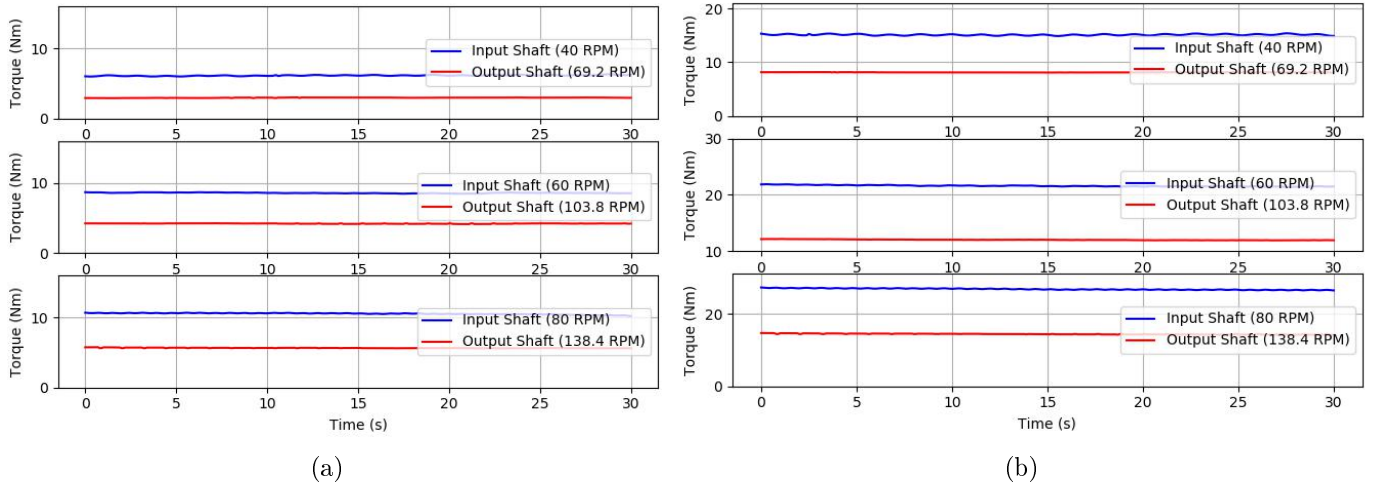


Figure 5.2: Torque induced by Eddy Current Brake in Position 1 (a) and Position 2 (b).

Position 3: The opposing magnet poles attract each other, resulting in the maximum amount of magnetic flux able to pass through the rotating aluminium disc. This results in the maximum amount of torque induced in the system at the selected operating speed and gear ratio. The torque induced in the input shaft exceeded the design specifications of the hollow flanged aluminium tube (35 Nm) and therefore was operated above that load for 1.5 s, as precaution. No damage was incurred to the transducer body as a safety factor of 3.59 was implemented (Appendix B).

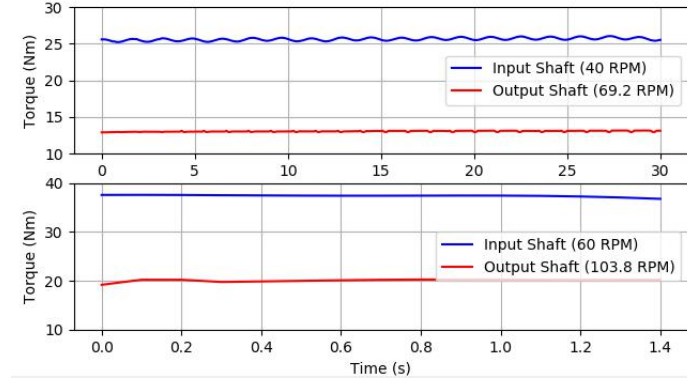


Figure 5.3: Torque induced by Eddy Current Brake in Position 3.

5.1 Brake calculations validation

Figure 5.4 compares the calculated power induced at the input shaft (Appendix C) with the measured power values induced at the input shaft, whilst the system was operating at an input shaft speed of 90 RPM. For this test, one magnet disc holder was engaged and the air gap set to 5 mm in order to validate Equation 3.1 used in Appendix C as described by Lee and Park (1999). An average difference of ± 9.84 W, across all gear ratios, was observed between the calculated and the measured power induced at the input shaft.

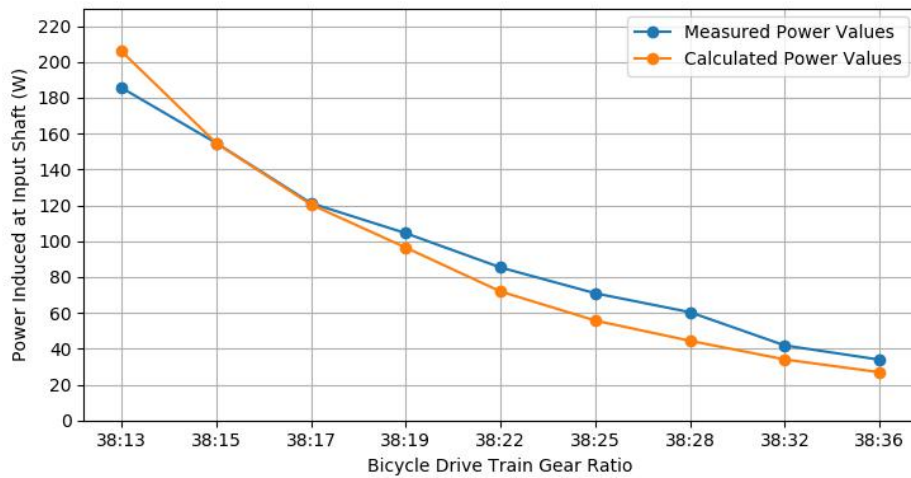


Figure 5.4: Calculated power induced at input shaft vs measured power induced at input shaft.

Chapter 6

Testing

This chapter covers the methods used to process the data obtained from the efficiency tests. The test rig performance is discussed and the results analysed to determine which lubricant (6 options) used resulted in the most efficient bicycle drivetrain.

6.1 Test procedure

To produce repeatable results, a constant procedure was followed when conducting the tests. Before start-up both shafts were unloaded and the torque transducers zeroed, the motor was then engaged (but not rotating). All tests were conducted at an input shaft speed of 90 RPM and a drivetrain gear ratio of 38:36 (1:1.0556). The ramp time of the input shaft (amount of time to reach 90 RPM from a standstill) was also held constant. Once the input shaft reached an operating speed of 90 RPM, data was collected for 60-70 s after which the motor was allowed to come to a standstill and disengaged. The blower used to dissipate the heat generated by the Eddy current brake was implemented during all tests. A series of nine tests per lubricant was performed. For each lubricant tested, the first test was conducted after the Eddy current brake had cooled down and subsequent tests performed at 5 min intervals.

6.2 Data processing

During the nine tests performed per lubricant, outlier tests were identified by inspecting the .csv data files. A test was deemed an outlier if efficiencies of 97%+ were derived. This would be considered elite, as the most efficient chain based bicycle drivetrain possible, a well oiled single speed drivetrain composed of new, unworn components delivers an efficiency of 98.08% (Topf, 2019). The components used during this study was old and worn, hence not able to measure these high drivetrain efficiencies. Whilst the input torque measured remained reasonably constant, higher output torques would occasionally be measured when compared to previous tests. An increase of 1 Nm output torque measured, increases the output power by 9.94 W, which increases the efficiency derived by 5% to 7% when an input load of 165 W to 185 W is applied. The source of these discrepancies could not be identified, but it was speculated that the increased torque induced could be a result of the additional friction caused by the two stage gear reduction system. The remaining tests displayed reasonable repeatability of which five were selected for drivetrain efficiency calculations.

Both the input- and output torque and speed measurements of the respective tests were uploaded to a `pandas.DataFrame` in the Python environment. A maximum and minimum threshold was set to each `pandas.DataFrame` column in order to identify outliers in the torque and speed measurements obtained. The maximum and minimum threshold was set at the 85th- and 15th percentile of the dataset, respectively. Even though speed measurement errors were greatly reduced as described in Chapter 4, the speed sensor module would occasionally measure input shaft speeds above 90 RPM up to a 100 RPM,

for five measurements at a time. The shaft speed was calculated ten times every second and on average this occurred 4-5 times per 60 s test. The effects were mitigated by replacing the outlier measurements, falling below or above the set threshold limits, with the median of the dataset. The only outliers present in the torque measurement data was that of the measured output torque values. These outliers were a result of data lost during serial communication between the two Arduino Uno's, but occurred seldom and with one to two data point at a time. These outliers were replaced with the average between the preceding and succeeding value or the median, if two data points were lost.

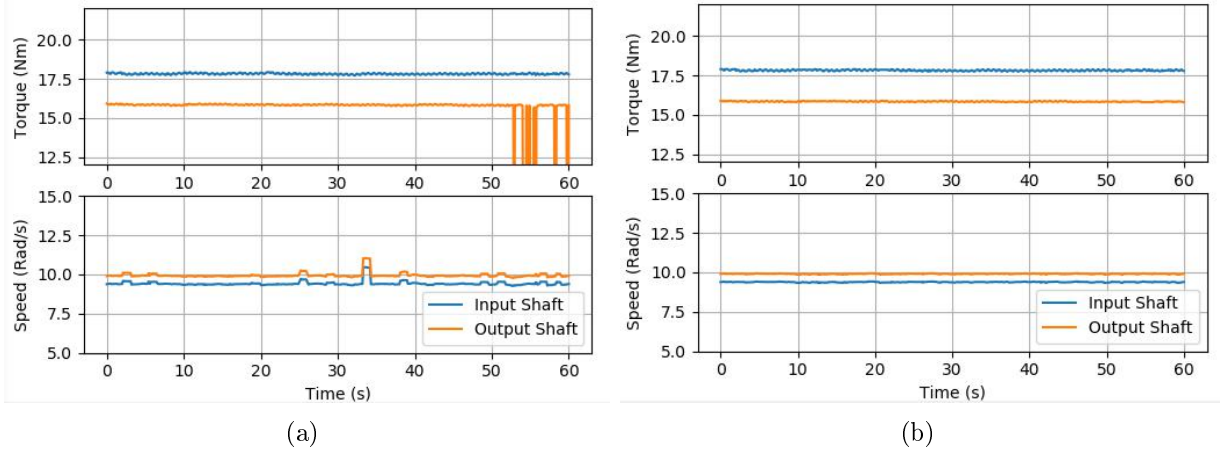


Figure 6.1: (a) Example of dataset pre-processing. (b) Example of dataset post-processing.

6.3 Test rig performance

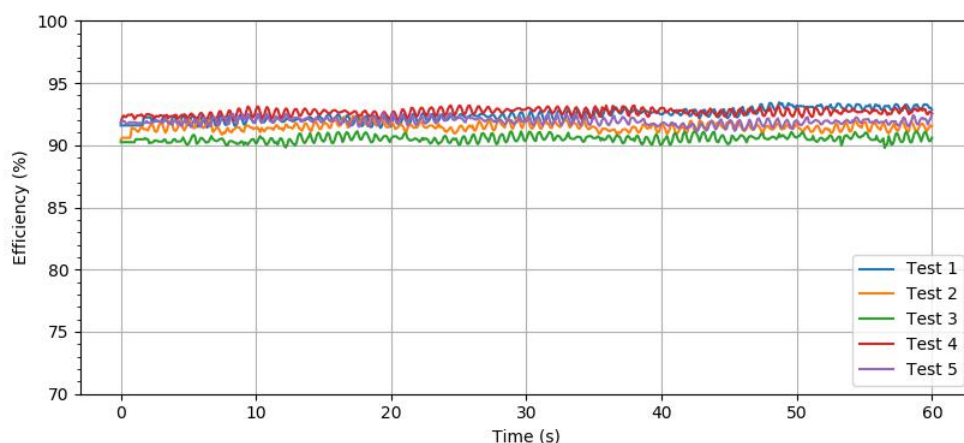
The performance and repeatability of the test rig was investigated by comparing the five tests used for efficiency calculations per lubrication method. Because the temperature of the brake affected the amount of torque induced in either shaft, comparing only the torque measured in either shaft of the five tests directly would not validate the repeatability of the test rig. Therefore the average difference between input and output torque measured per test and the average difference between input and output power calculated was compared. The efficiencies derived from the calculated power values was then compared and ultimately used to determine the repeatability of the test rig. To quantify and visualize test rig's performance, the data obtained from the candle-wax (paraffin wax) coated chain is displayed in Table 6.1, Table 6.2 and Figure 6.2.

Table 6.1: Comparison of difference in input and output torque measured with candle-wax coated chain.

Test no.	Average Input Torque (Nm)	Average Output Torque (Nm)	Difference (Nm)
Test 1	20.74	18.17	2.57
Test 2	19.53	16.93	2.60
Test 3	19.45	16.68	2.77
Test 4	19.04	16.72	2.32
Test 5	19.14	16.67	2.47

Table 6.2: Comparing output losses experienced by the candle-wax coated chain and efficiency derived from each test.

Test no.	Average Input Power (W)	Average Output Power (W)	Average Power Loss (W)	Average Efficiency (%)
Test 1	195.09	180.33	14.76	92.44
Test 2	183.45	167.82	15.62	91.48
Test 3	182.59	165.28	17.30	90.52
Test 4	178.85	165.71	13.14	92.65
Test 5	179.78	165.23	14.52	91.92
			Average	91.80

**Figure 6.2:** Candle-wax coated chain efficiency tests.

Comparing the efficiencies derived from each of the five tests conducted for a candle-wax coated chain a standard deviation of 0.85 % was observed and a coefficient of variation of 0.93 % calculated. This indicated low variance in the calculated efficiency of the series of tests conducted. Thus it can be conclude that the test rig is repeatable to a certain extent when excluding outlier tests.

6.4 Efficiency tests using different lubricants

According to Chester and Berto (2001), bicycle drivetrain efficiencies can range between 80% and 98%, depending on the condition of the components, gear ratios and the load applied. Power losses can be divided into two types. The first type is power dependant losses, which are losses created by friction of the moving parts under a driving load, i.e chainlinks, gears, bearings etc. The quantity of the losses are proportional to the load applied (Rohloff and Greb, 2003). The second type is power independent losses, which are created by friction of the moving parts under load but remain constant regardless of the load applied, i.e. gaskets and shims (Rohloff and Greb, 2003). By changing the lubricant we were able to quantify the the relative frictional losses incurred by the chain and chain rings, i.e dependant losses.

A selection of lubricants (6.3), with varying applications were tested and compared to determine which lubricant resulted in the most efficient drivetrain. The chain and chain rings were thoroughly cleaned and degreased before applying each lubricant before conducting the tests as described in section 7.1. The efficiencies were calculated using the average efficiency of all five tests from each lubricant. The efficiency for each test was calculated using 2.1.

Table 6.3: List of lubricants tested and efficiencies calculated with standard deviation between tests.

Lubricant	Efficiency (%)	Standard deviation (%)
Degreased	89.0	1.25
Candle-wax (paraffin wax)	91.8	0.85
“Squirt Dry Lube”	93.58	2.05
“Total Motor Oil”	93.08	0.85
Multipurpose Tool Oil	92.24	2.23
Q-20	90.13	1.37
“Vaseline” Petroleum Jelly	91.48	1.51

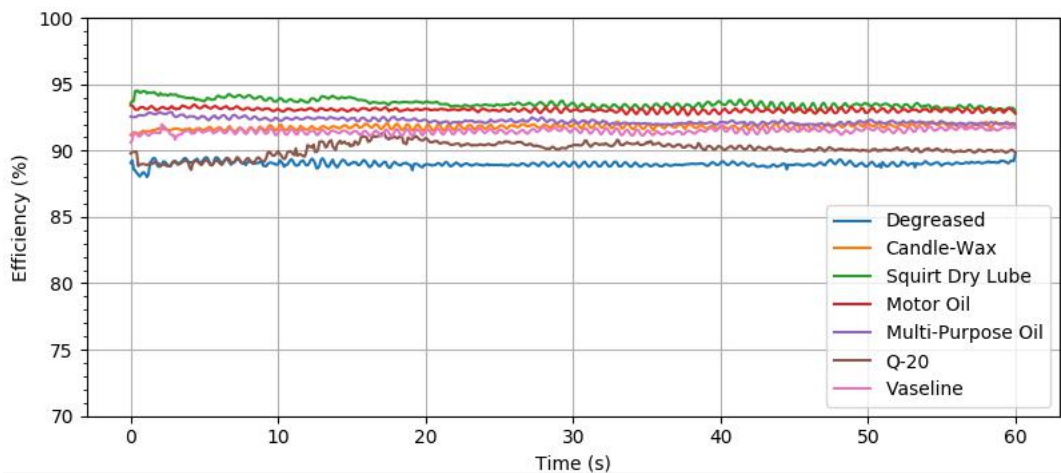


Figure 6.3: Average efficiency measured over time.

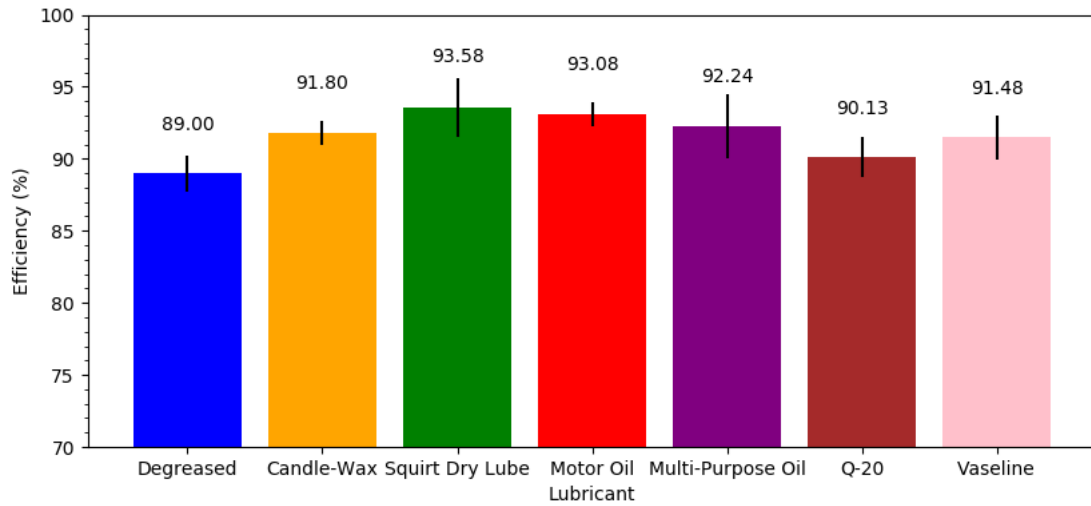


Figure 6.4: Average efficiency of drive with train error bar indicating the standard deviation between the five tests conducted per lubricant.

As expected the degreased chain performed the worst with an average efficiency of 89%. The increased losses are a result of the increase in coefficient of friction between the chainlinks and between the chain and chainrings. As observed in Figure 6.4 the use of any form of lubrication resulted in an increase in drivetrain efficiency, by reducing the coefficient of friction. The “Squirt Dry Lube”, which is a lubricant purposely made for a bicycle chain performed the best with an increase in efficiency of 4.58% compared to the degreased chain resulting in a drivetrain efficiency of 93.58%. Of the investigated, which are not purposely made for bicycle chains, “Total Motor Oil” performed the best.

It should be taken into account that the efficiencies derived are relative as there are other mechanical losses present in the system. These additional losses are caused by the shaft support bearings. Therefore, only the relative improvement can be measured by using different lubricants, but not the absolute drivetrain efficiency.

Bicycle drivetrain efficiency tests conducted by Chester and Berto (2001) at an output load ranging between 150 W and 200 W with similar gear ratio (1:1) yielding efficiencies between 92% and 95%, which are comparable to the efficiencies derived in this study, when only considering the lubricated chain. McKechnie (2018) reported higher efficiencies for the degreased (93%) and the lubricated (96%) chain at a slightly lower output load and a different gear ratio of 22:12. Therefore, the amount of torque applied at either the input- and output shaft would be less compared to our current study and ultimately result in a decreased chain tension. This however contradicts the findings of Spicer *et al.* (2000), where an increase in sprocket size and chain tension leads to a more efficient drivetrain. This would suggest that the test rig used in this study might be under performing and should therefore be investigated.

6.5 Suggested further work

This section provides recommendations for further work on the test rig to increase the test rig performance.

An Eddy current brake was used to mitigate the effects of vibrations caused by the gripping of a band brake, and would have resulted in noisy torque measurements. The choice was justified considering the lack of noise in the torque measured. The Eddy currents had an unpredictable heating effect on the effectivity of the brake, therefore making it challenging to apply a constant load during the tests. A fan was used to dissipate some of the heat, which improved the variability observed, but there was still some concern when comparing all the tests conducted. Future work would include the determination of an optimal operating brake temperature which would provide a constant load at a set disc speed as well as implementing a cooling system capable of maintaining a pre-determined brake temperature. A portion of the brake disc could be submerged in a water bath, with a pump circulating cold water through ensuring constant operating brake temperature thus inducing a constant load. The entire brake mechanism would however need to be concealed in a box to avoid the electronic equipment from getting wet and causing it to surge.

Another factor that could influence the output torque measured is the two stage gear reduction system, comprised of sprockets and chains. A possible solution would be the implementation of a pulley and belt gear reduction system which would result in a smoother operation, but would unfortunately incur additional costs.

Although the torque measurements were reasonably stable, adding a separate +5 V regulator to the HX711 module could reduce the fluctuating torque measurements as reported by Circuits4You [Online].

Rewiring of the photo-interrupter speed sensor module using shielded cabling should increase the reliability of the module by avoiding signal interference.

Chapter 7

Conclusion

The aim of this project was to design, manufacture and test a device that can accurately measure drivetrain losses for a bicycle. This included the design of a test rig frame, a motor driven bicycle drivetrain, the implementation of a braking mechanism to induce a load in the system and a means of measuring input- and output shaft torque and speed to calculate power which was used to determine drivetrain efficiency. The project was not dependant on the use of expensive measuring equipment and software, but rather made use of off the shelf electronics and open source software.

The designed test rig, driven by an electric servo motor was capable of measuring input- and output shaft torque and speed accurately, to determine drivetrain efficiency. A permanent magnet Eddy current brake, applied to the rear of the output shaft was able to induce a variable load in the system by adjusting the magnet disc holder orientation. This enabled the system to operate at various input shaft speeds and selected gear ratios, while inducing a load in the system comparable to a bicycle drivetrain. The spider, located at the front of the drivetrain was designed to be compatible with various chain ring sizes while 9 or 10 speed cassettes could be mounted onto the output shaft's rear hub. Various rear derailleur models can also be mounted onto the designed adjustable rear derailleur hanger.

The use of off the shelf electronics to measure speed and torque proved to be challenging. However, once sources, resulting in inaccurate measurements, were mitigated the designed torque transducer and photo-interrupter speed sensor module was reliable. As predicted, the designed Eddy current brake reduced the amount of vibration induced in the system, which produced a smooth torque measurement. Although the photo-interrupter speed sensor module occasionally measured higher speeds than expected, the effects thereof were mitigated during data processing by implementing outlier identification techniques in the Python environment. The Arduino DAQ system used, exceeded expectations as it was able to flawlessly receive the measured input- and output torque measurements via wireless RF transmission whilst measuring input shaft speed and transmitting the measured data via serial communication to the Python environment for data logging.

A good understanding of the effects that mechanical defects can have on the accuracy of measurements was obtained and an appreciation for precision engineering developed.

Drivetrain efficiency tests, at constant input shaft speed and drivetrain gear ratio, using different lubricants was conducted to determine which lubricant resulted in the most efficient drivetrain. The lubricants tested included motor oil, candle-wax (paraffin wax), multi-purpose tool oil, "Vaseline" (petroleum jelly), Q20 and "Squirt dry lube". Of the lubricants tested, the use of "Squirt dry lube" was the most efficient while Q20 proved to be the least efficient.

The rig proved to be repeatable when discarding outlier tests (efficiencies measured above 97%) as those high efficiencies derived were not possible with this test rig setup.

Possible further work would aid the system in its ability to measure higher relative

efficiencies and would not be limited to testing different lubricants. These suggested improvements, referring to the Eddy current brake, when implemented correctly can reduce variability in the braking load applied and produce more repeatable results.

All project objectives were met. The use of off the shelf electronics to measure dynamic torque was validated by accurate torque measurements. In conclusion, a cost effective means of measuring bicycle drivetrain losses was established.

Appendix A

Motor Selection Calculations

Motor Selection Calculations

Gearbox ratios of possible servo motors available at Stellenbosch University's Engineering Faculty.

$GR_{1M} := 13,28$ Motor 1 R27 CMP63M/KY/RH1M/SM1

$GR_{2M} := 6,59$ Motor 2 R27 CMP40M/KY/RH1M/SM1

$$GR_{DT} := \begin{bmatrix} GR1 & GR2 & GR3 & GR4 \\ \frac{38}{11} & \frac{30}{11} & \frac{38}{42} & \frac{30}{42} \end{bmatrix}$$

Standard maximum and minimum MTB gear ratios

The numerator indicating the amount of teeth on the chainring and the denominator indicating the amount of teeth on the rear cassette chainring.

Standard cycling cadence

$$n_{in} := \begin{bmatrix} 40 \\ 60 \\ 80 \\ 100 \end{bmatrix} \text{ rpm}$$

Required motor input speed

$$n_{motor1} := GR_{1M} \cdot n_{in} = \begin{bmatrix} 531,2 \\ 796,8 \\ 1062,4 \\ 1328 \end{bmatrix} \text{ rpm} \quad n_{motor2} := GR_{2M} \cdot n_{in} = \begin{bmatrix} 263,6 \\ 395,4 \\ 527,2 \\ 659 \end{bmatrix} \text{ rpm}$$

Output shaft speed

$$n_{out} := n_{in} \cdot GR_{DT} = \begin{bmatrix} 138,1818 & 109,0909 & 36,1905 & 28,5714 \\ 207,2727 & 163,6364 & 54,2857 & 42,8571 \\ 276,3636 & 218,1818 & 72,381 & 57,1429 \\ 345,4545 & 272,7273 & 90,4762 & 71,4286 \end{bmatrix} \text{ rpm}$$

Shaft speed at rear end of bicycle drive train

$$n_{in,rad} := n_{in} = \begin{bmatrix} 4,1888 \\ 6,2832 \\ 8,3776 \\ 10,472 \end{bmatrix} \frac{\text{rad}}{\text{s}} \quad n_{out,rad} := n_{out} = \begin{bmatrix} 14,4704 & 11,424 & 3,7889 & 2,892 \\ 21,7055 & 17,136 & 5,6848 & 4,468 \\ 28,9407 & 22,8479 & 7,5797 & 5,984 \\ 36,1759 & 28,5599 & 9,4746 & 7,48 \end{bmatrix} \frac{\text{rad}}{\text{s}}$$

Torque

Input torque at chainring on drive shaft

$$P_{in} := \begin{bmatrix} 100 \\ 150 \\ 200 \\ 300 \end{bmatrix} \text{ watt}$$

Nominal power exerted by cyclist

$$\text{for } i \in [1..4] \quad T_{in} := \frac{P_{in}}{n_{in,rad_i}}$$

A cyclist outputting 200 W at 60 RPM would induce a torque of 31.831 Nm.

Input Shaft Speed 40 RPM 60 RPM 80 RPM 100 RPM Nominal power exerted

$$T_{in} = \begin{bmatrix} \begin{bmatrix} 23,8732 \\ 35,8099 \\ 47,7465 \\ 71,6197 \end{bmatrix} & \begin{bmatrix} 18,9155 \\ 28,8732 \\ 31,831 \\ 47,7465 \end{bmatrix} & \begin{bmatrix} 11,9366 \\ 17,9049 \\ 23,8732 \\ 35,8099 \end{bmatrix} & \begin{bmatrix} 9,5493 \\ 14,3239 \\ 19,0986 \\ 28,6479 \end{bmatrix} \end{bmatrix} \text{ Nm}$$

100 W
150 W
200 W
300 W

Torque induced at driven shaft

$eff := 100\%$ Assuming 100% Drive Train Efficiency

$$P_{out} := eff \cdot P_{in} = \begin{bmatrix} 100 \\ 150 \\ 200 \\ 300 \end{bmatrix} W$$

Output torques for various gear ratios, input torques and shaft speeds.

GR1		GR2		GR3		GR4	
for $u \in [1..4]$		for $u \in [1..4]$		for $u \in [1..4]$		for $u \in [1..4]$	
$T_{out\ u\ 1} := \frac{P_{out}}{n_{out,rad\ u\ 1}}$		$T_{out\ u\ 2} := \frac{P_{out}}{n_{out,rad\ u\ 2}}$		$T_{out\ u\ 3} := \frac{P_{out}}{n_{out,rad\ u\ 3}}$		$T_{out\ u\ 4} := \frac{P_{out}}{n_{out,rad\ u\ 4}}$	
$T_{out\ 1\ 1} = \begin{bmatrix} 6,9107 \\ 10,366 \\ 13,8214 \\ 20,732 \end{bmatrix} Nm$	$T_{out\ 2\ 1} = \begin{bmatrix} 4,6071 \\ 6,9107 \\ 9,2142 \\ 13,8214 \end{bmatrix} Nm$	$T_{out\ 3\ 1} = \begin{bmatrix} 3,4553 \\ 5,183 \\ 6,9107 \\ 10,366 \end{bmatrix} Nm$	$T_{out\ 4\ 1} = \begin{bmatrix} 2,7643 \\ 4,1464 \\ 5,5285 \\ 8,2928 \end{bmatrix} Nm$	$T_{out\ 1\ 2} = \begin{bmatrix} 8,7535 \\ 13,1303 \\ 17,507 \\ 26,2606 \end{bmatrix} Nm$	$T_{out\ 2\ 2} = \begin{bmatrix} 5,8357 \\ 8,7535 \\ 11,6714 \\ 17,507 \end{bmatrix} Nm$	$T_{out\ 3\ 2} = \begin{bmatrix} 4,3768 \\ 6,5651 \\ 8,7535 \\ 13,1303 \end{bmatrix} Nm$	$T_{out\ 4\ 2} = \begin{bmatrix} 3,5014 \\ 5,2521 \\ 7,0028 \\ 10,5042 \end{bmatrix} Nm$
$T_{out\ 1\ 3} = \begin{bmatrix} 26,3862 \\ 39,5793 \\ 52,7724 \\ 79,1586 \end{bmatrix} Nm$	$T_{out\ 2\ 3} = \begin{bmatrix} 17,5905 \\ 26,3862 \\ 35,1816 \\ 52,7724 \end{bmatrix} Nm$	$T_{out\ 3\ 3} = \begin{bmatrix} 13,1931 \\ 19,7897 \\ 26,3862 \\ 39,5793 \end{bmatrix} Nm$	$T_{out\ 4\ 3} = \begin{bmatrix} 10,5545 \\ 15,8317 \\ 21,109 \\ 31,6635 \end{bmatrix} Nm$	$T_{out\ 1\ 4} = \begin{bmatrix} 33,4225 \\ 50,1338 \\ 66,8451 \\ 100,2676 \end{bmatrix} Nm$	$T_{out\ 2\ 4} = \begin{bmatrix} 22,2817 \\ 33,4225 \\ 44,5634 \\ 66,8451 \end{bmatrix} Nm$	$T_{out\ 3\ 4} = \begin{bmatrix} 16,7113 \\ 25,0669 \\ 33,4225 \\ 50,1338 \end{bmatrix} Nm$	$T_{out\ 4\ 4} = \begin{bmatrix} 13,369 \\ 20,0535 \\ 26,738 \\ 40,107 \end{bmatrix} Nm$

Thus at an input of 40 RPM and a gear ratio of 38:11 (GR1) resulting in an output shaft speed of 138.18 RPM transmitting 100 W through the drive drive would result in an induced torque of 6.9107 Nm at the output shaft.

And at an input of 80 RPM and a gear ratio of 38:42 (GR3) resulting in an output shaft speed of 72.38 RPM transmitting 200 W through the drive drive would result in an induced torque of 26.38 Nm at the output shaft.

As is evident in the calculations above high torques are required to maintain high power output when a low gear ratio is selected, this is in contrast to what cyclist normally would do, as they would increase the gear ratio and their cycling cadence as it is not possible to output those high torque values for long periods of time if possible at all.

Required motor torque

$$T_{motor,1} := \frac{T_{in}}{13,28} = \begin{bmatrix} 1,7977 \\ 2,6965 \\ 3,5954 \\ 5,3931 \end{bmatrix} \begin{bmatrix} 1,1985 \\ 1,7977 \\ 2,3969 \\ 3,5954 \end{bmatrix} \begin{bmatrix} 0,8988 \\ 1,3483 \\ 1,7977 \\ 2,6965 \end{bmatrix} \begin{bmatrix} 0,7191 \\ 1,0786 \\ 1,4381 \\ 2,1572 \end{bmatrix} Nm$$

$$T_{motor,2} := \frac{T_{in}}{6,58} = \begin{bmatrix} 3,6282 \\ 5,4422 \\ 7,2563 \\ 10,8845 \end{bmatrix} \begin{bmatrix} 2,4188 \\ 3,6282 \\ 4,8375 \\ 7,2563 \end{bmatrix} \begin{bmatrix} 1,8141 \\ 2,7211 \\ 3,6282 \\ 5,4422 \end{bmatrix} \begin{bmatrix} 1,4513 \\ 2,1769 \\ 2,9025 \\ 4,3538 \end{bmatrix} Nm$$

After consulting the data sheets of both the motors it was decided that Motor 1 would be the most applicable to the system as a wider range of input torques would be possible.

Appendix B

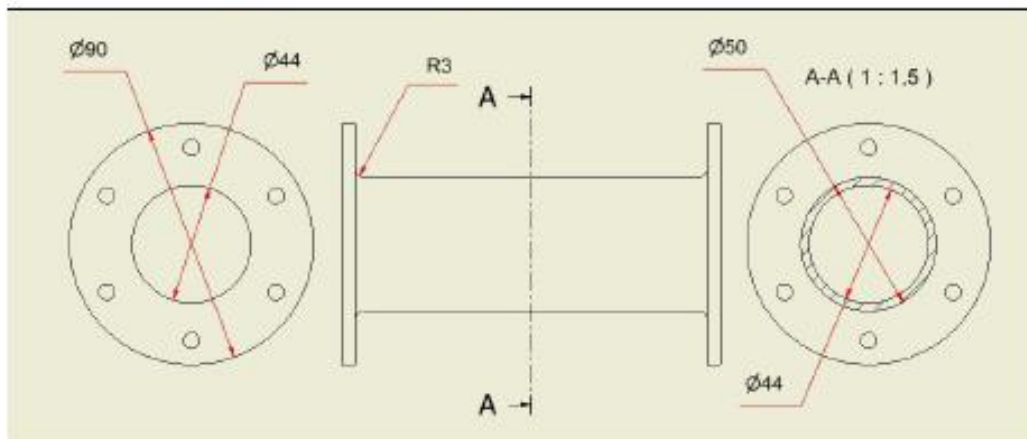
Transducer Design

Transducer Design

Material: Aluminium

Properties: $E := 71,7 \text{ GPa}$ $G := 26,9 \text{ GPa}$ $\nu := 0,33$

$S_y := 276 \text{ MPa}$ $S_{ut} := 310 \text{ MPa}$



Actual Dimensions:

$OD := 50 \text{ mm}$

$ID := 44 \text{ mm}$

$FilletRadius := 3 \text{ mm}$

The following calculations were performed assuming that the transducer body is a solid aluminium shaft with the a cross sectional area equivalent to that of the hollow aluminium tube at the flange shoulder.

The surface area at the shoulder is thus equal to:

$$A1 := \pi \cdot \left(\left(\frac{OD}{2} \right)^2 - \left(\frac{ID}{2} \right)^2 \right) = 0,0004 \text{ m}^2$$

A solid shaft with the equivalent cross sectional area has a diameter of:

$$d := \sqrt{\frac{4 \cdot A1}{\pi}} = 23,7467 \text{ mm}$$

The ratio of the actual aluminium tube diameter to the actual flange diameter is 1.8, thus the equivalent flange diameter assuming a solid aluminium shaft is:

$$D := d \cdot 1,8 = 42,7476 \text{ mm} \quad \text{Equivalent flange diameter}$$

$$r := 3 \text{ mm} \quad \text{Shoulder fillet radius}$$

The critical point which will be analysed in the following calculations is the Transducer Flanged shoulder.

Transducer Shoulder:

$$d_2 := 23,7487$$

Endurance Limit Modifying Factors:

$$a := 4,51 \quad b := -0,265$$

Table 6-2 (Shigley's)

$$S_{ut,2} := 310$$

$$k_a := a \cdot S_{ut,2}^b = 0,9862$$

Surface factor for machine surface material Equation 6-19 pg. 295 (Shigley's)

$$k_b := \left(\frac{d_2}{7,62} \right)^{-0,107} = 0,8855$$

Size factor Equation 6-20 pg. 295 (Shigley's)

$$k_c := 0,59$$

Loading factor Equation 6-26 pg. 299 (Shigley's)

$$k_d := 1$$

Temperature factor Equation 6-28 pg. 300 (Shigley's), Assuming shaft of 20 degrees celcius

Endurance Limit:

$$S'_e := 0,5 \cdot S_{ut} = 155 \text{ MPa}$$

$$S_e := k_a \cdot k_b \cdot k_c \cdot k_d \cdot S'_e = 79,8592 \text{ MPa}$$

Endurance limit Equation 6-18 (Shigley's)

Stress Concentration Factors:

$$\frac{r}{d} = 0,1263 \quad \frac{D}{d} = 1,8$$

$$K_t := 2,1 \quad K_{ts} := 1,7$$

Figure A-15-9 and Figure A-15-8 (Shigley's)

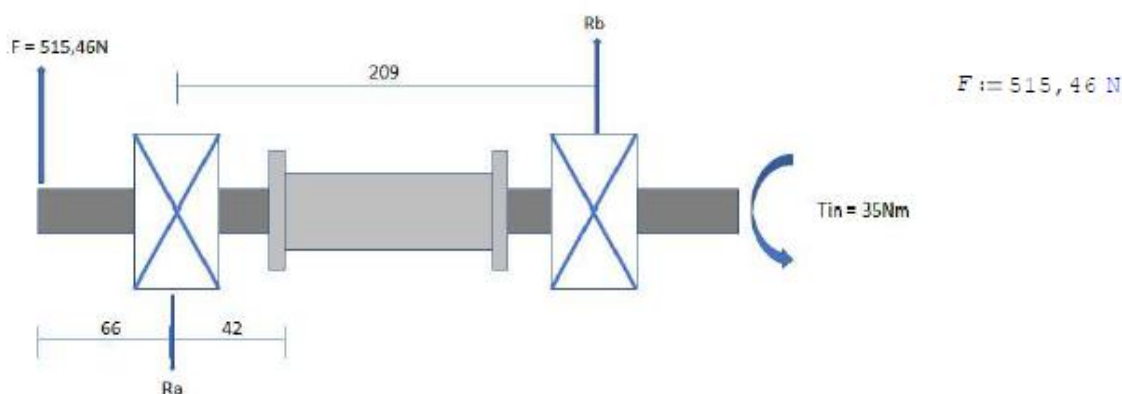
$$q := 0,7 \quad q_s := 0,85$$

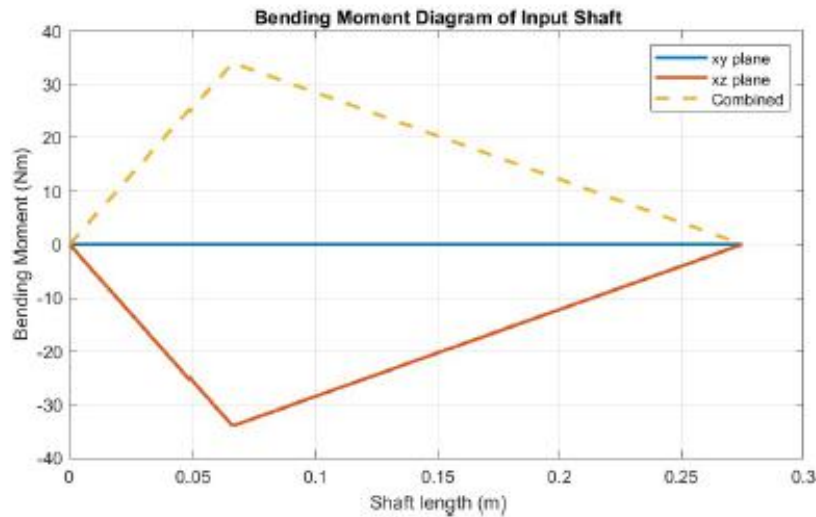
Figure 6-20 and 6-21 pg. 303,304 (Shigley's)

$$K_{fs} := 1 + q_s \cdot (K_{ts} - 1) = 1,595$$

$$K_f := 1 + q \cdot (K_t - 1) = 1,77$$

Equation 6-32 pg. 303 (Shigley's)





Applied Forces:

Torque:

$$T_{max1} := 35 \text{ N m}$$

Min and max applied torque at shoulder Transducer flange shoulder

$$T_{min1} := 35 \text{ N m}$$

$$T_{a1} := \left| \frac{T_{max1} - T_{min1}}{2} \right| = 0 \text{ N m}$$

Amplitude alternating Torque Equation 6-36 pg. 309 (Shigley's)

$$T_{m1} := \frac{T_{max1} + T_{min1}}{2} = 35 \text{ N m}$$

Mean alternating Torque Equation 6-36 pg. 309 (Shigley's)

Moments:

$$M_{max1} := 34,024 \text{ N m}$$

$$M_{min1} := M_{max1} = 34,024 \text{ N m}$$

$$M_{a1} := \left| \frac{M_{max1} - M_{min1}}{2} \right| = 0$$

Amplitude alternating Moment Equation 6-36 pg 309 (Shigley's)

$$M_{m1} := \frac{M_{max1} + M_{min1}}{2} = 34,024 \text{ J}$$

Mean alternating Moment Equation 6-36 pg 309 (Shigley's)

Von Mises Stresses:

$$\sigma_{a1} := \sqrt{\left(\frac{K_t \cdot 32 \cdot M_{a1}}{n \cdot d^3} + 0 \right)^2 \cdot 2 + 3 \cdot \left(\frac{K_{ts} \cdot 16 \cdot T_{a1}}{n \cdot d^3} \right)^2} = 0$$

$$\sigma_{m1} := \sqrt{\left(\frac{K_t \cdot 32 \cdot M_{m1}}{n \cdot d^3} + 0 \right)^2 \cdot 2 + 3 \cdot \left(\frac{K_{ts} \cdot 16 \cdot T_{m1}}{n \cdot d^3} \right)^2} = 66,2571 \text{ MPa}$$

Safety Factor:

$$n_f := \frac{1}{\frac{\sigma_{a1}}{S_e} + \frac{\sigma_{m1}}{S_{ut}}} = 3,5939$$

DE Goodman fatigue failure criterion Equation 6-46 pg 314 (Shigley's)

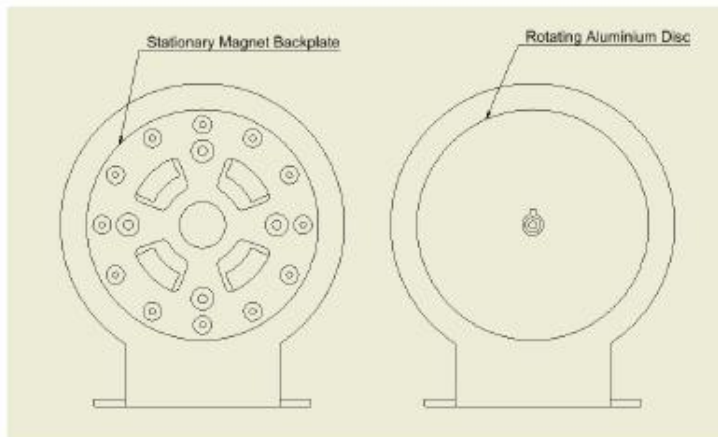
$$n_y := \frac{S_y}{\sigma_{a1} + \sigma_{m1}} = 3,1997$$

First Cycle yield criterion Equation 6-49 pg. 314 (Shigley's)

Appendix C

Eddy Current Brake Design

Eddy Current Brake Design



$$n_{in} := 90 \text{ rpm}$$

Input RPM

Nominal Cadence of a Cyclist

$$P_1 := 300 \text{ watt}$$

Input Power

Desired maximum average power transmitted through drive train

$$r_2 := [11 \ 13 \ 15 \ 17 \ 19 \ 22 \ 25 \ 28 \ 32 \ 36]^T$$

Rear cassette number of teeth per chaining

$$\text{for } i \in [1..10] \quad GR_{1,1} := \frac{32}{r_{2,i}}$$

$$\text{for } i \in [1..10] \quad GR_{2,1} := \frac{34}{r_{2,i}}$$

$$\text{for } i \in [1..10] \quad GR_{3,1} := \frac{36}{r_{2,i}}$$

$$\text{for } i \in [1..10] \quad GR_{4,1} := \frac{38}{r_{2,i}}$$

Possible drive train gear ratios:

Front chain ring size:

32 teeth

34 teeth

36 teeth

38 teeth

Rear cassette chaining size (teeth)

$GR_1 =$	$\begin{bmatrix} 2,9091 \\ 2,4615 \\ 2,1333 \\ 1,8824 \\ 1,6842 \\ 1,4845 \\ 1,28 \\ 1,1429 \\ 1 \\ 0,8889 \end{bmatrix}$	$GR_2 =$	$\begin{bmatrix} 3,0909 \\ 2,6154 \\ 2,2667 \\ 2 \\ 1,7895 \\ 1,5455 \\ 1,36 \\ 1,2143 \\ 1,0625 \\ 0,9444 \end{bmatrix}$	$GR_3 =$	$\begin{bmatrix} 3,2727 \\ 2,7692 \\ 2,4 \\ 2,1176 \\ 1,8947 \\ 1,6364 \\ 1,44 \\ 1,2857 \\ 1,125 \\ 1 \end{bmatrix}$	$GR_4 =$	$\begin{bmatrix} 3,4545 \\ 2,9231 \\ 2,5333 \\ 2,2353 \\ 2 \\ 1,7273 \\ 1,52 \\ 1,3571 \\ 1,1875 \\ 1,0556 \end{bmatrix}$	$\begin{bmatrix} 11 \\ 13 \\ 15 \\ 17 \\ 19 \\ 22 \\ 25 \\ 28 \\ 32 \\ 36 \end{bmatrix}$
----------	---	----------	---	----------	---	----------	---	--

$$GR := [GR_1 \ GR_2 \ GR_3 \ GR_4]$$

Output Shaft speed

Front chain ring size:	32 teeth	34 teeth	36 teeth	38 teeth	Rear cassette chainring size (teeth)
$n_{out} := GR \cdot n_{in} =$	$\begin{bmatrix} 261,8182 \\ 221,5385 \\ 192 \\ 169,4118 \\ 161,5789 \\ 130,9091 \\ 115,2 \\ 102,8571 \\ 90 \\ 80 \end{bmatrix}$	$\begin{bmatrix} 278,1818 \\ 238,3846 \\ 204 \\ 180 \\ 161,0526 \\ 139,0909 \\ 122,4 \\ 109,2857 \\ 95,625 \\ 85 \end{bmatrix}$	$\begin{bmatrix} 294,5455 \\ 249,2308 \\ 216 \\ 190,5682 \\ 170,5263 \\ 147,2727 \\ 129,6 \\ 115,7143 \\ 101,25 \\ 90 \end{bmatrix}$	$\begin{bmatrix} 310,9091 \\ 263,0769 \\ 228 \\ 201,1765 \\ 180 \\ 155,4545 \\ 136,8 \\ 122,1429 \\ 106,875 \\ 95 \end{bmatrix}$	$\begin{bmatrix} 11 \\ 13 \\ 15 \\ 17 \\ 19 \\ 22 \\ 25 \\ 28 \\ 32 \\ 36 \end{bmatrix}$

rpm

Input Torque:

$$T := \frac{P_1}{n_{in}} = 31,831 \text{ N m}$$

Output Torque:

$$n_{out1} := n_{out \ 1 \ 1} \quad n_{out2} := n_{out \ 1 \ 2} \quad n_{out3} := n_{out \ 1 \ 3} \quad n_{out4} := n_{out \ 1 \ 4}$$

$$\text{for } i \in [1..10] \quad \text{for } i \in [1..10] \quad \text{for } i \in [1..10] \quad \text{for } i \in [1..10]$$

$$T_{out1 \ 1 \ i} := \frac{P_1}{n_{out1 \ i}} \quad T_{out2 \ 1 \ i} := \frac{P_1}{n_{out2 \ i}} \quad T_{out3 \ 1 \ i} := \frac{P_1}{n_{out3 \ i}} \quad T_{out4 \ 1 \ i} := \frac{P_1}{n_{out4 \ i}}$$

Front chain ring size:	32 teeth	34 teeth	36 teeth	38 teeth	Rear cassette chainring size (teeth)			
$T_{out1} =$	$N m \begin{bmatrix} 10,9419 \\ 12,9313 \\ 14,9208 \\ 16,9102 \\ 18,8996 \\ 21,8838 \\ 24,868 \\ 27,8521 \\ 31,831 \\ 35,8099 \end{bmatrix}$	$T_{out2} =$	$N m \begin{bmatrix} 10,2983 \\ 12,1707 \\ 14,0431 \\ 15,9155 \\ 17,7879 \\ 20,5965 \\ 23,4051 \\ 26,2138 \\ 29,0225 \\ 33,7034 \end{bmatrix}$	$T_{out3} =$	$N m \begin{bmatrix} 9,7261 \\ 11,4945 \\ 13,2629 \\ 15,0313 \\ 16,7997 \\ 19,4523 \\ 22,1049 \\ 24,7574 \\ 28,2942 \\ 31,831 \end{bmatrix}$	$T_{out4} =$	$N m \begin{bmatrix} 9,2142 \\ 10,8895 \\ 12,5649 \\ 14,2402 \\ 15,9155 \\ 18,4285 \\ 20,9414 \\ 23,4544 \\ 26,805 \\ 30,1557 \end{bmatrix}$	$\begin{bmatrix} 11 \\ 13 \\ 15 \\ 17 \\ 19 \\ 22 \\ 25 \\ 28 \\ 32 \\ 36 \end{bmatrix}$

N m

Equivalent travelling speed of cyclist:

$$R := \frac{0,7366}{2} \text{ m}$$

Radius of MTB Wheel

Front chain ring size (teeth):

32

34

36

38

Rear cassette
chainring size
(teeth)

$$\text{Velocity} := n_{\text{out}} \cdot R = \begin{bmatrix} 36,3524 \\ 30,7597 \\ 26,6584 \\ 23,5221 \\ 21,0461 \\ 18,1762 \\ 16,995 \\ 14,2813 \\ 12,4961 \\ 11,1077 \end{bmatrix} \begin{bmatrix} 38,6244 \\ 32,6822 \\ 28,3245 \\ 24,9922 \\ 22,3615 \\ 19,3122 \\ 16,9947 \\ 13,1739 \\ 10,2771 \\ 11,8019 \end{bmatrix} \begin{bmatrix} 40,8964 \\ 34,6047 \\ 29,9907 \\ 26,4624 \\ 23,6769 \\ 20,4482 \\ 17,9944 \\ 16,0664 \\ 14,0581 \\ 12,4961 \end{bmatrix} \begin{bmatrix} 43,1684 \\ 36,5271 \\ 31,6568 \\ 27,9325 \\ 24,9922 \\ 21,5842 \\ 18,9941 \\ 16,959 \\ 14,8391 \\ 13,1904 \end{bmatrix} \begin{matrix} 11 \\ 13 \\ 15 \\ 17 \\ 19 \\ 22 \\ 25 \\ 28 \\ 32 \\ 36 \end{matrix} \frac{\text{km}}{\text{hr}}$$

Magnetic Brake Calculations:

Front chain ring size (teeth):

32

34

36

38

Rear cassette
chainring size
(teeth)

$$n_{\text{out,rad}} := n_{\text{out}} = \begin{bmatrix} 27,4175 \\ 23,1995 \\ 20,1062 \\ 17,7408 \\ 15,8733 \\ 13,7088 \\ 12,0637 \\ 10,7712 \\ 9,4248 \\ 8,3776 \end{bmatrix} \begin{bmatrix} 29,1311 \\ 24,6494 \\ 21,3628 \\ 18,8496 \\ 16,8654 \\ 14,5656 \\ 12,8177 \\ 11,4444 \\ 10,0138 \\ 8,9012 \end{bmatrix} \begin{bmatrix} 30,8447 \\ 26,0994 \\ 22,6195 \\ 19,9584 \\ 17,8575 \\ 15,4224 \\ 13,5717 \\ 12,1176 \\ 10,6029 \\ 9,4248 \end{bmatrix} \begin{bmatrix} 32,5583 \\ 27,5494 \\ 23,8761 \\ 21,0672 \\ 18,8496 \\ 16,2792 \\ 14,3257 \\ 12,7908 \\ 11,1919 \\ 9,9484 \end{bmatrix} \begin{matrix} 11 \\ 13 \\ 15 \\ 17 \\ 19 \\ 22 \\ 25 \\ 28 \\ 32 \\ 36 \end{matrix} \frac{\text{rad}}{\text{s}}$$

Properties:

$$B_r := 1,3 \text{ T}$$

Bremence filed

$$z := 0,005 \text{ m}$$

Pole distance (Distance between magnet pole and rotating disc, airgap)

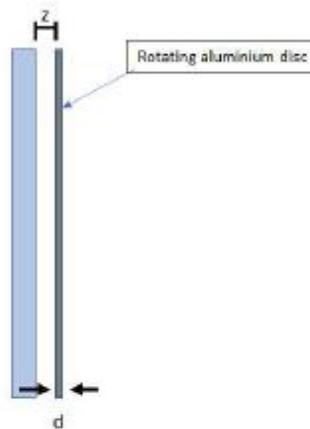
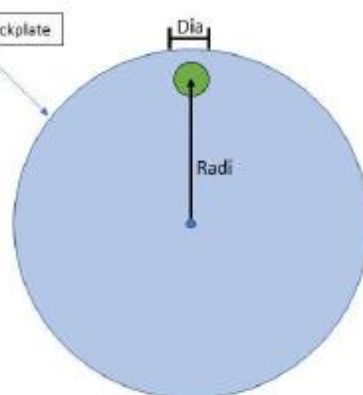
$$D := 0,007 \text{ m}$$

Magnet Thickness

$$r := 0,006 \text{ m}$$

Magnet Radius

Stationary magnet backplate



Dia = Magnet diameter

Radi = distance from centre
of disc to centre of magnet

z = Airgap

d = Disc thickness

Magnetic Flux Density:

$$B := \left(\frac{Br}{2} \right) \cdot \left(\frac{D+z}{\sqrt{r^2 + (D+z)^2}} - \frac{z}{\sqrt{r^2 + z^2}} \right) = 0,1653 \text{ T}$$

(Supermagnete, How do you calculate magnetic flux density, Formula for cylinder magnet flux density)

Calculate Braking Torque:

$$n := 12 \quad \text{Number magnets in slotted magnet disc holder}$$

$$\sigma := 3,69 \cdot 10^6 \frac{\text{S}}{\text{m}} \quad \text{Disc conductivity (Aluminium)}$$

$$\text{Dia} := r \cdot 2 = 0,012 \text{ m} \quad \text{Magnet diameter}$$

$$\text{Radi} := 0,07 \text{ m} \quad \text{Distance from centre of disc to center of magnet}$$

$$d := 0,005 \text{ m} \quad \text{Disc thickness}$$

$$S := \pi \cdot (r)^2 = 0,0001 \text{ m}^2 \quad \text{Magnet pole area}$$

Assuming gear reduction ratio of 1 between the output shaft and Eddy Current Brake Shaft:

$$\text{GR1} := 1 \quad \text{Brake gear reduction ratio}$$

Front chain ring size (teeth):	32	34	36	38	Rear cassette chainring size (teeth)	
$n_{\text{brake}} := n_{\text{out,rad}} \cdot \text{GR1} =$	27,4175	29,1311	30,8447	32,5583	11	
	23,1995	24,6494	26,0994	27,5494	13	
	20,1062	21,3628	22,6195	23,8761	15	
	17,7408	18,8496	19,9584	21,0672	17	
	15,8733	16,8654	17,8575	18,8496	19	
	13,7088	14,5656	15,4224	16,2792	22	
	12,0637	12,8177	13,5717	14,3257	25	
	10,7712	11,4444	12,1176	12,7908	28	
	9,4248	10,0138	10,6029	11,1919	32	
	8,3776	8,9012	9,4248	9,9484	36	
						Aluminium disc speed

Braking torque induced by magnetic brake governed by the following equation:

$$BT := \sigma \cdot \text{Radi}^2 \cdot S \cdot d \cdot B^2 \cdot n_{\text{brake}} \quad (\text{Lee and Park (1999)})$$

Assuming only one magnet in magnet disc holder.

$$BT := \sigma \cdot \text{Radi}^2 \cdot S \cdot d \cdot B^2 \cdot n_{\text{brake}} = \begin{bmatrix} 0,0077 & 0,0081 & 0,0086 & 0,0091 \\ 0,0065 & 0,0069 & 0,0073 & 0,0077 \\ 0,0056 & 0,006 & 0,0063 & 0,0067 \\ 0,005 & 0,0053 & 0,0056 & 0,0059 \\ 0,0044 & 0,0047 & 0,005 & 0,0053 \\ 0,0038 & 0,0041 & 0,0043 & 0,0045 \\ 0,0034 & 0,0036 & 0,0038 & 0,004 \\ 0,003 & 0,0032 & 0,0034 & 0,0036 \\ 0,0026 & 0,0028 & 0,003 & 0,0031 \\ 0,0023 & 0,0025 & 0,0026 & 0,0028 \end{bmatrix} \text{ N m} \quad \text{Braking torque applied}$$

```

BT1 := BT1  BT2 := BT2  BT3 := BT3  BT4 := BT4

nbrake1 := nbrake1  nbrake2 := nbrake2  nbrake3 := nbrake3  nbrake4 := nbrake4

for k ∈ [1..10]
    Pbrake11 k := BT1k · nbrake1k
    Pbrake21 k := BT2k · nbrake2k

for k ∈ [1..10]
    Pbrake31 k := BT3k · nbrake3k
    Pbrake41 k := BT4k · nbrake4k

```

Braking power transmitted by Eddy Current Brake:

Front chain ring size (teeth):	32	34	36	38		Rear cassette chainring size (teeth)
	$P_{brake} := \begin{bmatrix} P_{brake1}^T & P_{brake2}^T & P_{brake3}^T & P_{brake4}^T \end{bmatrix}$					
	$P_{brake} = \begin{bmatrix} \begin{bmatrix} 0,2099 \\ 0,1503 \\ 0,1129 \\ 0,0879 \\ 0,0704 \\ 0,0525 \\ 0,0406 \\ 0,0324 \\ 0,0248 \\ 0,0196 \end{bmatrix} & \begin{bmatrix} 0,237 \\ 0,1697 \\ 0,1274 \\ 0,0992 \\ 0,0794 \\ 0,0592 \\ 0,0459 \\ 0,0366 \\ 0,028 \\ 0,0221 \end{bmatrix} & \begin{bmatrix} 0,2657 \\ 0,1902 \\ 0,1429 \\ 0,1112 \\ 0,089 \\ 0,0664 \\ 0,0514 \\ 0,041 \\ 0,0314 \\ 0,0248 \end{bmatrix} & \begin{bmatrix} 0,296 \\ 0,2119 \\ 0,1592 \\ 0,1239 \\ 0,0992 \\ 0,074 \\ 0,0573 \\ 0,0457 \\ 0,035 \\ 0,0276 \end{bmatrix} \end{bmatrix}$				W	11 13 15 17 19 22 25 28 32 36

Increasing the gear reduction ratio to 9 increases the induced braking torque to:

GR2 := 9

Increased Aluminium disc speed (rad/s)						Rear cassette chainring size (teeth)
Front chain ring size (teeth):	32	34	36	38		
	$n_{brake} := n_{out,rad} \cdot GR2 = \begin{bmatrix} \begin{bmatrix} 246,7578 \\ 208,7951 \\ 180,9557 \\ 159,6668 \\ 142,8598 \\ 123,3789 \\ 108,5734 \\ 96,9406 \\ 84,823 \\ 75,3982 \end{bmatrix} & \begin{bmatrix} 262,1802 \\ 221,8448 \\ 192,2655 \\ 169,646 \\ 151,7885 \\ 131,0901 \\ 115,3593 \\ 102,9994 \\ 90,1244 \\ 80,1106 \end{bmatrix} & \begin{bmatrix} 277,6026 \\ 234,8945 \\ 203,5752 \\ 179,6252 \\ 160,7173 \\ 138,8013 \\ 122,1451 \\ 109,0581 \\ 95,4259 \\ 84,823 \end{bmatrix} & \begin{bmatrix} 293,0249 \\ 247,9442 \\ 214,8849 \\ 189,6044 \\ 169,646 \\ 146,5125 \\ 128,931 \\ 115,1169 \\ 100,7273 \\ 89,5354 \end{bmatrix} \end{bmatrix}$				$\frac{rad}{s}$	11 13 15 17 19 22 25 28 32 36

Braking torque induced in the brake shaft:

$$BT := \sigma \cdot Radi^2 \cdot S \cdot d \cdot B^2 \cdot n_{brake} = \begin{bmatrix} 0,0689 & 0,0732 & 0,0775 & 0,0818 \\ 0,0583 & 0,0619 & 0,0656 & 0,0692 \\ 0,0505 & 0,0537 & 0,0568 & 0,06 \\ 0,0446 & 0,0474 & 0,0502 & 0,0529 \\ 0,0399 & 0,0424 & 0,0449 & 0,0474 \\ 0,0345 & 0,0366 & 0,0388 & 0,0409 \\ 0,0303 & 0,0322 & 0,0341 & 0,036 \\ 0,0271 & 0,0288 & 0,0305 & 0,0321 \\ 0,0237 & 0,0252 & 0,0266 & 0,0281 \\ 0,0211 & 0,0224 & 0,0237 & 0,025 \end{bmatrix} \text{ Nm}$$

$$BT_1 := BT_1 \quad BT_2 := BT_2 \quad BT_3 := BT_3 \quad BT_4 := BT_4$$

$$n_{brake1} := n_{brake_1} \quad n_{brake2} := n_{brake_2} \quad n_{brake3} := n_{brake_3} \quad n_{brake4} := n_{brake_4}$$

$$\begin{aligned} \text{for } k \in [1..10] & \quad P_{brake1_1k} := BT_1_k \cdot n_{brake1_k} & \text{for } k \in [1..10] & \quad P_{brake2_1k} := BT_2_k \cdot n_{brake2_k} \end{aligned}$$

$$\begin{aligned} \text{for } k \in [1..10] & \quad P_{brake3_1k} := BT_3_k \cdot n_{brake3_k} & \text{for } k \in [1..10] & \quad P_{brake4_1k} := BT_4_k \cdot n_{brake4_k} \end{aligned}$$

Braking power induced in the system:

$$P_{brake} := \begin{bmatrix} P_{brake1}^T & P_{brake2}^T & P_{brake3}^T & P_{brake4}^T \end{bmatrix}$$

Front chain ring size (teeth): 32 34 36 38

$$P_{brake} = \begin{bmatrix} 17,0024 & 19,1941 & 21,5187 & 23,9761 \\ 12,1733 & 13,7425 & 15,4069 & 17,1663 \\ 9,1435 & 10,3222 & 11,5723 & 12,8938 \\ 7,1187 & 8,0363 & 9,0096 & 10,0384 \\ 5,6989 & 6,4335 & 7,2126 & 8,0363 \\ 4,2506 & 4,7985 & 5,3797 & 5,994 \\ 3,2917 & 3,716 & 4,166 & 4,6418 \\ 2,6241 & 2,9624 & 3,3211 & 3,7004 \\ 2,0091 & 2,2681 & 2,5427 & 2,8331 \\ 1,5874 & 1,792 & 2,0091 & 2,2385 \end{bmatrix} \text{ W}$$

Having only one magnet in the magnet disc holder produces enough braking torque to transmit a maximum of 23.97 W through the system. This however is not enough to accurately represent a standard bicycle drive train in operation.

Increasing the number of magnets in the stationary magnet disc holder will increase the braking torque induced in the system:

Increasing the number of magnets increases the amount of magnetic flux that is able to pass through the disc, as a result more eddy currents are induced in the rotating aluminium disc and a greater retarding torque is induced.

$n = 12$

Number of magnets

Braking Torque induced in the brake shaft:

$$BT_{12} := \sigma \cdot \text{Radi}^2 \cdot S \cdot d \cdot B^2 \cdot n_{\text{brake}} \cdot n = \begin{bmatrix} 0,8268 & 0,8785 & 0,9302 & 0,9819 \\ 0,6996 & 0,7434 & 0,7871 & 0,8308 \\ 0,6063 & 0,6442 & 0,6821 & 0,72 \\ 0,535 & 0,5685 & 0,6019 & 0,6353 \\ 0,4787 & 0,5086 & 0,5385 & 0,5685 \\ 0,4134 & 0,4393 & 0,4651 & 0,4909 \\ 0,3638 & 0,3865 & 0,4093 & 0,432 \\ 0,3248 & 0,3451 & 0,3654 & 0,3857 \\ 0,2842 & 0,302 & 0,3198 & 0,3375 \\ 0,2526 & 0,2684 & 0,2842 & 0,3 \end{bmatrix} \text{ N m}$$

Braking power induced in the system

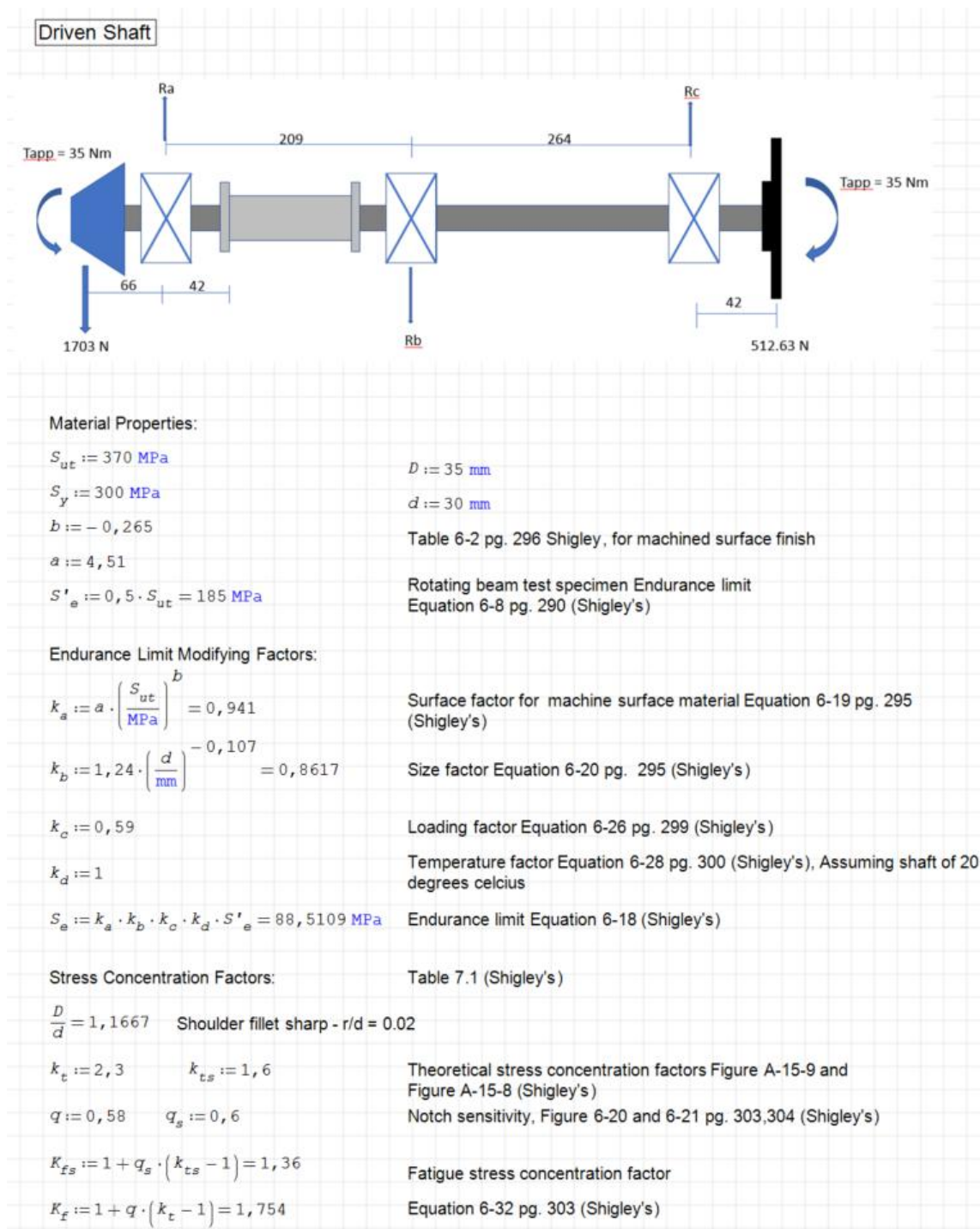
Front chain ring size (teeth):	32	34	36	38	Rear cassette chainring size (teeth)
$P_{\text{brake}_{12}} := n \cdot P_{\text{brake}} =$	204,029	230,3296	258,2242	287,7128	11
	146,0799	164,9106	184,8824	205,9956	13
	109,7223	123,8662	138,8673	154,7255	15
	85,4239	96,4356	108,1146	120,4611	17
	68,3865	77,2019	86,5516	96,4356	19
	51,0073	57,5824	64,5561	71,9282	22
	39,8	44,5918	49,9922	55,7012	25
	31,4892	35,5483	39,8535	44,4047	28
	24,1089	27,2167	30,5128	33,9973	32
	19,049	21,5045	24,1089	26,8621	36

The maximum possible power transmitted through the drive train is 287.71 W when only one magnet disc holder is in interaction with the rotating aluminium disc. This proves that the designed Eddy Current Brake will have the ability to provide enough load to the system to mimic the resistance a cyclist has to overcome. The brake also has the ability to vary its resistance by either changing the number of magnets or introducing the second magnet disc holder and adjusting the opposing magnet pole orientations.

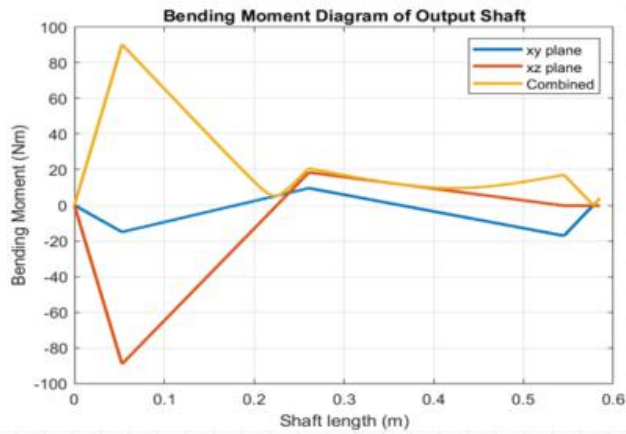
Appendix D

Shaft Design

D.1 Output shaft design



Bending Moment Diagram



Applied Forces:

Torque:

$$T_{max1} := 35 \text{ N m} \quad \text{Assume maximum torque induced in the shaft is 35 Nm at shoulder 1}$$

$$T_{min1} := 35 \text{ N m}$$

$$T_{a1} := \left| \frac{T_{max1} - T_{min1}}{2} \right| = 0 \text{ N m} \quad \text{Amplitude alternating Torque Equation 6-36 pg. 309 (Shigley's)}$$

$$T_{m1} := \frac{T_{max1} + T_{min1}}{2} = 35 \text{ N m} \quad \text{Mean alternating Torque Equation 6-36 pg. 309 (Shigley's)}$$

Moments:

$$M_I := 90 \text{ N m}$$

$$M_{max1} := M_I = 90 \text{ N m}$$

$$M_{min1} := M_I = 90 \text{ J}$$

At Shoulder 1

$$M_{a1} := \left| \frac{M_{max1} - M_{min1}}{2} \right| = 0 \quad \text{Amplitude alternating Moment Equation 6-36 pg 309 (Shigley's)}$$

$$M_{m1} := \frac{M_{max1} + M_{min1}}{2} = 90 \text{ J} \quad \text{Mean alternating Moment Equation 6-36 pg 309 (Shigley's)}$$

Von Mises Stresses:

$$\sigma_{a1} := \sqrt{\left(\frac{k_t \cdot 32 \cdot M_{a1}}{\pi \cdot d^3} + 0 \right)^2 + 3 \cdot \left(\frac{k_{ts} \cdot 16 \cdot T_{a1}}{\pi \cdot d^3} \right)^2} = 0 \quad \text{Equation 6-55 pg.326 (Shigley's)}$$

$$\sigma_{m1} := \sqrt{\left(\frac{k_t \cdot 32 \cdot M_{m1}}{\pi \cdot d^3} + 0 \right)^2 + 3 \cdot \left(\frac{k_{ts} \cdot 16 \cdot T_{m1}}{\pi \cdot d^3} \right)^2} = 80,2066 \text{ MPa} \quad \text{Equation 6-56 pg.326 (Shigley's)}$$

Safety Factor:

$$n_f := \frac{1}{\frac{\sigma_{a1}}{S_e} + \frac{\sigma_{m1}}{S_{ut}}} = 4,6131$$

DE Goodman fatigue failure criterion Equation 6-46 pg 314 (Shigley's)

$$n_y := \frac{S_y}{\sigma_{a1} + \sigma_{m1}} = 3,7403$$

First Cycle yield criterion Equation 6-49 pg. 314 (Shigley's)

At Flange Shoulder

Endurance Limit Modifying Factors:

$$d_2 := 35 \text{ mm} \quad D_2 := 90 \text{ mm}$$

$$k_a := a \cdot \left(\frac{S_{ut}}{\text{MPa}} \right)^b = 0,941$$

Surface factor for machine surface material Equation 6-19 pg. 295 (Shigley's)

$$k_b := 1,24 \cdot \left(\frac{d_2}{\text{mm}} \right)^{-0,107} = 0,8476$$

Size factor Equation 6-20 pg. 295 (Shigley's)

$$k_c := 0,59$$

Loading factor Equation 6-26 pg. 299 (Shigley's)

$$k_d := 1$$

Temperature factor Equation 6-28 pg. 300 (Shigley's), Assuming shaft of 20 degrees celcius

$$S_e := k_a \cdot k_b \cdot k_c \cdot k_d \cdot S'_e = 87,0629 \text{ MPa}$$

Endurance limit Equation 6-18 (Shigley's)

Stress Concentration Factors:

Table 7.1 (Shigley's)

$$\frac{D_2}{d_2} = 2,5714 \quad \text{Shoulder fillet sharp - } r/d = 0.02$$

$$k_t := 2,7 \quad k_{ts} := 2,4$$

Theoretical stress concentration factors, Figure A-15-9 and Figure A-15-8 (Shigley's)

$$q := 0,58 \quad q_s := 0,6$$

Figure 6-20 and 6-21 pg. 303,304 (Shigley's)

$$K_{fs} := 1 + q_s \cdot (k_{ts} - 1) = 1,84$$

Fatigue stress concentration factor

$$K_f := 1 + q \cdot (k_t - 1) = 1,986$$

Equation 6-32 pg. 303 (Shigley's)

Applied Forces:

Torque:

$$T_{max1} := 35 \text{ N m}$$

$$T_{min1} := 35 \text{ N m}$$

Moments:

$$M_1 := 90 \text{ N m}$$

$$M_{max1} := M_1 = 90 \text{ N m}$$

$$M_{min1} := M_1 = 90 \text{ J}$$

At Flange Shoulder

$$T_{a1} := \left| \frac{T_{max1} - T_{min1}}{2} \right| = 0 \text{ N m}$$

$$M_{a1} := \left| \frac{M_{max1} - M_{min1}}{2} \right| = 0$$

$$T_{m1} := \frac{T_{max1} + T_{min1}}{2} = 35 \text{ N m}$$

$$M_{m1} := \frac{M_{max1} + M_{min1}}{2} = 90 \text{ J}$$

Von Mises Stresses:

$$\sigma_{a1} := \sqrt{\left(\frac{k_t \cdot 32 \cdot M_{a1}}{\pi \cdot d_2^3} + 0 \right)^2 + 3 \cdot \left(\frac{k_{ts} \cdot 16 \cdot T_{a1}}{\pi \cdot d_2^3} \right)^2} = 0 \quad \sigma_{m1} := \sqrt{\left(\frac{k_t \cdot 32 \cdot M_{m1}}{\pi \cdot d_2^3} + 0 \right)^2 + 3 \cdot \left(\frac{k_{ts} \cdot 16 \cdot T_{m1}}{\pi \cdot d_2^3} \right)^2} = 60,2615 \text{ MPa}$$

Safety Factor:

$$n_f := \frac{1}{\frac{\sigma_{a1}}{S_e} + \frac{\sigma_{m1}}{S_{ut}}} = 6,1399$$

DE Goodman fatigue failure criterion Equation 6-46 pg 314 (Shigley's)

$$n_y := \frac{S_y}{\sigma_{a1} + \sigma_{m1}} = 4,9783$$

First Cycle yield criterion Equation 6-49 pg. 314 (Shigley's)

D.2 Summary of shaft design

Sample calculations for only the output shaft design is provided but a similar approach was applied to all shaft components and are summarized in tables D.1 to table D.4.

Table D.1: Input shaft.

Critical Point	Safety factors	
	DE-Goodman Fatigue	First cycle yielding
Flange Shoulder	13.29	10.78
Keyway	2.93	4.03

Table D.2: Output shaft.

Critical Point	Safety factors	
	DE-Goodman Fatigue	First cycle yielding
Flange Shoulder	6.14	4.97
Keyway	1.41	3.49

Table D.3: Brake shaft.

Critical Point	Safety factors	
	DE-Goodman Fatigue	First cycle yielding
Shoulder	25.23	20.46
Keyway	2.89	8.58

Table D.4: Gear reduction shaft.

Critical Point	Safety factors	
	DE-Goodman Fatigue	First cycle yielding
Shoulder	2.57	7.79
Keyway	5.83	11.4

Appendix E

Pugh Charts

Band brake	Option 1	IR sensor with reflective tape Photo interrupter with perforated disc	Option 1 Option 2	HBM T-22 in-line Transducer	Option 1
Electromagnetic brake	Option 2			Measure relative twist angle	Option 2
Permanent magnet brake	Option 3			Strain gauges	Option 3
				Measure motor reaction force	Option 4

(a)

(b)

(c)

Figure E.1: (a) Brake option definition. (b) Shaft speed measurement option definition. (c) Torque measurement option definition

Design Criteria	Weight	Concepts					
		Option 1		Option 2		Option 3	
		Rating	Score	Rating	Score	Rating	Score
Reliability (Accurate)	20%	4	0.8	4	0.8	4	0.8
Smooth operation	25%	2	0.5	4	1	4	1
Cost effectiveness	15%	3	0.45	2	0.3	3	0.45
Intracacy	10%	2	0.2	4	0.4	3	0.3
System integration	15%	3	0.45	2	0.3	3	0.45
Accessibility (maintenance)	15%	3	0.45	2	0.3	4	0.6
Total	100%	2.85		3.1		3.6	
Rank		3		2		1	
Continue		No		No		Yes	

(a)

Design Criteria	Weight	Concepts			
		Option 1		Option 2	
		Rating	Score	Rating	Score
Reliability (Accurate)	20%	3	0.6	4	0.8
Cost effectiveness	15%	3	0.45	3	0.45
System integration	20%	3	0.6	3	0.6
Intracacy	10%	2	0.2	3	0.3
Accessibility (maintenance)	15%	4	0.6	4	0.6
Compatibility	20%	4	0.8	4	0.8
Total	100%	3.25		3.55	
Rank		2		1	
Continue		No		Yes	

(b)

Figure E.2: (a) Brake mechanism Pugh chart. (b) Shaft speed measurement Pugh chart.

Design Criteria	Weight	Concepts							
		Option 1		Option 2		Option 3		Option 4	
		Rating	Score	Rating	Score	Rating	Score	Rating	Score
Reliability (Accurate)	25%	4	1	3	0.75	4	1	2	0.5
Intracacy	10%	3	0.3	2	0.2	3	0.3	2	0.2
Cost effectiveness	20%	4	0.8	3	0.6	4	0.8	4	0.8
System integration	15%	4	0.6	3	0.45	3	0.45	2	0.3
Durability	10%	3	0.3	2	0.2	3	0.3	2	0.2
Accessibility (maintenance)	10%	4	0.4	3	0.3	4	0.4	3	0.3
Compatibility	10%	5	0.5	2	0.2	3	0.3	2	0.2
Total	100%	3.9		2.7		3.55		2.5	
Rank		1		4		2		5	
Continue		Yes		No		Yes		No	

Figure E.3: Torque measurement Pugh chart.

Appendix F

Risk Analysis and Safety Procedure

General lab safety:

The following general lab safety instructions are applicable:

- No after hours testing may be performed without the necessary permissions
- An induction is required before testing may be undertaken.
- Closed shoes must be worn at all times.
- Loose clothing may not be worn.
- Good housekeeping practices should be kept during testing.
- No food or drink is permitted in the lab.
- Safety report must be visible and accessible during testing.
- If uncertain, ask for help - it will be willingly provided!

Safety measures during testing:

The following safety measures will be adhered to during testing.

- An emergency stop button will be implemented.
- All rotating parts will be covered during operation of the test rig.

Covid-19 Safety Measures:

The following safety instructions are put in place to prevent the spreading of the Covid-19 virus or being infected by it.

- A face mask is to be worn at all times.
- Sanitise hands at the door before entering the faculty at the allocated entrance.
- Upon entering the faculty each individual is to be screened.
- The compulsory form is to be completed.
- Maintain social distancing unless it interferes with the completion of a compulsory task.
- Sanitise your hand and working area regularly.
- Wear the appropriate PPE's if possible.

Activity based risk assessment:

The severity of the consequences of the activity based risk assessment is based off of the following risk matrix scale.

Table F.1: Risk Assessment Matrix

Risk Matrix					
Likelihood	Medium	High	Extreme	Low	1
	Low	Medium	High	Medium	2
	Low	Low	Medium	High	3
	Impact			Extreme	4

Activity Based Risk Assessment**Table F.2:** Activity Based Risk Assessment

Activity	Risk	Risk Type	Classification of risk severity	Mitigating steps
Entering the faculty	Spreading or getting infected by the Covid-19 virus.	P	3	Follow screening procedure, wear appropriate PPE's and practice social distancing.
Assembling test rig	Dropping tools on floor/feet	P/E	1	Wear closed shoes at all times. Ensure tools are gripped tightly.
Mounting motor on test rig	Dropping motor	P/E	2	Ask for assistance.
Attaching or removing HBM T-22 torque transducer to input or output shaft	Dropping or bumping transducer	E	3	Be very cautious when handling this transducer and ensure it is fastened tightly when system is in operation.
Attaching or removing designed torque transducers	Dropping or bumping transducer	E	3	Be very cautious when handling this transducer and ensure it is fastened tightly when system is in operation.
Changing testing components	Rotating components can cause harm when you do get into contact with them	E/P	2	Ensure power to motor is turned completely off or even disconnected when swapping out components.

Turning on electric servo motor and VSD.	Electrical shock	E/P	3	Ensure that all cabling insulation is intact and that the cables are correctly attached. Ensure wall plugs are switched off while connecting VSD to lead.
Applying load to output shaft, i.e. braking the system.	Snapping chain	E/P	3	Operate the system with a protective cover over all rotating components.
Applying load to output shaft, i.e. braking the system.	Applying a bigger load than what the system is designed to handle can lead to components failure.	E	2	Ensure load experience by shafts does not exceed designed parameters.
Operating test rig at max speed.	Sudden jerk on the system could damage the chain or system components.	E	2	Bring system operating speed up to a max slowly.
Long term tests	Heating up of magnetic brake.	P	2	Place fan at rear end to cool the brake. Do not touch the magnetic brake unless the system has been switched off for at least 5 minutes.
Moving around rig during operation.	Getting loose clothes or fingers caught in rotating components.	P	2	Ensure safety covers are applied when system is operated. Do not wear any loose fitting clothing.
Data capturing.	Data capturing equipment or wiring getting caught up in rotating components.	E	1	Ensure that data capturing equipment is fastened at a safe distance from rotating components. Ensure that any wiring is fastened to the frame of the test rig by either taping it down or using cable ties.
Tidying work area	Tripping	P/E	1	Ensure that the area surrounding the test rig is kept clear of any obstructions.
	Electric shock	P/E	2	Ensure that the area surrounding the test rig is clean and dry.



Figure F.1: Test rig safety chains and guard covering all rotating components.

Appendix G

Techno-Economic Analysis

G.1 Budget

Presented in Table G.1 and Table G.2 are a comparison between the proposed budget of the project and the actual budget of the project. An hourly cost of R400 for a junior engineer and R300 for MMW labour was incurred.

The actual cost of the project was significantly more than what was initially proposed. The majority of the additional costs, are due to certain activities taking longer than anticipated, caused by unplanned events which weren't initially accounted for, as well as misjudgement of the time needed to complete these activities. The activities which account for the biggest increase in costs are, detailed design, cad and technical drawings, manufacturing, test rig assembly and initial testing as well as troubleshooting. The project however would not have been completed had these additional costs not been incurred.

Activity	Engineering Time		Running Costs	Faculty Use	Capital Costs	MMW		Total
	hr	R				Labour	Material	
Literature Review	25	10000						10000
Determine Engineering Requirements	5	2000						2000
Concept Generation	20	8000						8000
Concept Selection	5	2000						2000
Detailed Design	40	16000						16000
Cad and Technical Drawings	10	4000						4000
Workshop Manufacturing						20	6000	8500
Procurement of Electronics	5	1500			800			2300
Software Design	20	8000						8000
Test Rig Assembly	35	14000		700				14700
Torque Transducer Assembly	5	2000	500	125				2625
Calibration	5	2000						2000
Initial Testing and Troubleshooting	16	6400		400				6800
Testing	30	12000		750				12750
Data Processing	25	10000						10000
Design Review	10	4000						4000
Report Writing	50	20000						20000
Total	306	121900	500	1975	800	20	6000	133675

Table G.1: Proposed budget.

Activity	Engineering Time		Running Costs	Faculty Use	Capital Costs	MMW		Total
	hr	R				Labour	Material	
Literature Review	40	16000						16000
Determine Engineering Requirements	8	3200						3200
Concept Generation	25	10000						10000
Concept Selection	8	3200						3200
Detailed Design	60	24000						24000
Cad and Technical Drawings	40	16000						16000
Workshop Manufacturing						103	30900	34764.9
Procurement of Electronics	15	4500			800			5300
Software Design	40	16000						16000
Test Rig Assembly	100	40000		2000				42000
Torque Transducer Assembly	20	8000	500	500				9000
Initial Testing and Troubleshooting	60	24000		1500				25500
Testing	50	20000		1250				21250
Data Processing	30	12000						12000
Design Review	10	4000						4000
Report Writing	65	26000						26000
Total	571	226900	500	5250	800	103	30900	268215

Table G.2: Actual budget.

G.2 Time management

As mentioned above the total cost of the project exceeded the initial amount proposed, which were caused by certain activities taking longer to complete than initially planned. The activities include; detailed design, cad and technical drawings, manufacturing, test rig assembly and initial testing as well as troubleshooting. The biggest part of the project was the design component. This included the design of a test rig frame, both input- and output shafts, two torque transducers capable of measuring small surface strains whilst being structurally sound, and the design of a permanent magnet Eddy current brake capable of inducing an adequate amount of braking load in the system. This was an iterative process as many options were considered. Once an option for each component was selected, an initial design was made and the required calculations performed until the designed component met the engineering requirements. Manufacturing was a big contributor to the additional costs and took longer than planned. A total of 80 drawings were submitted, including assemblies and sub-assemblies, which was more than initially anticipated. Manufacturing was also

delayed by three weeks due to the Covid- 19 pandemic as the workshop was not in operation when the drawings were submitted, and once manufacturing commenced, the workshop was operating at half capacity for the first few weeks. Test rig assembly, initial testing and troubleshooting also accounted for a majority of the additional costs. This was due to slight design changes and once testing commenced, problems arose in the accuracy of measurements which took time to understand and mitigate.

Table G.3 depicts the total time added to the project and the associated costs. Calibration was included as part of the initial testing and troubleshooting, as it could only be performed once the test rig was operating as designed.

Planned Activities	Time (hr)	Actual Activities	Time (hr)	Time Difference
Literature Review	25	Literature Review	40	15
Determine Engineering Requirements	5	Determine Engineering Requirements	8	3
Concept Generation	20	Concept Generation	25	5
Concept Selection	5	Concept Selection	8	3
Detailed Design	40	Detailed Design	60	20
Cad and Technical Drawings	10	Cad and Technical Drawings	40	30
Workshop Manufacturing	20	Workshop Manufacturing	103	83
Procurement of Electronics	5	Procurement of Electronics	15	10
Software Design	20	Software Design	40	20
Test Rig Assembly	35	Test Rig Assembly	100	65
Torque Transducer Assembly	5	Torque Transducer Assembly	20	15
Calibration	5			-5
Initial Testing and Troubleshooting	16	Initial Testing and Troubleshooting	30	14
Testing	30	Testing	50	20
Data Processing	25	Data Processing	30	5
Design Review	10	Design Review	10	0
Report Writing	50	Report Writing	65	15
Total Time	326		644	318
Associated Cost	R134 539.85			

Table G.3: Hours worked.

Activity	Feb	Mar	Apr	May	Jun	Jul	Aug	Sept	Oct	Nov
Literature Review	■	■	■							
Determine Engineering Requirements		■								
Concept Generation		■	■							
Concept Selection			■							
Detailed Design			■	■						
Simulate Designed Transducer (FEM)				■	■					
Cad and Technical Drawings					■	■				
Workshop Manufacturing						■	■			
Procurement of Electronics							■	■		
Software Design								■	■	
Test Rig Assembly									■	■
Torque Transducer Assembly									■	■
Initial Testing and Troubleshooting									■	■
Testing									■	■
Data Processing									■	■
Design Review										■
Report Writing										■

Table G.4: Proposed Gantt chart.

Activity	Feb	Mar	Apr	May	Jun	Jul	Aug	Sept	Oct	Nov
Literature Review										
Determine Engineering Requirements										
Concept Generation										
Concept Selection										
Detailed Design										
Cad and Technical Drawings										
Manufacturing										
Procurement of Electronics										
Software Design										
Test Rig Assembly										
Torque Transducer Assembly										
Initial Testing and Troubleshooting										
Testing										
Data Processing										
Design Review										
Report Writing										

Table G.5: Actual Gantt chart.

G.3 Technical impact

The technical impact of this project was to manufacture a device capable of measuring the associated drivetrain losses of a bicycle. Even though this was the second attempt at this project, by a Stellenbosch University student, there was no prior knowledge of what the previous student had done, when the project had already been well into its development phase. The methods used to measure torque and apply a variable braking load differed substantially, although similar results were obtained. The technical difficulty of measuring small power losses proved to be the determining factor of the success of this project. Many problems arose in the accuracy of measurements, but they were identified and mitigated by various means. The implementation of a permanent magnet Eddy current brake proved to be the right choice as the reduction in vibration induced in the shaft resulted in smooth torque measurements.

The project confirms the possibility to measure small dynamic losses without being dependant on expensive measuring equipment. Even though additional cost were incurred, the system proved to be reliable and with the completion of the aforementioned “further work suggested” there is potentially a lot to benefit from the system in the cycling community.

G.4 Return on investment

Because the entirety of the project was started from scratch and not based off of previous work, the initial investment was big. This was due to research and development costs, as well as the manufacturing of a working prototype. It is expected that further work on this prototype would not be as costly, as the lengthy design and manufacturing process has already been completed, therefore additional costs would only involve improving the existing components. The system thus needs to be optimized, not redesigned. As mentioned earlier, a lot of time was spent on testing and troubleshooting. The problems encountered are now better understood and will be easier to resolve, should it be a problem in the future. Therefore resulting in the efficient use of time and a reduction in costs.

By implementing these suggested improvements on the existing system, it has the potential to accurately measure much smaller losses and further testing can be

conducted using different component sets and gear ratios. The most efficient combination can then be determined. This is of huge interest to the cycling community, as a slight efficiency improvement of 1 % can have a significant effect over a 200 km race. Therefore this system has potential and further work is encouraged.

G.5 Potential for commercialization

The system as a product would not be viable for commercialization due to a small market, but the knowledge and expertise acquired can be sold and is certainly feasible. There is undoubtedly a use for this technology and the potential advantages it can have, by understanding bicycle drivetrain efficiencies and what affects it. Its intellectual property could be sold to bicycle shops and help customers make informed decisions, when spending hard earned money on new equipment. Professional cycling teams can also be approached, as high performance athletes are very competitive in their physical ability, and therefore the use of optimal equipment can result in incremental gains. There is therefore evidence that the system may have the potential for commercialization.

Appendix H

Instrumentation Used

H.1 Calibration

For calibration purposes a universal DAQ (data acquisition system) in conjunction with a in-line torque transducer was used.

H.1.1 Data acquisition system

The data acquisition system used is a universal measuring amplifier and can interface with sensors and transducers based on various sensor technologies. For this system a HBM QuantumX MX440B was used which can act as a stand-alone measuring instrument or can be connected to a PC and data recorder for mobile measurements. The DAQ has a 24-bit analog to digital converter, various sample rates and active low pass filters. This results in good resolution and high precision of the measured values up to 0.05 %. The DAQ was used in conjunction with an in-line torque transducer to measure the dynamic torque accurately in order to calibrate the designed torque transducers of the system. The sampling rate was set to 10 Hz to match the sampling rate of the designed torque transducer and could thus be plotted on the same graph for comparison. The DAQ makes provision for 4 input channels but only one was used for this application. The DAQ interfaces via an ethernet cable with a PC and by using HBM's Catman Easy software, the measured data can be viewed live and stored for post processing.

H.1.2 In-line torque transducer

The in-line torque transducer used for calibration purposes was the HBM T22 rated at 50 Nm. This was considered sufficient as the system was designed to operate at a maximum induced torque at either shaft of 35 Nm. The maximum operating speed of the system is 100 RPM which is well below the nominal rated rotational speed of 20000 RPM.

H.2 Speed sensors

The speed sensor used is a photo-interrupter, which consists of a light source and photo-diode aligned facing each other and detects when an object obstructs emitting light, acting as an optical switch. The photo-interrupter used has an integrated LM393 comparator capable of converting the measured analog values to either a digital high or digital low when the module detects an obstruction, depending on the configuration of the Arduino Interrupt pin, i.e rising edge triggered or falling edge triggered. The sensor has an operating voltage of 3.3 V to 5 V and can be connected to either supply voltage pins on the Arduino Uno DAQ (3.3 V was used in this case).

H.3 Designed torque transducer

H.3.1 Sparkfun HX711 analog-to-digital load cell amplifier

The HX711 is a precision 24-bit analog-to-digital bridge amplifier with selectable gain (32, 64, and 128) and sampling rates (10 Hz, 80 Hz). It operates at an input voltage of 5 V whilst the integrated voltage regulator provides a stable 4.3 V to the bridge sensor. The module outputs data via serial communication as measured values to the Arduino Uno DAQ of the system.

H.3.2 Arduino Nano

Arduino is an open source platform used for building electronics projects. It consists of a programmable circuit board and software, the Arduino IDE (Integrated development environment) that runs on your computer. Arduinos are perfect for interfacing with sensors and one its biggest advantages is that there is no need for a hardware programmer to upload a program onto the microcontroller as the 0.5 Kb of boot loader allows for the program to be uploaded directly onto the microcontroller. An Arduino Nano microcontroller is interfaced with the HX711 module to read the measured torque values via serial communication.

H.3.3 NRF24L01 transceiver module

The NRF24L01 transceiver module is designed to work in the ISM frequency band ranging from 2.400 - 2.4835 GHz and is ideal for low-power wireless applications. The air data rate of the module is configurable but for this system the default air data rate of 1 Mbps was sufficient. The module is used to transmit the measured torque values wirelessly from the torque transducer (Arduino Nano) to the Arduino UNO DAQ system.

H.4 Arduino Uno DAQ system

The Arduino Uno DAQ system is comprised of two Arduino Uno modules each receiving the measured torque values from either the input or output shaft wirelessly via the NRF24L01 modules. The Arduino Uno connected to the photo-interrupter measuring shaft speed is connected to the PC via USB cable and sends the measured torque and speed values to the Python environment for power calculations and data logging.

List of References

- Allen, J. (2018). Band brakes. Available at: <https://www.sheldonbrown.com/band-brakes.html>, [2020, March 28].
- Avia (2017). Data Sheet - HX-711. *Avia Semiconductor*, vol. 1, no. 1, pp. 1–9.
- Baharom, M., Nuawi, M., Harris, S. and Priyandoko, G. (2011). Braking torque analysis on electromagnetic braking study using eddy current for brake disc of al6061 and al7075. In: *Proceedings of Regional Conference on Automotive Research*.
- Binsfeld Engineering [Online] (2020). Weldable vs bondable strain gages for shaft torque measurement. Available at: <https://binsfeld.com/torque-measurement-weldable-bondable-strain-gage/>, [2020, June 15].
- Bolen, R. and Archibald, C.M. (2017). An experimental study on the efficiency of bicycle transmission. *2017 ASEE Zone II Conference*, vol. 32, no. 8, pp. 1317–1327.
- Botshop [Online] (nd). Infrared speed sensor module. Available at: <https://www.botshop.co.za/product/infrared-speed-motor-sensor/>, [2020, April 26].
- Chester, K.R. and Berto, F. (2001). The mechanical efficiency of bicycle derailleur and hub-gear transmissions. *Technical Journal of the IHPVA.*, vol. 52, no. 2, pp. 3–23.
- Circuits4You [Online] (2016). Hx711 load cell amplifier interface with arduino. Available at: <https://circuits4you.com/2016/11/25/hx711-arduino-load-cell/>, [2020, June 20].
- Components101 [Online] (2018). Hx711-24 bit analog to digital converter (adc). Available at: <https://components101.com/ics/hx711-24-bit-analog-digital-converter-adc>, [2020, April 11].
- Edwards, J., Jayawant, B., Dawson, W. and Wright, D. (1999). Permanent-magnet linear eddy-current brake with a non-magnetic reaction plate. *IEE Proceedings-Electric Power Applications*, vol. 146, no. 6, pp. 627–631.
- Figliola, Richard S. ; Beasley, D.E. (2015). *Theory and Design for Mechanical Measurements*. 6th edn. Wiley.
- HBM [Online] (2020). The cost affective alternative. Available at: <https://www.hbm.com/en/2384/t22-torque-transducer-for-simple-torque-applications/>, [2020, April 25].
- Indoor Traing Bikes [Online] (2020). Resistance types. Available at: <https://www.indoortrainingbikes.com/resistance-types/>, [2020, May 5].
- InterlinkKnight (2019). Arduino tutorial: Tachometer (rpm counter). Available at: <https://www.youtube.com/watch?v=u2uJMJWsfsg&t=4s>, [2020, July 20].
- Jang, S.M. and Lee, S.H. (2003). Comparison of Three Types of Permanent Magnet Linear Eddy-Current Brakes According to Magnetization Pattern. *IEEE Transactions on Magnetics*, vol. 39, no. 5 II, pp. 3004–3006. ISSN 00189464.
- Kallhovd, O. (2017). Hx711-adc calibration. Available at: https://github.com/olka1/HX711_ADC/blob/master/examples/Calibration/Calibration.ino, [2020, 10 June].
- Killedar, J.S. (2012). *Dynamometer, Theory and Application to Engine Testing*. Xlibris.
- Kruger, L., Swart, P.L., Chtcherbakov, A.A. and Van Wyk, A. (2004). Non-contact torsion sensor using fibre bragg gratings. *Measurement Science and Technology*, vol. 15, no. 8, p. 1448.

- LastMinuteEngineers [Online] (2018). How nrf24l01+ wireless module works & interface with arduino. Available at: <https://lastminuteengineers.com/nrf24l01-arduino-wireless-communication/>, [2020, May 10].
- Lee, K. and Park, K. (1999). Optimal robust control of a contactless brake system using an eddy current. *Mechatronics*, vol. 9, no. 6, pp. 615–631.
- McKechnie, T. (2018). Design a test rig for measuring bicycle drive train efficiency. *Stellenbosch University Skripsie Project*.
- Micro Robotics [Online] (2020). Wave ir reflective sensor. Available at: <https://www.robotics.org.za/W9523?search=IR%20wave>, [2020, June 15].
- Microcontrollers Lab [Online] (2020 May). Hx711 24-bit analog-to-digital converter (adc) for weigh scales. Available at: <https://microcontrollerslab.com/hx711-adc-weigh-scales/>, [2020, April 10].
- Muftah, M.H., Haris, S.M., Petroczki, K. and Khidir, E.A. (2013). An improved strain gauge-based dynamic torque measurement method. *International Journal of Circuits, Systems and Signal Processing*, vol. 7, no. 1.
- Mustafa, A., Bu, X. and Han, W. (2018). Development of wireless clamp-on torque transducer for rotating shaft. *Journal of Automation and Control Engineering Vol*, vol. 6, no. 1.
- Nordic (2008). nRF24L01+ Single Chip 2.4GHz Transceiver Product Specification v1.0. *Building Research*, , no. 1, p. 78.
- RENESAS [Online] (2017). Op-amps, comparator circuit. Available at: <https://www.renesas.com/us/en/support/technical-resources/engineer-school/electronic-circuits-03-op-amps-comparator-circuit.html>, [2020, April 10].
- Rodrigues, O., Taskar, O., Sawardekar, S., Clemente, H. and Dalvi, G. (2016). Design & fabrication of eddy current braking system. *International Research Journal of Engineering and Technology (IRJET)*, vol. 3, no. 04.
- Rohloff, B. and Greb, P. (2003). Efficiency measurements of bicycle transmissions - a neverending story?. *Technical Journal of the IHPVA.*, vol. 54, no. 2, pp. 11–15.
- RS Components [Online] (2020). Incremental encoder broadcom. Available at: https://za.rs-online.com/web/p/rotary-encoders/7967806?cm_mmc=ZA-PLA-DS3A, [2020, April 15].
- Silva, D., Mendes, J.C., Pereira, A.B., Gégot, F. and Alves, L.N. (2017). Measuring torque and temperature in a rotating shaft using commercial saw sensors. *Sensors*, vol. 17, no. 7, p. 1547.
- Smith, B. (2019). How eddy current brakes work. Available at: <https://www.azom.com/article.aspx?ArticleID=18334>, [2020, March 15].
- Spicer, J.B., Richardson, C.J., Ehrlich, M.J., Bernstein, J.R., Fukuda, M. and Terada, M. (2000). On efficiency of bicycle chain drives. *Technical Journal of the IHPVA.*, vol. 51, no. 2, pp. 3–10.
- Sward, W.T. and Nunley, W. (2016). Selecting the Proper Sensor for Optimum System Design Application Bulletin 201 Application Bulletin 201. pp. 1–5.
- Topf, B. (2019). Ceramicspeed driven â the most efficient road bike drivetrain. Available at: <https://granfondo-cycling.com/ceramicspeed-driven-the-most-efficient-road-bike-drivetrain/>, [2020, March 15].

- van der Merwe, J. (2020). *Mechatronics: Sensors, Actuators and Controls* , [Lecture Notes]. Stellenbosch University.
- Viral Science, The Home of Creativity [Online] (2018). Arduino rpm counter | speed counter. Available at: <https://www.youtube.com/watch?v=vWAgrah925Y>, [2020, April 22].
- Wang, L., Lin, C. and Chern, G. (2001). A torsion sensor made of a corrugated long period fibre grating. *Measurement Science and Technology*, vol. 12, no. 7, p. 793.
- Wikipedia [Online] (2020). Force between magnets. Available at: "https://en.wikipedia.org/wiki/Force_between_magnets", [2020, 22 May].
- Wouterse, J. (1991). Critical torque and speed of eddy current brake with widely separated soft iron poles. In: *IEEE Proceedings B (Electric Power Applications)*, vol. 138, pp. 153–158. IET.
- Zappalá, D., Bezziccheri, M., Crabtree, C. and Paone, N. (2018). Non-intrusive torque measurement for rotating shafts using optical sensing of zebra-tapes. *Measurement science and technology*, vol. 29, no. 6, p. 065207.